Master's thesis

NTNU
Norwegian University of Science and Technology
Faculty of Information Technology and Electrical Engineering
Department of Engineering Cybernetics

Eirik Eikeseth Gillund

Single target tracking for Phased Array Radio Navigation

Master's thesis in Cybernetics and Robotics
Supervisor: Kristoffer Gryte
June 2022

NTNU
Kunnskap for en bedre verden

Eirik Eikeseth Gillund

Single target tracking for Phased Array Radio Navigation

Master's thesis in Cybernetics and Robotics
Supervisor: Kristoffer Gryte
June 2022

Norwegian University of Science and Technology
Faculty of Information Technology and Electrical Engineering
Department of Engineering Cybernetics

NTNU
Norwegian University of
Science and Technology

Preface

This master's thesis is written as a part of the course TTK4900 and accounts for 30 credits in the 2-year masters degree programme *Cybernetics and robotics*. It was written during the spring semester of 2022 and concludes the master's programme at Norwegian University of Science and Technology(NTNU).

The idea for this thesis was brought forth to me by my supervisor Dr. Kristoffer Gryte who in his research proposed a navigation system for a fixed-wing Unmanned Aerial Vehicles(UAV) in GNSS denied areas. The navigation system uses measurements from a phased array radio system(PARS) to aid an inertial navigation(INS) system of the UAV. Research showed that this system was susceptible to multipath propagation when flying above the sea. Because of this, a deeper look into the use of single target tracking algorithms was of interest.

The software provided as a starting point for the work in this thesis was the *navigation toolbox*. It is a MATLAB toolbox developed at the department of Engineering Cybernetics at NTNU. The development process is led by Torleiv H. Bryne. Access is restricted, although it may be granted on request. See appendix A for more information. The toolbox contains code that is able to simulate an INS on recorded flight data, with the choice of estimation algorithm currently being the Multiplicative Extended Kalman Filter(MEKF) or nonlinear observers.

The MATLAB toolbox, tuning of the INS and MEKF, in combination with datasets from previous flight experiments with a fixed-wing UAV provides the starting point for the work in this thesis.

This thesis aims to first give a detailed explanation to how PARS can be used in navigation systems for UAVs. The main focus will however be on single target tracking, and how it can be used to mitigate the effect of multipath propagation that provides clutter measurements.

The assumed background of the reader is a person with graduate level experience within Cy-

bernetics and robotics or signal processing. This report might also interest people with other engineering backgrounds, but it is recommended to have general knowledge about linear system theory and the Kalman filter to be able to understand the report.

While writing this thesis a good amount of work has been put into understanding sensor fusion at a deeper level than the author previously have. The research therefore consisted of reading in books and papers about target tracking and Kalman filtering.

Acknowledgment

I would like to thank my supervisor Dr. Kristoffer Gryte for his guidance and feedback through several meeting and emails this spring semester. He has been both encouraging and helpful when I have been stuck on a problem or didn't know how to go forward. I would also like to thank him for providing me tips on literature and for giving me feedback on a draft version of this thesis.

Another person that deserves a big thank you is PhD Candidate Mika Okuhara. We have both been working on the problem of mitigating the effect of multipath in the PARS based navigation system. As a result, she has helped me with both understanding theory and implementing the target tracking algorithms in the MATLAB toolbox. For this I am very grateful. Mika has been available for discussion and help through several emails and a meeting at the start of the semester. I would also like to thank here for extracting the 4 largest direction of arrival measurements from the raw Agdenes dataset.

Lastly I would also like to recognize Professor Emeritus Marvin Rausand for the work to prepare the latex template used in this report.

Eirik Eikeseth Gillund

Abstract

Many Unmanned aerial vehicles(UAV) use position measurements provided by a Global Satellite Navigation System(GNSS) to aid their navigation system. GNSS is however vulnerable to several environmental disturbances and potential attacks. A GNSS receiver may become subject to intentionally emitted radio-frequency(RF) noise known as jamming, which causes the receiver to loose track of the GNSS signals. Artificial GNSS signals can also be transmitted towards the receiver to provide false position measurements and steer the UAV off course. This is known as spoofing. These vulnerabilities has made it essential to look into other alternatives for position measurements.

A promising local GNSS independent navigation solution has been demonstrated at the NTNU Unmanned Aerial Vehicle laboratory (UAVlab) in the past few years. It uses Phased Array Radio System(PARS) that provides spherical position measurements of the UAV, described by a range, an azimuth- and an elevation angle. Previous flight experiments above the ocean with the proposed navigation system implemented has however shown that the PARS measurement is susceptible to multipath propagation. The signal transmitted from the UAV is reflected off the ocean surface and arrives at the PARS ground antenna together with the direct signal. This especially effects the elevation angle.

This Master's thesis investigates whether single target tracking algorithms can mitigate the effect of multipath in the PARS aided navigation system. By monitoring the measurements from both the direct- and reflected signals, a tracking algorithm is applied to handle the measurement uncertainty. Two single target tracking algorithms are implemented in an existing MATLAB navigation toolbox framework. The toolbox is able to play back previous flight experiments using recorded sensor data for analysis and testing. The implemented algorithms are the Nearest Neighbor(NN)- and the Probabilistic Data Association(PDA) filter. These are tested both on a prerecorded dataset from a flight experiment above the ocean, and a synthetic dataset based on observations from other closed-loop flight experiments.

The results indicate that single target tracking algorithms alone are not able to mitigate the full effect of the multipath propagation in the PARS measurements. The data used in this thesis indicate that interference between different signal paths is a bigger problem than jumps between different signal paths in the direction of arrival estimation. The NN filter handled the latter case better than the PDA filter, however none of the algorithms was able to mitigate the interference-induced oscillations in the elevation angle.

Sammendrag

Mange ubemannede luftfartøy(UAV) benytter seg av posisjonsmålinger fra et globalt satellittnavigasjonssystem(GNSS) i sine egne navigasjonssystemer. Likevel er GNSS vist å være sårbart for både miljøforstyrrelser og potensielle angrep. En GNSS mottaker vil kunne bli utsatt for bevisst utsendt radiofrekvens støy, kjent som jamming, for å forstyrre den fra å motta GNSS signaler. Kunstige GNSS signaler kan også bli sendt mot mottakeren for å gi feil posisjonsmålinger og dermed være i stand til å styre luftfartøyet til feil kurs. De nevnte problemene motiverer søken etter alternative posisjonsmålinger for ubemannede luftfartøy.

Et lovende navigasjonssystem som er uavhengig av GNSS i et lokalt område har de siste årene blitt utviklet og demonstrert av NTNU sitt laboratorium for ubemannede luftfartøy. Systemet benytter et fasestyrt radiosystem(PARS) for å motta sfæriske posisjonsmålinger av det ubemannede luftfartøyet, i form av en avstand, en asimutal vinkel og en elevasjonsvinkel. Tidligere fly eksperimenter over havet med navigasjonssystemet implementert har vist at PARS posisjonsmålingene påvirkes av flerveisinterferens. Signalet som sendes fra luftfartøyet reflekteres også fra havets overflate før det mottas hos PARS antennen på bakken. Denne flerveisinterferensen påvirker spesielt elevasjonsvinklene.

Denne masteroppgaven undersøker om enkeltmålfølgingsalgoritmer kan benyttes for å minske effekten fleirveisinterferens har på navigasjonssystemet som benytter PARS posisjonsmålinger. Ved å overvåke både det direkte og de reflekterte signalene, så kan en enkeltmålfølgingsalgoritme brukes for å finne ut av hvilket signal som faktisk kommer fra luftfartøyet. To algoritmer blir implementert i et eksisterende navigasjonssystem rammeverk i MATLAB. Dette rammeverket benyttes for å spille av sensor data fra tidligere eksperimenter og dermed kunne gjøre nye analyser og tester. Algoritmene nærmeste nabo(NN)- og det sannsynlighetsbaserte data assosiasjons(PDA) filteret blir implementert. Disse testes på data fra et tidligere fly eksperiment over havet, og et syntetisk datasett basert på observasjoner gjort i andre fly eksperimenter.

Resultatene indikerer at enkeltmålfølgingsalgoritmer alene ikke er i stand til å minke effekten av flerveisinterferens i PARS posisjonsmålingene. Dataen som ble benyttet i denne masteroppgaven viser at interferens mellom det direkte og de reflekterte signalene er et større problem enn hopp mellom de estimerte ankomstretningene når et reflektert signal ble sterkere enn det direkte. NN filteret håndterte et sterkere reflektert signal bedre enn PDA filteret, selv om ingen av algoritmene var i stand til å minke de observerte interferens induserte oscillasjonene i elevasjonsvinkelen.

List of symbols

ρ	Range $[m]$
ξ	Azimuth angle [°]
α	Elevation angle [°]
ϵ_ρ	Range measurement noise $[m]$
ϵ_ξ	Azimuth measurement noise [°]
ϵ_ξ	Azimuth measurement noise [°]
ϕ	Roll angle [°]
θ	Pitch angle [°]
ψ	Yaw angle [°]
l_{lon}	Longitude [°]
l_{lat}	Latitude [°]
σ	Standard deviation
V	Volume of validation gate $[m^3]$
γ	Validation gate threshold.
λ	Clutter density $[m^{-3}]$
P_D	Probability of detection.
P_G	Probability of a measurement being gated.
z	Number of clutter measurements.

m Number of validated measurements.

$\boldsymbol{x}$ True state

$\delta\boldsymbol{x}$ Error state

$\boldsymbol{x}_{nom}$ Nominal state

$\boldsymbol{y}$ Measurement

$\boldsymbol{p}$ Position $[m]$

$\boldsymbol{v}$ Velocity $[\frac{m}{s}]$

$\boldsymbol{q}$ Attitude unit quaternion

$\boldsymbol{b}_{acc}$ Accelereomter bias $[m/s^2]$

$\boldsymbol{b}_{ars}$ Gyroscope bias $[^\circ/s]$

$\boldsymbol{\Theta}$ Attitude parameterized by euler angles $[^\circ]$

$\boldsymbol{f}$ Specific force $[m/s^2]$

$\boldsymbol{\omega}$ Angular velocity $[^\circ/s]$

$\boldsymbol{g}$ Gravitational acceleration $[m/s^2]$

$\boldsymbol{M}$ Covariance mapping from spherical to Cartesian coordinates

$\boldsymbol{R}_b^a$ Rotation matrix from some reference frame {b} to {a}.

$\boldsymbol{I}$ Identity matrix.

$\boldsymbol{A}$ State transition matrix.

$\boldsymbol{a}$ Modified Rodriguez parameters

$\boldsymbol{B}$ Discrete control input matrix.

$\boldsymbol{C}$ Discrete measurement matrix.

$\mathbb{S}$ Innovation covariance matrix.

$\boldsymbol{K}$ Kalman gain.

$\boldsymbol{P}$ Error covariance matrix.

$\boldsymbol{R}$ Measurement noise covariance matrix.

$\boldsymbol{Q}$ Process noise covariance matrix.

$\boldsymbol{w}$ Measurement noise.

$\boldsymbol{v}$ Process noise.

$\boldsymbol{\beta}$ Association probabilities.

Abbreviations

AHRS Attitude and Heading Referece System.

ARS Attitude Rate Sensor.

BVLOS Beyond Visual Line Of Sight.

CA Constant Acceleration.

CT Constant Turn.

CV Constant Velocity.

DoA Direction of Arrival.

ECEF Earth-Centered-Earth-Fixed.

ECI Earth-Centered-Inertial.

EKF Extended Kalman Filter.

ESKF Error State Kalman Filter.

GNSS Global Navigation Satellite Systems.

GPS Global Positioning System.

IMU Inertial Measurement Unit.

INS Inertial Navigation System.

KF Kalman Filter.

MAE Mean Absolute Error.

ME Mean Error.

MEKF Multiplicative Extended Kalman Filter.

MHT Multiple Hypothesis Tracking.

MRP Modified Rodriguez parameters.

MUSIC Multiple Signal Classification.

NED North East Down.

NIS Normalized Innovation Squared.

NN Nearest Neighbor.

PARS Phased Array Radio System.

PDA Probabilistic Data Association.

PDDA Propagator Direct Data Acquisition.

RF Radio Frequency.

RMSE Root Mean Square Error.

RTK Real Time Kinematics.

RTT Round Trip Time.

SNR Signal to Noise Ratio.

STD Standard Deviation.

UAV Unmanned Aerial Vehicle.

UAVlab Unmanned Aerial Vehicle laboratory.

UWB Ultra-Wideband.

Contents

Preface i
Abstract iii
Sammendrag v
List of symbols vii
Abbreviations xii
Contents xv

1 Introduction **1**
1.1 Previous work 3
1.2 Problem description 6
1.3 Contributions 7
1.4 Structure of thesis 7

2 Mathematical prerequisites **9**
2.1 Vector and matrices 9
2.2 Statistics 9
2.3 Reference frames 11
2.4 Representation of attitude 14

3 Theory **17**
3.1 Phased array radio systems 17
3.2 Multipath propagation 22
3.3 Navigation systems 27
3.3.1 Inertial Navigation Systems 28
3.3.2 Model based navigation systems 30
3.4 The Kalman Filter and it's error-state formulation 32
3.4.1 The Extended Kalman Filter 34
3.4.2 The Multiplicative Extended Kalman Filter 35

3.5 Single target tracking . . . 39
3.5.1 Validation of measurements . . . 40
3.5.2 Mathematical models in tracking . . . 41
3.5.3 Nearest Neighbor Filter . . . 43
3.5.4 The Probabilistic Data Association Filter . . . 44
3.5.5 Multiple hypothesis tracking . . . 46

4 Implementation and dataset examination 49
4.1 Implementation in Matlab Toolbox . . . 50
4.2 The Agdenes dataset . . . 52
4.3 Synthetic dataset . . . 54
4.4 Ground truth measurements for comparison . . . 59

5 Results 61
5.1 The Agdenes dataset . . . 61
5.1.1 One measurement using the largest peak . . . 61
5.1.2 Nearest Neighbor Filter . . . 67
5.1.3 Probabilistic Data Association Filter . . . 70
5.1.4 Observations . . . 73
5.2 Synthetic dataset . . . 74
5.2.1 Nearest Neighbor . . . 74
5.2.2 Probabilistic Data Association Filter . . . 76

6 Discussion 81
6.1 The dataset and measurement extraction . . . 81
6.2 Performance of the single target tracking algorithms . . . 82
6.3 A realistic analysis scenario . . . 84
6.4 Dependent multipath measurements . . . 85
6.5 Further work . . . 86

7 Conclusion 87

Bibliography 88

A Matlab Toolbox 93

B Tuning and equations **95**
B.1 Linear error state kinematics 95
B.2 Tuning of INS and MEKF 96

C Results - Statistics **99**
C.1 The Agdenes dataset - One measurement using the larges peak 99
C.2 The Agdenes dataset - Nearest Neighbor filter 101
C.3 The Agdenes dataset - Probabilistic Data Association filter 102
C.4 Synthetic dataset - Nearest Neighbor filter 104
C.5 Synthetic dataset - Probabilistic Data Association Filter 105

D Results - Figures **107**
D.1 The Agdenes dataset - One measurement using the larges peak 107
D.2 The Agdenes dataset - Nearest Neighbor filter 110
D.3 The Agdenes dataset - Probabilistic Data Association filter 112
D.4 Synthetic dataset - Nearest Neighbor filter 114
D.5 Synthetic dataset - Probabilistic Data Association Filter 116

Chapter 1

Introduction

Global navigation satellite systems(GNSS) are a widely used positioning sensor for unmanned aerial vehicles(UAVs).[1] GNSS systems such as the Global Positioning System(GPS)[2] has the advantage of providing worldwide coverage for position determination of a GNSS receiver. The GNSS receiver it mounted to the UAV and uses the continuously transmitted signals from at least 4 satellites to derive a precise position estimate.

UAVs have been proven to be very useful in many business sectors such as agriculture, infrastructure and logistics, both for military and civil applications.[1] As shown in the literature review [3] and the references therein, monitoring of critical infrastructure such as power lines and construction sites have used UAV with onboard sensors such as cameras to detect potential problems. The same holds for agriculture where inspection of the crops with UAVs can lead to increased productivity by for instance detecting weeds and crop disease. Delivery companies like Amazon has also started the process of developing systems for package deliveries with autonomous UAVs.[4] These are only some of the applications in which deploying UAVs will improve existing solutions, the reader is referred to [3] for a thorough overview of the potential of UAVs in civil applications.

With UAVs being utilized for tasks such as the aforementioned, the integrity of operation must be guaranteed. This means that the navigation system must handle losing the GNSS signal or flying into GNSS-denied areas. Although GNSS is a widely used positioning system, it has been proven to be vulnerable to several radio-frequency(RF) propagation error sources. As the GNSS signal travels through the atmosphere it is subject to frequency dependent delays in both the ionosphere and troposphere. The ionospheric delays will vary depending on the solar activity while the tropospheric delays depend on variables such as temperature and humidity. In

cities where the density of tall buildings is high, multipath propagation will cause interference to the direct GNSS signal, which again will affect the accuracy of the calculated position.[5] The tropospheric- and ionospheric delays can be accounted for by utilizing a dual frequency GNSS receiver and mathematical models. There also exists techniques to mitigate the effect of multipath propagation which are listed in [5], but it still is considered to be RF propagation error sources that effects the calculated position the most.

The RF propagation error sources are to some extent predictable, but GNSS can also be a victim of intentional attacks known as jamming and spoofing. [5] Jamming could be both intentional and unintentional. It happens when a device releases RF energy near the GNSS signal frequency bands, with sufficient power to make the receiver incapable of detecting the GNSS signal. The received GNSS signal has a low signal to noise ratio(SNR), which makes it susceptible to these attacks. Some techniques to mitigate the effect of jamming include the use of spatial filtering with beamforming and an antenna array at the receiver to steer the beam direction towards the satellite.[6] Spoofing is when an artificial GNSS signal is transmitted from a device. The GNSS receiver may interpret this signal as the authentic signal from a satellite. If the receiver locks on to the artificial signal it may be steered off course without triggering any alarm. An example of this was performed by Kerns et. al. in [7], where GPS spoofing is performed on a UAV in simulations and field experiments. Techniques to defend a receiver from spoofing includes encryption of the GNSS signal to make it hard for a spoofer device to produce similar signals, and drift monitoring which detects unusual changes in the receiver position. A comprehensive overview of spoofing defense strategies can be found in [8].

Even with mitigation techniques, jamming and spoofing motivates to use of other positioning sensors in UAVs, to make it less dependent on GNSS. As shown in [9], other GNSS-independent navigation solutions based on visual odeometry, visual SLAM and Ultra-wideband(UWB) poitioning has been proposed in the references therein. However vision based navigation is affected by weather and illumination and require an environment with a high density of visual features. UWB positioning systems depends on several transceiver antennas at known locations, and has mostly been used for indoor navigation due to its limited range. This makes them less relevant for e.g. beyond visual line of of sight(BVLOS) operation of UAVs above open water.

Researchers at the NTNU Unmanned Aerial Vehicle laboratory(UAVlab)[10] has also been investigating alternatives to GNSS for UAV navigation systems, especially in flights above the ocean.

A promising solution that uses a phased array radio system(PARS) to provide position measurements that aids an inertial navigation system(INS) has been presented in [11], [12] and [13]. The PARS system consist of two antenna arrays. One at a known location on the ground, and one mounted to the UAV. Using direction of arrival(DoA)- and round trip time(RTT) estimation of the signal sent from the UAV to the ground station, a spherical position measurements can be obtained. The spherical position consists of a range, azimuth and elevation angle. The goal of this thesis is to expand this research by investigating how the PARS based INS can become more robust against multipath propagation from the ocean surface, which has proven to be a problem. The published research on PARS based navigation is summarized in chapter 1.1.

1.1 Previous work

Using PARS for aiding measurements has been an active field of research over the last few years at the Norwegian University of Science and Technology(NTNU). The PARS used in the research consists of the Radionor $CRE2-189$[14] antenna as ground station, and the $CRE2-144-LW$[15] mounted to the UAV. The PARS ground stations frustum covers 90^o in the horizontal and vertical direction, with a maximum range of $60km$.[16] This means that the azimuth angles and elevation angle ranges from -45^o to 45^o. The fact that the PARS is directional and that the position measurements transmitted from the ground station can be strongly encrypted makes it more robust against spoofing attacks. It also yield a high SNR compared to the GNSS signals.

In 2017 Albrektsen et. al. [16] published a paper in which they displayed PARS as a system that has merit in providing aiding measurements to a navigation system. It was shown that due to suspected reflections of the UAV transmitted signal from the ocean surface, the vertical accuracy of the UAV position estimate was reduced. However by introducing a barometer to provide the vertical position measurement, the Mean Error(ME) compared to the RTK-GNSS measurement was $24.23m$. The measurements were obtained in an beyond visual line of sight(BVLOS) flight approximately $5km$ away from the PARS ground antenna array.

In [11] the PARS measurements are used together with an IMU, a barometer and a magnetometer in two separate nonlinear observers which estimates the position, velocity and orientation of the UAV respectively. Albrektsen et. al. performs a 35 minute flight with the UAV, where the largest distance from the ground antenna is $5.35km$. The navigation system provides a root mean square error(RMSE) accuracy of $26.3m$ when compared to the RTK-GNSS position.

Further in [17] two identical observers like the one presented in [11] runs in parallel. The only difference between them is the fact that one uses a position measurement from PARS and barometer, and the other from GNSS. The two observers provide two postion, velocity and attitude estimates that can be compared in a Kalman filter(KF). If the difference is beyond some threshold, the GNSS is being spoofed and the observer aided by PARS should be trusted. The paper thereby displays a navigation system that can switch between RTK-GNSS aiding and PARS aiding, depending on whether the GNSS signal is being spoofed.

Even though [16]-[17] mentioned the fact that the the range and elevation angle could not be trusted due to spikes and jumps caused by reflections from the ocean floor, Gryte et. al. [12] field tests above land yielded reasonable results. In [12] the navigation system is an INS aided by PARS measurements based on the Multiplicative Extended Kalman Filter(MEKF). By using a MEKF rather than nonlinear observers, couplings between the rotational- and translational estimation error makes it possible to estimate the heading of the UAV without a compass/magnetometer. The navigation system is also implemented with an outlier rejection technique to make the MEKF reject unreliable PARS measurements. The navigation system was implemented on a *Nordic Unmanned Camflight BG-200 HL* multirotor UAV, as opposed to the fixed-wing UAV *Skywalker-X8* used in [16]-[17] Through field tests where the UAV flew with a range of about a hundred meteres away from the PARS ground antenna array, Gryte et.al. showed that an INS aided by PARS based position measurements in a MEKF yielded an RMSE of $6.86m$ compared to the GNSS position.

Further Gryte et. al. [13] performs experiments with the PARS and MEKF based navigation system in above water flights. Among the experiments is a $20km$ flight with a maximum distance of $5km$ from the PARS ground antenna array. The elevation angle was heavily affected by multipath propagation in flights above the ocean.[16, 11] Therefore a barometer was used to provide the vertical position measurement. The range and azimuth angle was provided by the PARS, resulting a cylindrical 3D position measurement. The result was mean error of $19.95m$ to the norm, compared to the GNSS-RTK solution. With a much smaller error in the down direction compared to North and East, as the barometer was used to calculate the height component of the position. The paper also showed that the elevation angle measurement displayed jumps with a magnitude of $30°$. This could be explained by the fact that PARS is designed for communication purposes. When the reflected signal became stronger than the direct signal, the PARS

provided the strongest direction of arrival as the position measurement.

In [18] Okuhara et. al. proposes an automatic calibration algorithm which estimates the PARS ground antenna orientation with respect to the local navigation frame, NED. An introduction to the coordinate frame used in navigation is given in chapter 2. To obtain an accurate position estimate of the UAV, it is crucial to have precise knowledge of the antenna position and orientation. The algorithm is based on the MEKF which uses GNSS measurements in the initial part of the flight to estimate the orientation. The flight data recorded at Agdenes, Norway in [18] is used in this thesis.

Several of the above research papers mention that especially in flights above the ocean, multipath propagation becomes a problem that affects the PARS from choosing the correct signal. Introducing a target tracking algorithm that attempts to keep track of not only the direct signal but also the reflected signals, might make the system more robust against this problem. If the elevation angle proves to be more reliable through tracking, then the barometer can be excluded from the navigation solution. Thereby obtaining an INS purely aided by PARS positioning measurements. Another approach that could then possible is to use both the barometer and the full spherical PARS position measurement. This would increase the robustness of the system and help with estimating the bias in the barometer. The results from this thesis might also be of interest for those working with navigation using Bluetooth Low Energy(BLE) version 5.1. A constant tone extension(CTE) with constant frequency and wavelength is added to the Bluetooth signal in this version of BLE. Sampling the phase and amplitude of the CTE using a Bluetooth antenna array, makes it possible to estimate the DoA of the Bluetooth signal.[19]

1.2 Problem description

The official problem description for this thesis, provided by supervisor Kristoffer Gryte, is defined in the following list:

1. The candidate should familiarize with existing multiplicative extended Kalman filters and "low complexity" target tracking methods suitable for mitigating multipath in phased-array radio navigation.

2. Qualitatively evaluate the target-tracking methods on their complexity and ability to mitigate the multipath problem, and implement the most promising methods in the existing MATLAB navigation toolbox.

3. Compare the implemented methods, on pre-recorded flight data, for the given application [using appropriate metrics]

4. Discuss the implications of the results. Especially consider whether more complex target tracking algorithms have merit.

5. Conclude in written report.

An important point to notice is what is meant by "low complexity" target tracking methods. In this thesis, low complexity is interpreted literally. This means that the target tracking methods that will be investigated should be easy to implement in the navigation system and have a reasonable computational complexity. The chosen algorithms should be applicable for real time implementation. Since the target tracking algorithms in this thesis only need to track one UAV, it simplifies the tracking process as opposed to having several targets.

In this thesis, it is important to make a distinction between the effects that will be observed as a result of multipath propagation. Multipath affects the PARS in two main ways. The first way is that the reflected signals interferes with the direct signal from the UAV. The second way is that the PARS sometimes chooses the reflected signal as if it was the direct signal when providing a position measurement. This effect has been observed in several papers mentioned in chapter 1.1.
From the problem description, a research questions, also known as a problem statement, that this thesis will attempt to answer is then formulated as follows:

"To what degree will low complexity single target tracking algorithms mitigate the effects of multipath propagation and increase the robustness of a PARS aided navigation system?"

The chosen metrics used to compare the implemented solution in this thesis is chosen to be the Mean Error(ME), Mean Absolute Error(MAE) accompanied by the calculated standard deviation(STD) of the estimation error. As well as the Root Mean Square Error(RMSE). The metrics are chosen since they have been used to display accuracy in previous work on the same system. By using the same metrics, the work performed in this thesis can easily be placed into the existing framework of research. Different error metrics also give a better overall view of the performance of the navigation system. RMSE is for instance known to be more affected by large individual errors than MAE. [20, p.80]

1.3 Contributions

The main contributions made in this thesis is formulated in the following list:

- Implementation of Nearest Neighbor- and Probabilistic Data Associtation algorithms in existing MATLAB toolbox. Details for accessing the code is given in appendix A.
- Testing the implemented solution on both a prerecorded- and synthetic dataset.
- Displaying whether single target tracking methods are suitable to handle the effect of multipath propagation in a PARS aided inertial navigation system.

1.4 Structure of thesis

The thesis starts with chapter 2 which gives an overview of the notation and different coordinate frames used in this thesis. Some formulas are also introduced. Chapther 3 introduces the reader to phased array radio systems, navigation systems and target tracking with related algorithms. Thereafter chapter 4 explains the setup of the MATLAB Toolbox and provided datasets, before chapter 5 presents the results of the test of the algorithms on pre-recorded flight data. The results are discussed in chapter 6 before a conclusion is presented in chapter 7.

Chapter 2

Mathematical prerequisites

This chapter introduces the mathematical notation used in this thesis. As the use of different coordinate frames and the relation between them are used in navigation, these are explained and presented in this chapter as well.

2.1 Vector and matrices

Vectors a written with bold lowercase letters, and matrices with bold uppercase letters. This means that $\boldsymbol{A}$ is a matrix, and $\boldsymbol{a}$ is a vector of arbitrary size. $\boldsymbol{A}^T$ and $\boldsymbol{a}^T$ denotes the transpose of the matrix and vector respectively. $I_n \in \mathbb{R}^{nxn}$ denotes the identity matrix with n as the number of elements along the diagonal of the matrix. The cross product of vector $\boldsymbol{a} = [a_1, a_2, a_3]^T$ and $\boldsymbol{b} = [b_1, b_2, b_3]^T$ is given by $\boldsymbol{a} \times \boldsymbol{b} = \boldsymbol{S}(\boldsymbol{a})\boldsymbol{b}$, where $\boldsymbol{S}(\boldsymbol{a})$ is a skew symmetric matrix given by equation 2.1.

$$\boldsymbol{S}(\boldsymbol{a}) = \begin{bmatrix} 0 & -a_3 & a_2 \\ a_3 & 0 & -a_1 \\ -a_2 & a_1 & 0 \end{bmatrix} \tag{2.1}$$

2.2 Statistics

A probability distribution that is fundamental to the Kalman filter(KF), is the Gaussian distribution. It is also known as the normal distribution. Since the KF is of great importance in this thesis, a brief introduction to this probability distribution is given. A vector of random variables, $\boldsymbol{x}$, distributed according to the multivariate Gaussian distribution is denoted $\boldsymbol{x} \sim \mathcal{N}(\bar{\mu}, \boldsymbol{P})$ where is $\bar{\mu} \in \mathbb{R}^n$ is the mean of the distribution, and $\boldsymbol{P} \in \mathbb{R}^{nxn}$ the corresponding covariance matrix. It

has the probability density function(PDF), $f(\boldsymbol{x})$ given by equation 2.2, where n is the dimension of $\boldsymbol{x}$.[21, Ch.3]

$$f(\boldsymbol{x}) = \frac{1}{(2\pi)^{\frac{n}{2}}|\boldsymbol{P}|^{\frac{1}{2}}} e^{(-\frac{1}{2}(\boldsymbol{x}-\bar{\boldsymbol{\mu}})\boldsymbol{P}^{-1}(\boldsymbol{x}-\bar{\boldsymbol{\mu}}))} \tag{2.2}$$

The calculation of the mean error(ME), mean absolute error(MAE) and root mean squared error(RMSE) is performed using equation 2.3, 2.4 and 2.5 respectively. Where x is the true value and $\hat{x}$ is the estimated value, while n is the total number of estimated values.

$$ME = \frac{1}{n}\sum_{i=1}^{n}(\hat{x}-x) \tag{2.3}$$

$$MAE = \frac{1}{n}\sum_{i=1}^{n}|\hat{x}-x| \tag{2.4}$$

$$RMSE = \sqrt{\frac{1}{n}\sum_{i=1}^{n}(\hat{x}-x)^2} \tag{2.5}$$

The statistical expectation of some stochastic variable x is denoted $\mathbb{E}[x]$.

2.3 Reference frames

Since this thesis deals with several reference frames, the notation that describes in which coordinate frame a vector is defined is described as follows. $\boldsymbol{p}^e_{eb}$ is the vector describing the position of a vehicle in the b-frame with respect to the e-frame, expressed in the e-frame coordinates, see [22, Ch.2].

The North-East-Down(NED) coordinate frame is denoted $\{n\} = (x_n, y_n, z_n)$. Where x_n and y_n points towards north and east respectively, while z_n points as a normal downwards to the earths center. The origin o_n of NED is typically defined on a tangent plane to earths surface on a specific location typically described by a specific longitude and latitude. However in this thesis it is defined in the center of the PARS ground antenna array.

The NED frame can be used in local navigation, as it approximates a frame that is tangent to the earths surface. This means that further away from the origin o_n, the approximation of a flat earth deteriorates. This flat earth approximation deliver accurate solutions within an area of $10x10km$. Although it is possible to use the NED frame for global navigation by moving the origin of the NED frame as the vehicle moves beyond the limits of the local NED frame.[22, p.19-20].

Another solution to this problem is to use the Earth-Centered-Earth-Fixed(ECEF) frame, denoted by $\{e\} = (x_e, y_e, z_e)$, as the reference frame. It is defined as the coordinate frame with its origin, o_e, at the center of the earth. It is fixed to the earth so that it rotates about z_e with the same rotational velocity as the earth. This means that the z_e points towards earths true north. The x_e-axis point towards 0^o longitude, which is where the equator and prime meridian crosses. y_e is defined using the right hand rule. Both x_e and y_e lie within the equatorial plane, which means at the plane described by a latitude of 0^o.[23, Ch.2.1.2]

The Earth-Centered-Inertial(ECI) frame, denoted $\{i\} = (x_i, y_i, z_i)$, is the inertial frame used in global navigation. It has its origin o_i that coincides with ECEF, but since ECI is inertial it does not rotate about z_i. x_i and y_i lie within the equatorial plane. The x_i-axis points in the direction between the earth and the sun druing vernal equinox in the northern hemisphere.[23, Ch.2.1.1] Figure 2.1 displays the defined coordinate frames with respect the the earth.

The BODY coordinate frame, denoted $\{b\} = (x_b, y_b, z_b)$, is a coordinate frame with an origin o_b which is fixed to the vehicle. In this thesis, the vehicle of interest is a fixed-wing UAV, in which

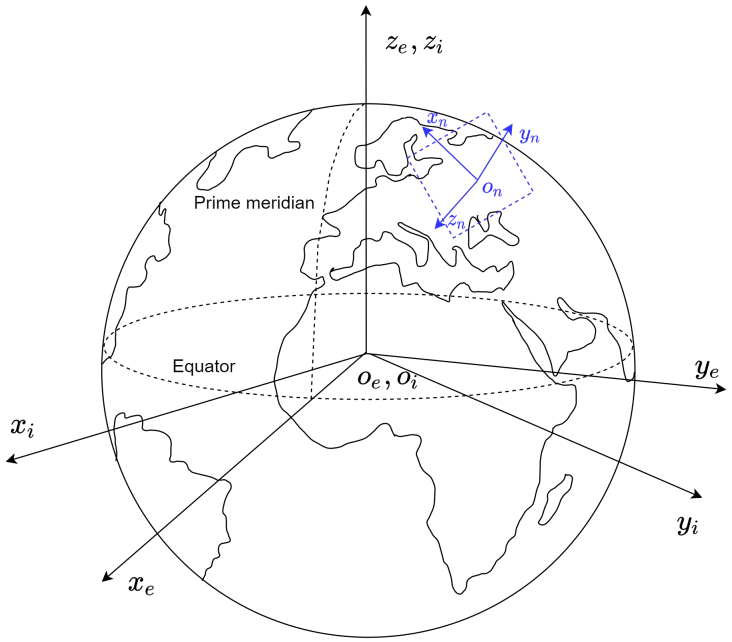

Figure 2.1: Visual definition of the {i}-, {e}- and {n}-frame. Based on figure in [22, p.19].

x_b, y_b and z_b are to chosen to point out the nose, right wing and out of the belly of the UAV respectively.[24, p.7]

The radio frame $\{r\} = (x_r, y_r, z_r)$ is the frame in which the PARS position measurements are defined. The origin of the radio frame is at the center of the PARS ground antenna. The only difference between the {r}-frame and {n}-frame in this thesis is that the {r}-frame is rotated by ψ_r degrees compared to the $\{n\}$-frame.[24, p.7] Figure 2.2 displays the relation between the {r}-, {n}- and {b}-frame.

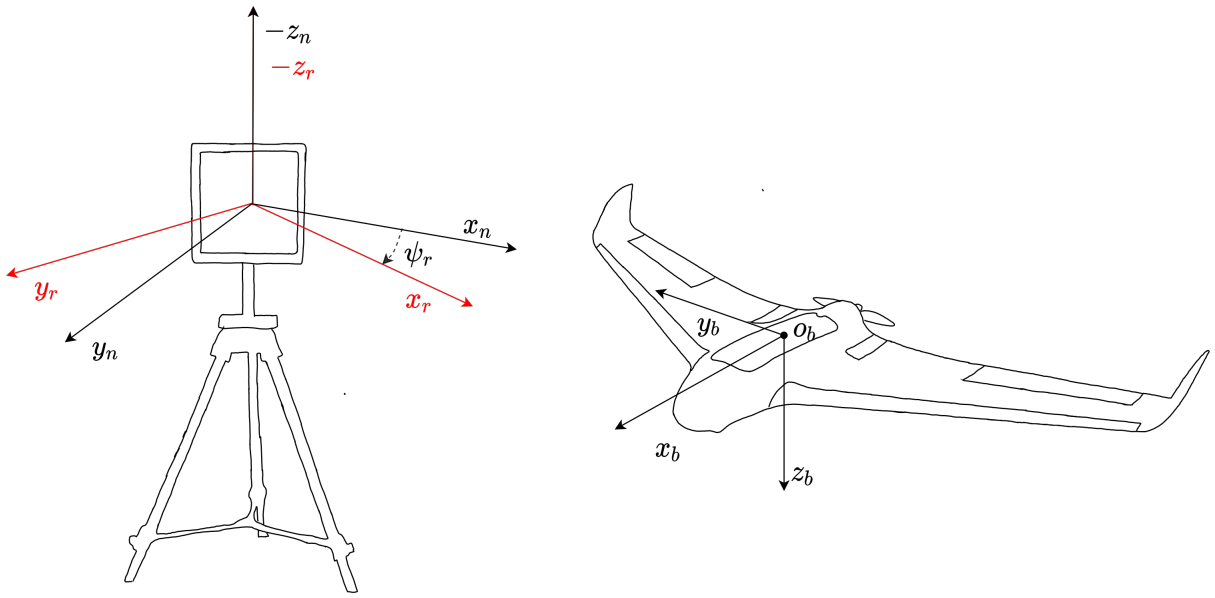

Figure 2.2: Visual definition of {r}-frame in relation to {n}-frame and the {b}-frame.

2.4 Representation of attitude

A 3-dimentional orientation between two coordinate frames, knowns as attitude, can be parameterized by euler angles $\boldsymbol{\Theta} = [\phi, \theta, \psi]$, where ϕ is known as the pitch angle, θ as the roll angle and ψ the yaw angle.
Euler angles are related to the rotation matrix $\boldsymbol{R}(\boldsymbol{\Theta}) \in SO(3)$ in equation 2.6. Where $s(*)$ and $c(*)$ is short for $sin(*)$ and $cos(*)$ respectively.

$$\boldsymbol{R}(\boldsymbol{\Theta}) = \begin{bmatrix} c\theta s\psi & -c\theta s\psi 0 s\phi s\theta c\psi & s\phi s\psi + c\phi s\theta c\psi \\ c\theta s\psi & c\phi c\psi + s\phi s\theta s\psi & -s\theta c\psi + c\phi s\theta s\psi \\ -s\theta & s\phi c\theta & c\phi c\theta \end{bmatrix} \tag{2.6}$$

The rotation from coordinate frame 1 frame to coordinate frame 2 is denoted as $\boldsymbol{R}_1^2$. An example is the rotation from the {n}-frame and {e}-frame is known as the longitude and latitude rotation matrix, $\boldsymbol{R}_n^e(l_{lon}, l_{lat})$, where l_{lon} is the longitude and l_{lat} is the latitude of a point on the earths surface. It is given in equation 2.7.[22, p.40]

$$\boldsymbol{R}_n^e(l_{lon}, l_{lat}) = \begin{bmatrix} -c(l_{lon})s(l_{lat}) & -s(l_{lon}) & -c(l_{lon})c(l_{lat}) \\ -s(l_{lon})s(l_{lat}) & c(l_{lon}) & -s(l_{lon})c(l_{lat}) \\ c(l_{lat}) & 0 & -s(l_{lat}) \end{bmatrix} \tag{2.7}$$

Using euler angles, $\boldsymbol{\Theta}_b^e$ to represent the attitude of a UAV {b}-frame with respect to the {e}-frame may be problematic as it becomes singular when the pitch angle, $\theta = 90^o$. This motivates the use of the unit quaternion $\boldsymbol{q} = [q_w, \boldsymbol{q}_v]^T \in \mathbb{Q}$ for the UAV attitude representation. Where $\mathbb{Q}$ is the set of unit quaternions $\mathbb{Q} = \{\boldsymbol{q} \mid \boldsymbol{q}^T\boldsymbol{q} = 1, \boldsymbol{q} = [q_w, \boldsymbol{q}_v]^T, q_w \in \mathbb{R}^1 \text{ and } \boldsymbol{q}_v \in \mathbb{R}^3\}$.[22, p.32-33] Note that this thesis uses the Hamiltonian representation of the unit quaternion as in [24].

The rotation matrix between the {b}- and {e}-frame can also be obtained by using equation 2.8 if $\boldsymbol{q}$ is the unit quaternion describing the orientation between the aforementioned frames.

$$\boldsymbol{R}_b^e(\boldsymbol{q}) = \boldsymbol{I}_3 + 2q_w\boldsymbol{S}(\boldsymbol{q_v}) + 2\boldsymbol{S}^2(\boldsymbol{q_v}) \tag{2.8}$$

The hamiltonian quaternion product, denoted $\otimes$, is performed as in equation 2.9.[22, ch.2.2.2]

$$\boldsymbol{q}_1 \otimes \boldsymbol{q}_2 = \begin{bmatrix} q_{w_1} q_{w_2} - \boldsymbol{q}_{v_1}^T \boldsymbol{q}_{v_2} \\ q_{w_1} \boldsymbol{q}_{v_2} + q_{w_2} \boldsymbol{q}_{v_1} + \boldsymbol{S}(\boldsymbol{q}_{v_1}) \boldsymbol{q}_{v_2} \end{bmatrix} \tag{2.9}$$

Chapter 3

Theory

This chapter presents the theory deemed necessary to understand the work performed in this thesis. It starts by introducing phased array radio systems(PARS) and how they are used to obtain spherical position measurements. The effects of multipath propagation is also presented before the focus switches to navigation systems and single target tracking methods.

3.1 Phased array radio systems

A Phased array antenna is a configuration of several antenna elements, most often in a linear or planar manner. The most common antenna geometries are linear-, rectangular- or circular antenna arrays. The configuration of several radiating antennas in combination with a feed network which consists of components such as amplifiers and phase-shifters makes up the entire phased array antenna system. The phase-shifters are used to adjust the phase of the transmitted signal from each individual antenna element. By doing this it is possible to steer the main beam of the antenna array towards some direction of interest. In the case of a linear antenna array the angle of interest is one dimensional, while for rectangular or circular configurations it is two dimensional. Steering a phased array antenna is therefore also known as beamforming.[25]

Phased array antennas can also receive incoming signals. By measuring the difference in phase between the same signal received at different antennas with known positions, it is possible to estimate the direction of arrival(DoA) of the incoming signal. Several DoA algorithms rely on the assumption that the signal received from a far field source at each antenna element has a narrow bandwidth and is affected by additive Gaussian white noise with a common variance σ^2_{DoA}.[26, ch.3] By assuming that the source is far away the signal can be considered to be a plane wave

such as in figure 3.1. It displays the fact that the signal will be received at the rightmost antenna first and the leftmost last. This time-delay corresponds to a phase-shift. Although the figure displays a one dimensional case with a linear antenna array, many DoA algorithms can easily be expanded to work in the two dimensional case as well. For a more thorough introduction to DoA algorithms and the underlying mathematics, the reader is referred to [26] by Chen et.al.

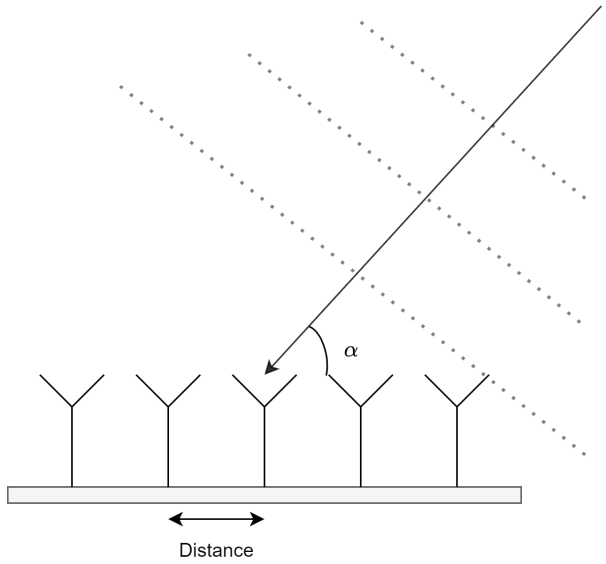

Figure 3.1: A sketch of a linear antenna array where an incoming signal impinges on the antenna with an angle of α. The signal will use a longer path before being received at the antennas to the left.

Phased array antennes where originally developed for radar applications, although it has also found use in communication applications.[25] This is the case for the PARS used in this thesis, see chapter 1.1. The papers presented in chapter 1.1 uses the Radionor $CRE2-189$[14] antenna as ground station, while the UAV uses the $CRE2-144-LW$[15]. To obtain the direction towards the UAV the ground station antenna sends a directed signal which the UAV antenna responds to. The distance between the ground station and UAV antennas can then be estimated by using the recorded RTT and subtracting the internal processing time. The full spherical position of the UAV, given be a range, azimuth- and elevation angle, is then obtained by DoA estimation of the received signal at ground station.[16]. Figure 3.2 displays how the range, ρ, azimuth-, ξ and elevation angle, α is defined in the {r}-frame. Where origin of the frame is placed at the center of the PARS ground antenna.

There exists several DoA algorithms such as the well established MUSIC algorithm[27] or a more

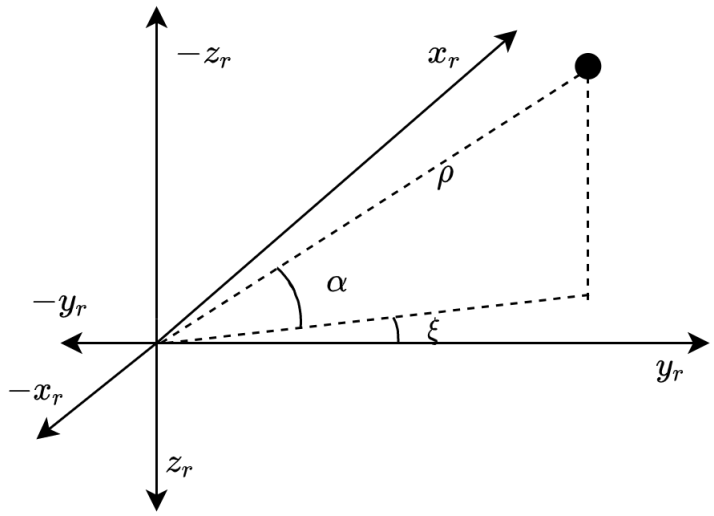

Figure 3.2: Definition of the range, ρ, azimuth, ξ and elevation angle, α with respect to the radio frame.

recent algorithm known as PDDA[28]. Both algorithms estimates what is known as a pseudospectrum. An example of a pseudospectrum produced by the DoA algorithm in the PARS used in this thesis is shown in figure 3.3. One received signal is expected, therefore the indices of the largest peak corresponds to the DoA of the signal. If n signals were expected, then the n largest peaks would correspond to the different DoAs.

The DoA algorithm in the Radionor system is considered a black box. It is therefore assumed that some DoA algorithm in combination with range estimation from RTT delivers spherical position measurement in the {r}-frame which is affected by additive Gaussian white noise $\epsilon_* \sim \mathcal{N}(0, \sigma_*^2)$ as in equation 3.1 - 3.3. Where ρ is the measured range, ξ is the measured azimuth angle and α is the measured elevation angle.

$$\rho = \rho_u + \epsilon_\rho \tag{3.1}$$

$$\xi = \xi_u + \epsilon_\xi \tag{3.2}$$

$$\alpha = \alpha_u + \epsilon_\alpha \tag{3.3}$$

In order to use the PARS position measurement as an aiding measurement to the INS it is must be mapped from spherical- to cartesian coordinates via equation 3.4. It is worth mentioning that this nonlinear mapping will as discussed in [24, Ch.14.2.1] by Gryte, result in biases in the Cartesian position. Gryte solves this by debiasing the measurement.

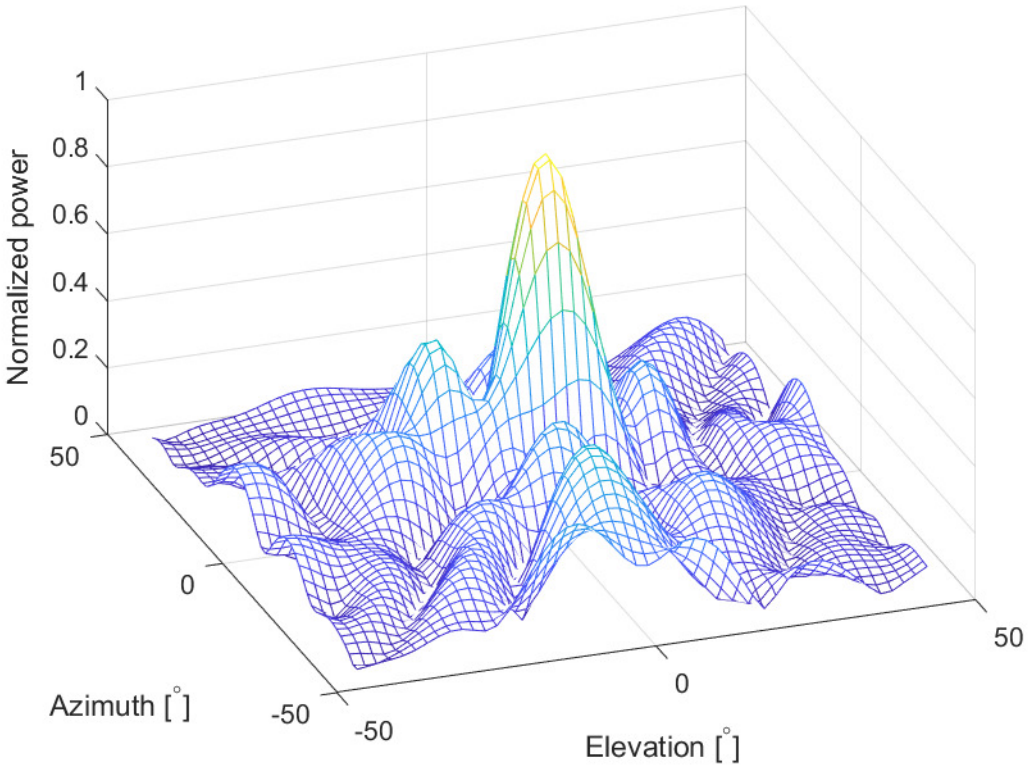

Figure 3.3: Pseudospectrum produced by the PARS ground antenna while the UAV is mid flight.

$$\boldsymbol{p}^r_{rb} = \begin{bmatrix} p^r_{rb,x} \\ p^r_{rb,y} \\ p^r_{rb,z} \end{bmatrix} = \rho \begin{bmatrix} \cos(\xi)\cos(\alpha) \\ \sin(\xi)\cos(\alpha) \\ -\sin(\alpha) \end{bmatrix} \tag{3.4}$$

Since the INS propagates the position of the UAV in the {e}-frame is rotated to this frame as in equation 3.5. This is done with the help of the rotation matrix $\boldsymbol{R}^e_r = \boldsymbol{R}^e_n(l_{lon}, l_{lat})\boldsymbol{R}^n_r(\boldsymbol{\Theta_{PARS}})$. $\boldsymbol{\Theta}_{PARS}$ is the orientation between the {n}-frame and the {r}-frame. And l_{lon} and l_{lat} describes the longitude and lattitude of the PARS ground antenna.

$$\boldsymbol{p}^e_{eb} = \boldsymbol{p}^e_{er} + \boldsymbol{R}^e_r \boldsymbol{p}^r_{rb} \tag{3.5}$$

The PARS positions measurements are used in a Multiplicative Extended Kalman Filter, and knowledge of the uncertainty of the position measurement, in the form of a covariance matrix, $\boldsymbol{R}_s$, is therefore needed. The mapping from spherical- to Cartesian coordinates also makes it necessary to map the covariance. $\boldsymbol{R}_s$ is defined in equation 3.6.

$$\boldsymbol{R}_s = \begin{bmatrix} \sigma_\rho^2 & 0 & 0 \\ 0 & \sigma_\xi^2 & 0 \\ 0 & 0 & \sigma_\alpha^2 \end{bmatrix} \tag{3.6}$$

Reiterated from Grytes PhD thesis [24, Ch.14.2.1], the matrix that maps the covariance from spherical to cartesian coordinates, $\boldsymbol{M}$, is found by computing the jacobian matrix of the position with respect to measurement noise as in equation 3.7. Where $\boldsymbol{\epsilon_{pos}} = [\epsilon_\rho, \epsilon_\phi, \epsilon_\theta]$.

$$\boldsymbol{M} = \frac{\partial \boldsymbol{p}_{rb}^e}{\partial \boldsymbol{\epsilon}_{pos}} = \begin{bmatrix} \cos(\xi)\cos(\alpha) & -\rho\cos(\alpha)\sin(\xi) & -\rho\cos(\xi)\sin(\alpha) \\ \cos(\alpha)\sin(\xi) & \rho\cos(\xi)\cos(\alpha) & -\rho\sin(\xi)\sin(\alpha) \\ \sin(\alpha) & 0 & -\rho\cos(\alpha) \end{bmatrix} \tag{3.7}$$

The covariance matrix $\boldsymbol{R}_s$ is then first mapped into the Cartesian {r}-frame, before it again is mapped into the {e}-frame in two sequential similarity transforms as in equation 3.8.

$$\boldsymbol{R}_{PARS} = \boldsymbol{R}_r^e \boldsymbol{M} \boldsymbol{R}_s \boldsymbol{M}^T \boldsymbol{R}_e^r \tag{3.8}$$

3.2 Multipath propagation

As this thesis focuses on mitigating the multipath problem affecting the PARS it is important to have a fundamental understanding of what effects will be observed as a result.

Multipath is a common phenomenon in which a radio signal reaches the receiving antenna via more paths than the direct path. It will affect almost all radio communication systems. A simple sketch displaying a multipath scenario which is of interest in this thesis is displayed in figure 3.4. Both the direct signal from the UAV and the same signal reflected from the ocean is received at the ground antenna array.

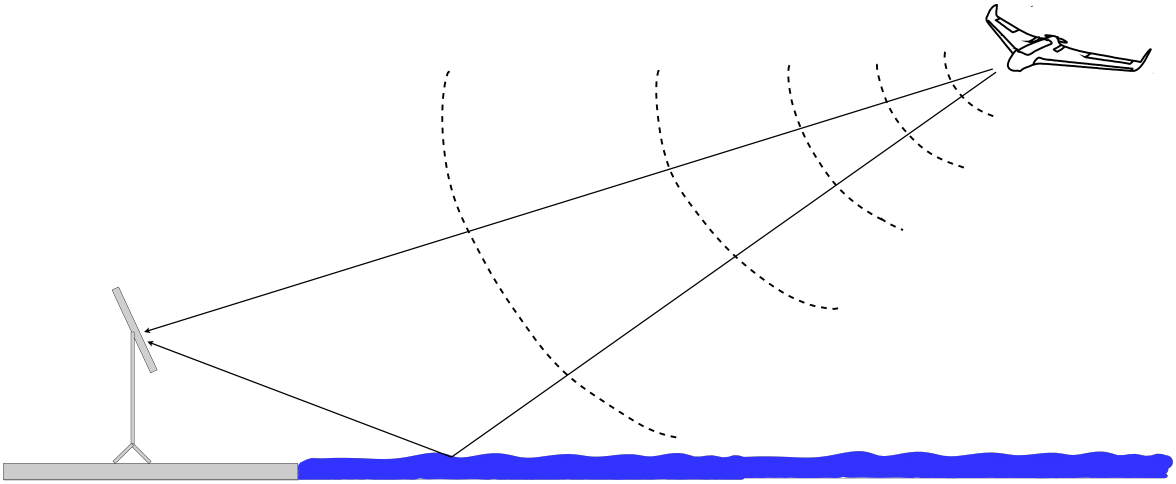

Figure 3.4: Sketch displaying the multipath problem in the PARS based navigation system. As the UAV flies above water, the reflected signal also reaches the PARS ground antenna array.

In different scenarios, the reason for multipath propagation will vary. In figure 3.4 the signal is reflected from the ocean surface. Other ways multipath can occur is due to diffraction. It is when an object with sharp edges blocks the signal, resulting in bending the signal around the object. Scattering of the signal into multiple directions will also happen if it impinges on smaller rough surfaces.[29, Ch.5.4]

The effect of the mentioned scenarios will vary depending on the signals frequency and wavelength. As some frequencies may be more heavily distorted than other for a given range and angle of arrival in different weather conditions. From this it can be understood that there are many variables that plays into how severe the multipath propagation will affect the direct radio signal at the receiving end.[30, ch.7]

Multipath signals will use a longer path to reach the receiving antenna, and as a result be subject to a phase-shift. The phase shifted signals will interfere with the direct signal and distort it. The phase-shifted multipath signals may attenuate or amplify the direct signal based on whether the multipath signal is in phase or not with the direct signal. In some instances the multipath signal might cancel out the direct signal almost entirely if their phases are opposite.[29, Ch.5.5] How much each multipath signal will distort the direct signal, depends on how much energy was reflected towards the receiving antenna. Reflections from smoother surfaces will be coherent with the direct signal. These reflections often have the greatest effect as most of the signal energy is reflected toward the receiver. Scattering on the other hand results in less distortion on the direct signal as less energy is reflected towards the receiver antenna. It will look more like noise on the direct signal.[30, ch.7]

The distortion of the direct signal will cause its amplitude, phase and therefore it's DoA to be distorted as well. This effect can be observed in the raw PARS spherical position measurements. It seems to especially effect the elevation angle. By mapping the spherical PARS position measurement to Cartesian coordinates, and rotating it to the in the {n}-frame, it can be compared to the GNSS measurements. Figure 3.5 displays how the reflected signals seems to affect the direct signal more as the distance between the UAV and the ground station increases.

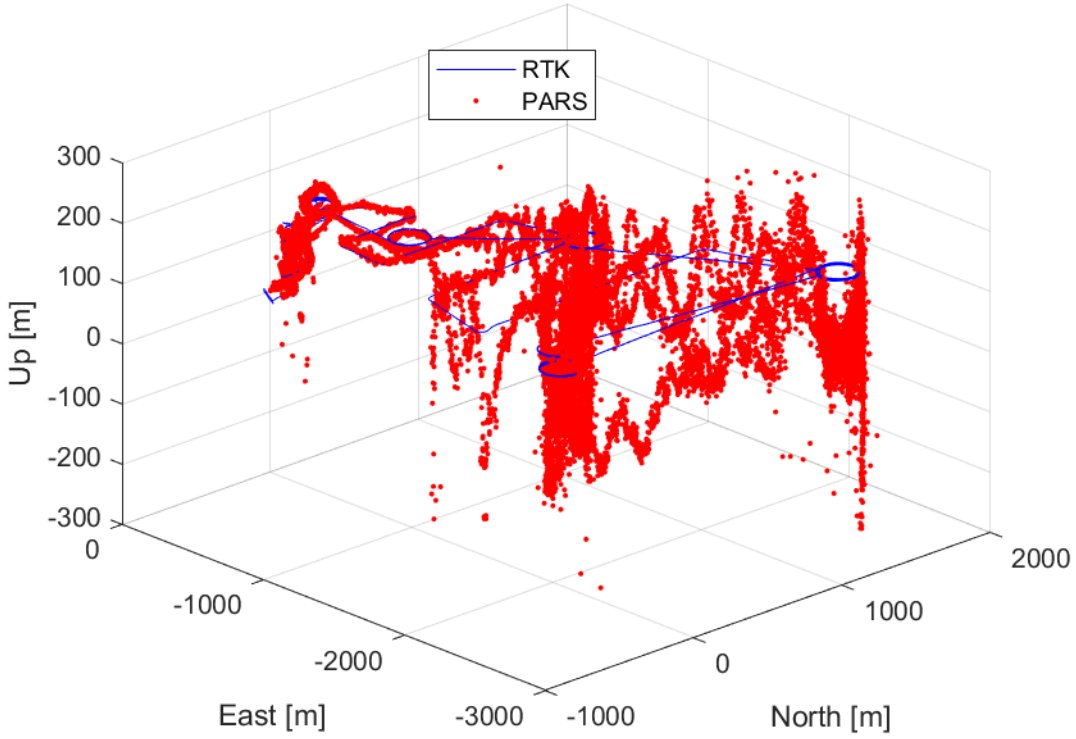

Figure 3.5: 3D PARS position measurements through the duration of the UAVs flight compared to RTK-GNSS.

Figure 3.6 shows how the multipath interference is effecting the horizontal measurement on a much smaller relative scale. Although it affects the position measurement more the further away it is from the PARS ground antenna array.

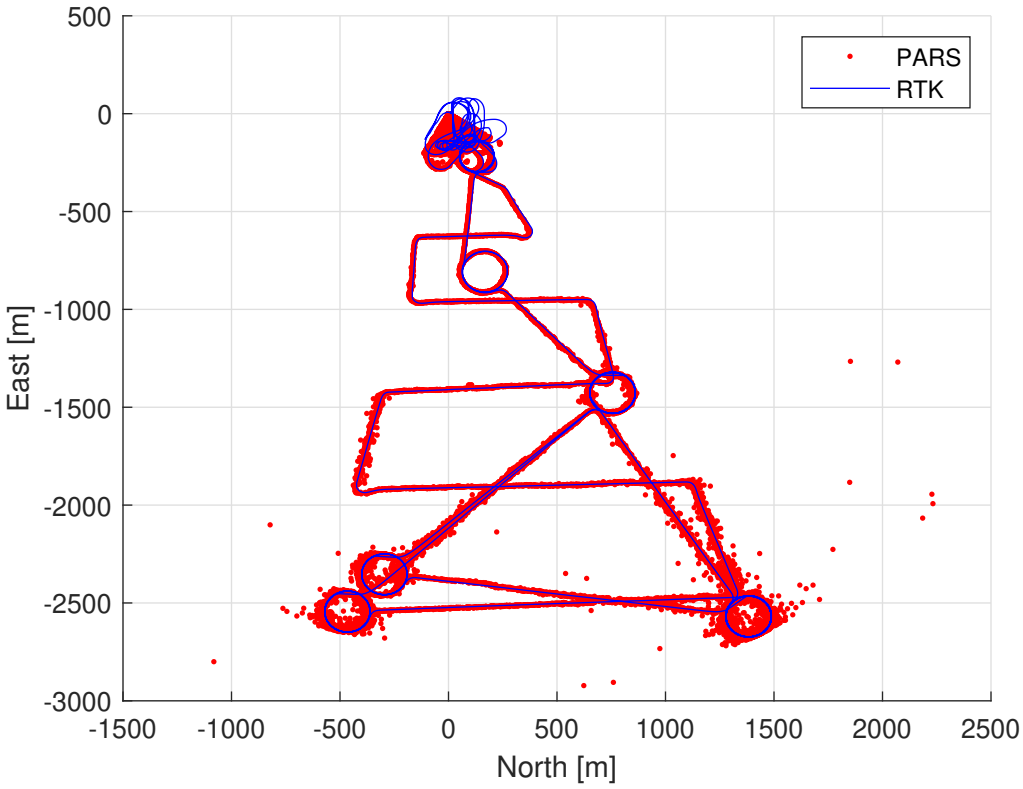

Figure 3.6: 2D measurements of the PARS measurements through the duration of the flight compared to RTK-GNSS.

The reason for the large position errors in the vertical measurements seems to originate from the oscillations that occur mid-flight in the PARS measured elevation angle. These oscillations are likely caused from interference between the direct signal and the reflected signals. Figure 3.7 shows that it oscillates with an amplitude of about 2.5^o.

There exists some techniques for mitigating the effect of multipath. An example for radar is only considering the leading edge of the received radio frequency waveform and discarding the rest as affected by multipath. This is because the multipath signals will have some delay compared to the direct signal. The position of the receiving antennas can also influence how much of an affect the multipath signals will have. Antenna design for mitigating multipath interference is also of importance.[30, Ch.7.8]

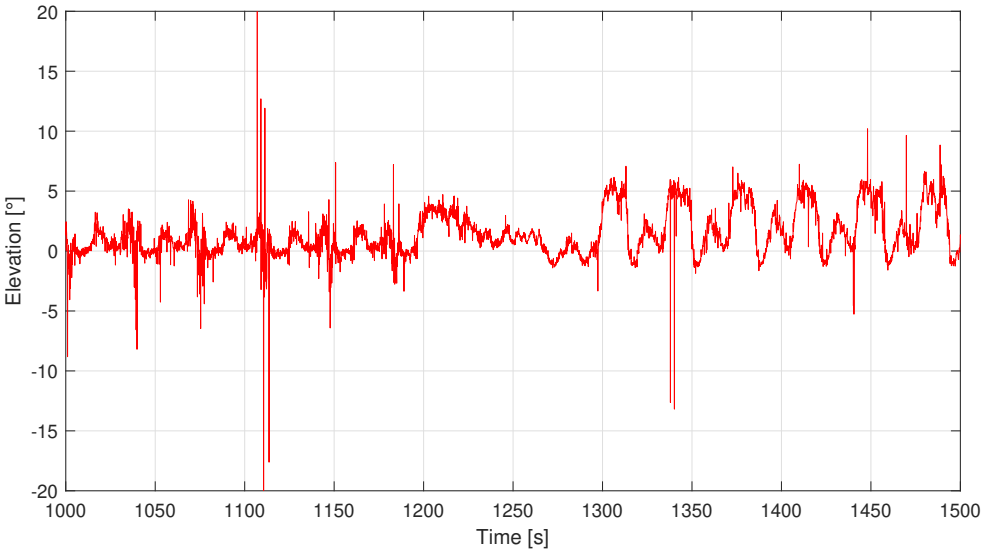

Figure 3.7: Oscillations in mid-flight elevation angle measurements of the direct signal transmitted from the UAV

3.3 Navigation systems

Navigation can be defined as the problem of calculating the position and velocity of some vehicle or aircraft with respect to some fixed reference frame such as the {n}- or {e}-frame. The navigation system may also produce estimates of an aircraft's heading and attitude. This is often done by fusing measurements from different sensors such as accelerometers and gyroscopes, but also other systems such as GNSS.

Depending on the application, different requirements in terms of accuracy can be expected from the navigation system. For safety critical tasks such as airliners and aircrafts in general, the tolerated positioning and velocity errors may be much more strict than for other applications. For such tasks it is also important to have a fault detection system in place. This enables the navigation system to detect in which component of the navigation system where a fault is present. The navigation solution can thereby by adapt to this by removing the faulty sensor data from the navigation solution. This is also known as integrity monitoring.[23, Ch.1]

A typical navigation system consists of three components. A dead reckoning system, a position fixing system and an estimation algorithm. A dead reckoning system calculates the current position by integrating measurements of for instance the velocity of the vehicle. This is added to the previous position estimate to obtain the current position. It is also possible to perform dead reckoning with a mathematical model instead of with sensor measurements. An example of a dead reckoning system is an Inertial Navigation System(INS) which processes measurements from an IMU to obtain a position estimate. Due to measurement noise and inherent biases in the IMU, the error of the position estimate accumulates over time. This creates the need for aiding measurements from a position fixing system. An example of a position fixing system is GNSS which can provide a more reliable estimate of the position and velocity of the vehicle, at a lower rate than the dead reckoning system.[23, Ch.1] An estimation algorithm such as the KF[31] or a nonlinear observer[22, Ch.13.5] then uses the aiding measurement to make corrections to the dead reckoning solution.

3.3.1 Inertial Navigation Systems

This thesis is concerned with a strapdown Inertial Navigation System(INS). It consists of an IMU that is strapped to the body of the vehicle and a computer that integrates what is known as the strapdown navigation equations. The strapdown navigation equations uses the IMU measurements as input, and are precise equations that the describe the kinematics of the vehicle. The IMU contains at least a 3-axis accelerometer and 3-axis angular rate sensor known as gyroscopes. Other sensors such as magnetometers are also sometimes included in an IMU. [22, p.443-44] It is here assumed that the the IMU measurement frame is aligned with the vehicle {b}-frame with a shared origin. If this was not the case, the IMU measurements would need to transformed into the {b}-frame. .

A 3-axis accelerometer measures specific force, $\boldsymbol{f}_{ib}^{b} \in \mathbb{R}^3$. The specific force is defined as non-gravitational force per mass unit. This means that the specific force by definition is an acceleration, not a force, even though the word force is used to describe it. A 3-axis gyroscope measures the angular velocity $\boldsymbol{\omega}_{ib}^{b} \in \mathbb{R}^3$ of the IMU body with respect to the inertial {i}-frame.[22, p.446] It is also referred to as an attitude rate sensor(ARS). Because all accelerometers and gyroscopes to some degree will exhibit both biases and measurement noise, a model of the IMU measurements is needed. In Grytes PhD thesis[24, Ch.14.3.1] the IMU measurements are modeled as in equation 3.9 and 3.10, which provide specific force and angular rate respectively, both influenced by their respective biases and measurement noise. Where $\boldsymbol{b}_{*}^{b}$ are the biases effecting the IMU measurements, $\boldsymbol{\epsilon}_{*}^{b}$ the noise which is assumed to be Gaussian white noise distributed according to $\boldsymbol{\epsilon}_{*}^{b} \sim \mathcal{N}(0, \sigma_{*}^{2})$.

$$\boldsymbol{f}_{imu}^{b} = \boldsymbol{f}_{ib}^{b} + \boldsymbol{b}_{acc}^{b} + \boldsymbol{\epsilon}_{acc}^{b} \tag{3.9}$$

$$\boldsymbol{\omega}_{imu}^{b} = \boldsymbol{\omega}_{ib}^{b} + \boldsymbol{b}_{ars}^{b} + \boldsymbol{\epsilon}_{ars}^{b} \tag{3.10}$$

By utilizing the sensor model and knowledge of the kinematics of the vehicle with respect to the {e}-frame, the strapdown navigation equations are presented as follows.
The position of the vehicle is described by the relationship in equation 3.11.

$$\dot{\boldsymbol{p}}_{eb}^{e} = \boldsymbol{v}_{eb}^{b} \tag{3.11}$$

The equation describing the velocity of the vehicle is more complicated due to the fact that the {e}-frame rotates with respect to the inertial {i}-frame. It is given in equation 3.12. The earth ro-

tates with the angular velocity $\boldsymbol{\omega}^e_{ie} = [0, 0, \omega^e_{ie}]$. The kinematic equation for velocity is dependent not only on the specific force, but also the Coriolis acceleration due to the rotating resolving frame.[23, Ch.5.2] The gravitational acceleration, $\boldsymbol{g}^e_b$, is dependent on the specific location on the earths surface. Hence it is calculated using a model called the World Geodetic System which is described in [p.448][22] by Fossen.

$$\dot{\boldsymbol{v}}^e_{eb} = \boldsymbol{g}^e_b(\boldsymbol{p}^e_{eb}) - 2\boldsymbol{S}(\boldsymbol{\omega}^e_{ie})\boldsymbol{v}^e_{eb} + \boldsymbol{R}^e_i \boldsymbol{f}^b_{ib} \tag{3.12}$$

The attitude kinematics of the vehicle in {e} coordinates is defined as in equation 3.13. Where the matrices $\boldsymbol{\Omega}(\boldsymbol{\omega}^b_{ib})$ and $\boldsymbol{\Gamma}(\boldsymbol{\omega}^e_{ie})$ are given in equation 3.14 and 3.15 respectively. The unit quaternion is used to avoid singularities, which are a well known problem with Euler angles. The first part of the right side of equation 3.13 accounts for the rotation of the {b}-frame of the vehicle with respect to the {i}-frame. While the second part accounts for the rotation of the {e}-frame, the earth, with respect to the {i}-frame, the intertial frame.[23, Ch.5.2]

$$\dot{\boldsymbol{q}}^e_b = \frac{1}{2}\boldsymbol{\Omega}(\boldsymbol{\omega}^b_{ib})\boldsymbol{q}^e_b - \frac{1}{2}\boldsymbol{\Gamma}(\boldsymbol{\omega}^e_{ie})\boldsymbol{q}^e_b \tag{3.13}$$

$$\boldsymbol{\Omega}(\boldsymbol{\omega}^b_{ib}) = \begin{bmatrix} \boldsymbol{0} & -\boldsymbol{\omega}^{b\ T}_{ib} \\ \boldsymbol{\omega}^b_{ib} & -\boldsymbol{S}(\boldsymbol{\omega}^b_{ib}) \end{bmatrix} \tag{3.14}$$

$$\boldsymbol{\Gamma}(\boldsymbol{\omega}^e_{ie}) = \begin{bmatrix} \boldsymbol{0} & -\boldsymbol{\omega}^{e\ T}_{ie} \\ \boldsymbol{\omega}^e_{ie} & \boldsymbol{S}(\boldsymbol{\omega}^e_{ie}) \end{bmatrix} \tag{3.15}$$

Integrating the strapdown navigation equations results in a nominal state estimate $\boldsymbol{x}^e_{eb,nom} = [\boldsymbol{p}^e_{eb,nom}, \boldsymbol{v}^e_{eb,nom}, \boldsymbol{q}^e_{eb,nom}, \boldsymbol{b}^b_{acc,nom}, \boldsymbol{b}^b_{ars,nom}]^T \in \mathbb{R}^{16}$. It should be noted that the IMU biases are included in the state, because it is of interest to estimate them. As in [24, Ch.14.3.1] the specific force- and angular rate used in the nominal state strapdown equations are defined as in equation 3.16-3.17.

$$\hat{\boldsymbol{f}}^i_{ib} = \boldsymbol{f}^b_{imu} - \boldsymbol{b}^b_{acc,nom} \tag{3.16}$$

$$\hat{\boldsymbol{\omega}}^i_{ib} = \boldsymbol{\omega}^b_{imu} - \boldsymbol{b}^b_{ars,nom} \tag{3.17}$$

The nominal bias model for both the accelerometer and gyroscope is defined as Gauss-Markov processes as in equation 3.18 and 3.19, with time constants $\boldsymbol{T}_{acc} = T_{acc}\boldsymbol{I}_3$ and $\boldsymbol{T}_{ars} = T_{ars}\boldsymbol{I}_3$.

$$\dot{\boldsymbol{b}}^b_{acc,nom} = -\boldsymbol{T}^{-1}_{acc}\boldsymbol{b}^b_{acc,nom} \tag{3.18}$$

$$\dot{\boldsymbol{b}}^b_{ars,nom} = -\boldsymbol{T}^{-1}_{acc}\boldsymbol{b}^b_{ars,nom} \tag{3.19}$$

The nominal bias model is used in the strapdown navigation equations, that are summarized in equation 3.20-3.22.

$$\dot{\boldsymbol{p}}^e_{eb,nom} = \boldsymbol{v}^b_{eb,nom} \tag{3.20}$$

$$\dot{\boldsymbol{v}}^e_{eb,nom} = \boldsymbol{g}^e_b(\boldsymbol{p}^e_{eb,nom}) - 2\boldsymbol{S}(\boldsymbol{\omega}^e_{ie})\boldsymbol{v}^e_{eb} + \boldsymbol{R}^e_b\hat{\boldsymbol{f}}^b_{ib} \tag{3.21}$$

$$\dot{\boldsymbol{q}}^e_{b,nom} = \frac{1}{2}\boldsymbol{\Omega}(\boldsymbol{\omega}^b_{ib})\boldsymbol{q}^e_{b,nom} - \frac{1}{2}\boldsymbol{\Gamma}(\boldsymbol{\omega}^e_{ie})\boldsymbol{q}^e_{b,nom} \tag{3.22}$$

3.3.2 Model based navigation systems

Another available approach when developing a navigation system is using a mathematical model of the vehicle. Conventional ships and underwater vehicles often use a model-based navigation system [22, p.387]. Without going into too much detail, a brief explanation is provided. The model based approach utilizes a kinetic model of the vehicle. A kinetic model is a description of how the forces applied on the vehicle causes motion. It is derived using Newtons laws of motion. This is fundamentally different to the strapdown equations used in an INS, as these provide a geometric description of the vehicles motion. The model works as a predictor, in the sense that it takes the control inputs of the vehicle in the current time step, and predicts the state vector in the next time step. Figure 3.8 describes the difference between the two navigation system approaches.[22, Ch.13]

An obvious drawback of the model-based approach is the fact that a kinetic model will have to be developed. This is both time consuming and will introduce modeling errors. Compared to an INS which uses a geometrical description, the strapdown navigation equations, which aren't prone to parameter errors.[22, p.457] On the other hand, a mathematical model can be used to make predictions of where the vehicle may be positioned in the next time step. The model based approach may also works without an IMU, although these measurements can also be fused into the navigation solution by using for instance a KF, for redundancy and a more reliable navigation solution.[22, Ch.13]

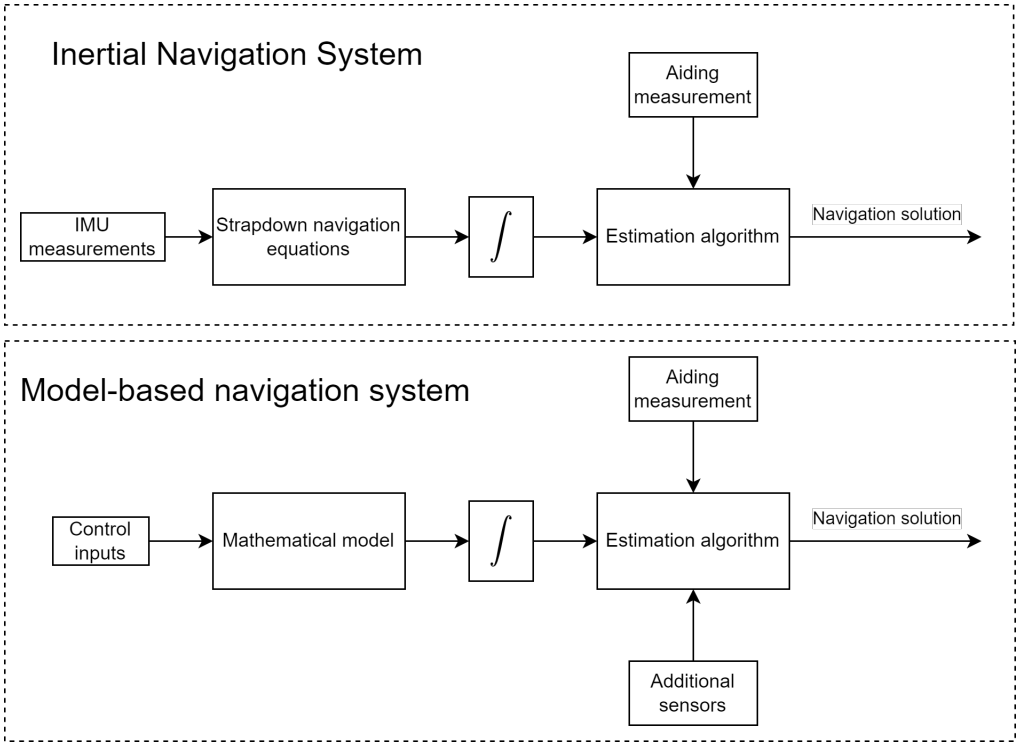

Figure 3.8: Architectures for model-based- and intertial navigation system. The figure is based on [22, p.388] by Fossen.

3.4 The Kalman Filter and it's error-state formulation

A very famous and widely used estimation algorithm in many navigation system today is the Kalman filter(KF)[31], which was first proposed by R. E. Kalman in 1960 in it's simplest form. It combines the available noisy measurements into an optimal estimate of the state vector $\boldsymbol{x}$. Optimal in the KF sense, means to obtain the minimum mean square error estimate of the state vector.[32, p.6] The KF assumes that the system- and measurement model are both linear as in equation 3.23 and 3.24 respectively, where $\boldsymbol{A}$ is the discrete system matrix, also known as the transition matrix, $\boldsymbol{B}$ is the control input matrix, and $\boldsymbol{C}$ is the measurement matrix. Equation 3.23 and 3.24 are both discrete, which is necessary for implementation in a computer. The models are also assumed to be affected by zero-mean Gaussian noise, distributed according to equation 3.25 and 3.26. Where $\boldsymbol{Q}$ is known as the process noise covariance, and $\boldsymbol{R}$ the measurement noise covariance.

$$\boldsymbol{x}[k+1] = \boldsymbol{A}[k]\boldsymbol{x}[k] + \boldsymbol{B}[k]\boldsymbol{u}[k] + \boldsymbol{v}[k] \tag{3.23}$$

$$\boldsymbol{y}[k] = \boldsymbol{C}[k]\boldsymbol{x}[k] + \boldsymbol{w}[k] \tag{3.24}$$

$$\boldsymbol{v}[k] \sim \mathcal{N}(0, \boldsymbol{Q}) \tag{3.25}$$

$$\boldsymbol{w}[k] \sim \mathcal{N}(0, \boldsymbol{R}) \tag{3.26}$$

The KF first obtains what is known as an a priori estiamte of the state, $\hat{\boldsymbol{x}}^-$, and the state estimation error covariance , $\boldsymbol{P}^-$, by using equation 3.27 and 3.28. This is called the prediction step, as the KF predicts the values of the state vector and covariance in the next time step given the current estimate $\hat{\boldsymbol{x}}$. [33, p.6]

$$\hat{\boldsymbol{x}}^-[k+1] = \boldsymbol{A}[k]\hat{\boldsymbol{x}}[k] + \boldsymbol{B}[k]\boldsymbol{u}[k] \tag{3.27}$$

$$\boldsymbol{P}^-[k+1] = \boldsymbol{A}[k]\boldsymbol{P}[k]\boldsymbol{A}^T[k] + \boldsymbol{Q}[k] \tag{3.28}$$

Once a measurement is available, the update step is performed. This step involves first calculating the Kalman gain, $\boldsymbol{K}$, using equation 3.29. The Kalman gain is the optimal weighting of between the predicted state and the measured state. It thereby minimizes the a posteriori state estimation error covariance, $\boldsymbol{P}$, which describes the uncertainty of the state vector estimate, and the correlation between the errors of the state estimates. The a posterior state and covariance estimate is obtained by applying equation 3.31 and 3.32. Where the predicted measurement

$\hat{\boldsymbol{y}}[k]$ is given by equation 3.30. An important note about the covariace matrix is that the correlations can increase between the measurement intervals. This means that if the measurement itself does not contain enough information to estimate the full state vector, it might still be possible due to the information contained in the covariance matrix.[23, p.56] An example of this is the fact the Gryte et.al [13] was able to remove dedicated heading measurement when using a version of the KF as the estimation algorithm in the PARS aided navigation system, as opposed to using a nonlinear observer setup.

$$\boldsymbol{K}[k] = \boldsymbol{P}^{-}[k]\boldsymbol{C}[k]^{T}(\boldsymbol{C}[k]\boldsymbol{P}^{-}[k]\boldsymbol{C}[k]^{T} + \boldsymbol{R}[k])^{-1} \tag{3.29}$$

$$\hat{\boldsymbol{y}}[k] = \boldsymbol{C}[k]\hat{\boldsymbol{x}}^{-}[k] \tag{3.30}$$

$$\hat{\boldsymbol{x}}[k] = \hat{\boldsymbol{x}}^{-}[k] + \boldsymbol{K}[k](\boldsymbol{y}[k] - \hat{\boldsymbol{y}}[k]) \tag{3.31}$$

$$\boldsymbol{P}[k] = (\boldsymbol{I}_n - \boldsymbol{K}[k]\boldsymbol{C}[k])\boldsymbol{P}^{-}[k](\boldsymbol{I}_n - \boldsymbol{K}[k]\boldsymbol{C}[k])^{T} + \boldsymbol{K}[k]\boldsymbol{R}[k]\boldsymbol{K}[k]^{T} \tag{3.32}$$

The KF then performs the prediction and update step in a recursive manner. This is visualized in figure 3.9.

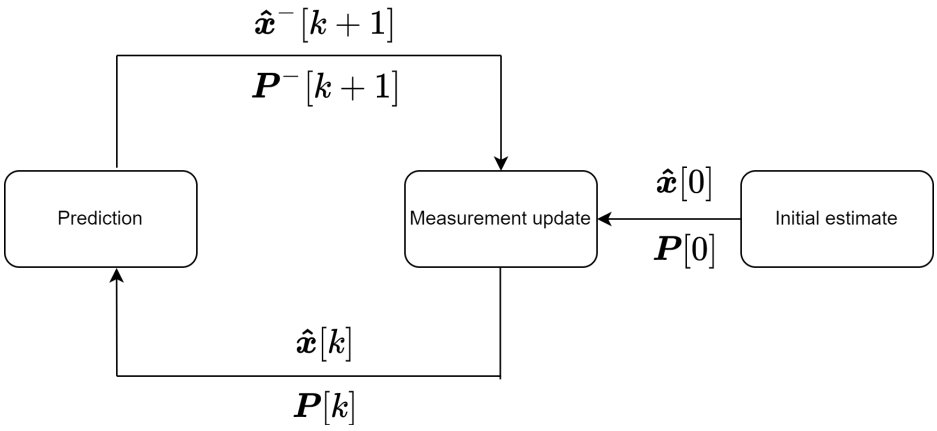

Figure 3.9: The recursive manner of which the standard Kalman filter operates.

Since the Kalman filter is a Bayesian estimation technique, it might better be understood by looking at it from the Bayesian perspective on conditional probability distributions. Essentially the KF maintains an estimate of the first and second moment of a probability density function conditional on the earlier information about the state distribution. Namely the mean and covariance. If the assumption about the noise affecting the system being Gaussian distributed holds, then the a posterior estimate of the state vector is distributed according to the conditional probability density function displayed in equation 3.33. The KF can then be understood

as propagating the mean and covariance of a Gaussian probability distribution that is conditional on all the previous knowledge about the state.[33]

$$p(\boldsymbol{x}[k] \mid y[k]) \sim \mathcal{N}(\hat{\boldsymbol{x}}[k], \boldsymbol{P}[k]) \tag{3.33}$$

3.4.1 The Extended Kalman Filter

In practice the assumption of a linear system- and measurement model may not hold. There are some systems where a linear approximation may be suitable, but if the system displays highly nonlinear behavior this is not a feasible solution.[23, Ch.3] A discrete nonlinear system- and measurement model affected by zero mean Gaussian white noise can be written as in 3.34 and 3.35.

$$\boldsymbol{x}[k+1] = f(\boldsymbol{x}[k], \boldsymbol{u}[k]) + \boldsymbol{v}[k] \tag{3.34}$$

$$\boldsymbol{y}[k] = h(\boldsymbol{x}[k]) + \boldsymbol{w}[k] \tag{3.35}$$

When the system- or measurement model is nonlinear a solution is to use the Extended Kalman Filter(EKF). It uses Taylor series expansion to linearize the nonlinear functions about the most recent estimate for the prediction step, and the most recent prediction in the update state. The linerization yields the jacobian matrices in equation 3.36 and 3.37.[33, Ch.2]

$$\boldsymbol{A}[k] = \frac{\partial \boldsymbol{f}}{\partial \boldsymbol{x}}\Big|_{\substack{\hat{\boldsymbol{x}}[k-1], \\ \boldsymbol{u}[k-1]}} \tag{3.36}$$

$$\boldsymbol{C}[k] = \frac{\partial \boldsymbol{h}}{\partial \boldsymbol{x}}\Big|_{\hat{\boldsymbol{x}}^-[k]} \tag{3.37}$$

This linearization is performed at each time step. With the obtained jacobians, the EKF algorithm is similar to that of standard KF. Where the prediction step was presented in equation 3.27 and 3.28 and the update step was presented by equation 3.29-3.32. The only difference is the fact that the predicted state, $\hat{\boldsymbol{x}}^-$, and measurement, $\hat{\boldsymbol{y}}$, is calculated using the nonlinear system- and measurement models. Since the noise terms $\boldsymbol{v}$ and $\boldsymbol{w}$ are unknown in practice, they are set to zero when the prediction is performed.[33, Ch.2]

A drawback to the EKF is that by linearizing the models, the filter loses it's ability to provide theoretically optimal estimates. Another potential problem caused by the linearization is diver-

gence. If the initial state- and covariance estimate are far away from the ground truth, the EKF may start to move away from the true solution. It is therefore critical to initialize the EKF with accurate estimates. Even though these problems may cause trouble in some instances, proper initialization results in excellent performance by the EKF. It is therefore a estimation algorithm used in many navigation systems.[22, Ch.13.4.2]

3.4.2 The Multiplicative Extended Kalman Filter

As mentioned in the introduction, this thesis builds upon the navigation system presented in [24, Ch.14] by Gryte. The INS uses a Multiplicative Extended Kalman Filter(MEKF) to correct the drifting nominal state estimates provided by integration of the strapdown navigation equations. Therefore a thorough understanding of the estimation algorithm is considered crucial. The explanation provided in this subchapter is largely a based on [21, Ch.10] by Brekke, [34, Ch.5-7] by Sola and [24, Ch.14.3.4] by Gryte. For a more in depth explanation, the readers are referred to the mentioned references. Especially [34] by Sola, which goes into great detail on the error-state Kalman filter(ESKF).

The MEKF differs from a regular EKF in two main ways. First of all the filter is formulated as an ESKF. Equation 3.38 describes the relationship between the nominal state
$\boldsymbol{x}^e_{eb,nom} = [\boldsymbol{p}^e_{eb,nom}, \boldsymbol{v}^e_{eb,nom}, \boldsymbol{q}^e_{eb,nom}, \boldsymbol{b}^b_{acc,nom}, \boldsymbol{b}^b_{ars,nom}]^T$,
error-state, $\delta\boldsymbol{x} = [\delta\boldsymbol{p}, \delta\boldsymbol{v}, \delta\boldsymbol{a}, \delta\boldsymbol{b}_{acc}, \delta\boldsymbol{b}_{ars}]^T$, and true state, $\boldsymbol{x} = [\boldsymbol{p}^e_{eb}, \boldsymbol{v}^e_{eb}, \boldsymbol{q}^e_{eb}, \boldsymbol{b}^b_{acc}, \boldsymbol{b}^b_{ars}]^T$. The $\bigoplus$-operator represents + for all states except for the attitude, for which the quaternion product, $\bigotimes$, is used. By providing corrections when an aiding measurement is available, the MEKF steers the drifting nominal state towards the true state. Figure 3.10 gives an overview of the MEKF algorithm.

$$\boldsymbol{x}^e_{eb} = \boldsymbol{x}^e_{eb,nom} \oplus \delta\boldsymbol{x} \tag{3.38}$$

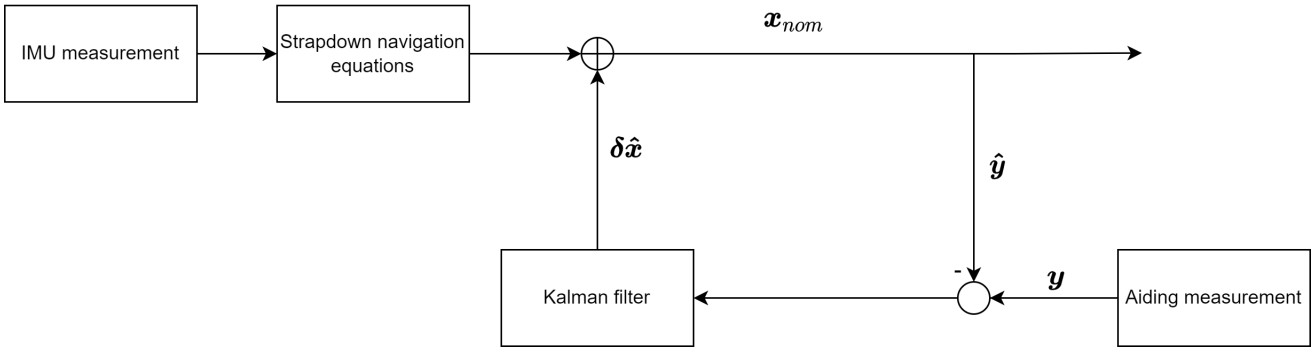

Figure 3.10: Simple figure displaying the workings of the MEKF. It shows how the error-state estimate is injected into the nominal state to obtain an estimate of the true state. Based on a figure in [22, p.477] by Fossen.

From this the second main difference is also brought forward. It is the fact that the true attitude state, $\boldsymbol{q}$, is parameterized by the unit quaternion, while the attitude error ,$\delta\boldsymbol{a}$, uses a 3-dimentional representation, called Modified Rodriguez parameters(MRP) scaled by a factor of 4. This is because of the covariance matrix describing the uncertainty in the attitude error could become rank deficient as a result of the unit quaternion constraint.[21, Ch.10.3] Using MRP means that the error-state $\delta\boldsymbol{x} \in \mathbb{R}^{15}$, while the nominal state $\boldsymbol{x}^e_{eb,nom} \in \mathbb{R}^{16}$. The Modified Rodriguez representation is valid for errors which limited to $\pm 180^o$, which corresponds to $||\delta\boldsymbol{a}|| > 4$.[24, p.149] Equation 3.39 and 3.40 shows how the transformation from quaternion to 4 times MRP is performed both ways.[22, p.480-481]

$$\delta\boldsymbol{a}(\delta\boldsymbol{q}) = 4\frac{\delta\boldsymbol{\epsilon}}{1+\delta\eta} \tag{3.39}$$

$$\delta\boldsymbol{q}(\delta\boldsymbol{a}) = \frac{1}{16+\delta\boldsymbol{a}^T\delta\boldsymbol{a}}\begin{bmatrix}16-\delta\boldsymbol{a}^T\delta\boldsymbol{a}\\ 8\delta\boldsymbol{a}\end{bmatrix} \tag{3.40}$$

As explained in chapter 3.3.1, the nominal state is updated by integrating the strapdown equations using a numerical integration technique such as Runge Kutta method of a specific order. With the frequency of which the IMU measurements arrive, the strapdown equations propagate the nominal state. The error state covariance matrix, $\boldsymbol{P}^-[k]$, is also propagated at the same rate. In order to propagate the covariance, the kinematic equations for the error-state are needed. These can be obtained by rearranging equation 3.38. These equations have previously been derived and presented in [24, Ch.14] by Gryte, and the reader is referred to this source for a thorough derivation. The error-state kinematic equations must be linearized as in the standard EKF, and is formulated as a linear time-variant system on the form showed in equation 3.41, where

$\boldsymbol{w} = [\epsilon_{acc}, \epsilon_{ars}, \epsilon_{b_{acc}}, \epsilon_{b_{ars}}]^T$. The values in matrices $\boldsymbol{F}$ and $\boldsymbol{D}$ are given in appendix B.

$$\delta\dot{\boldsymbol{x}} = \boldsymbol{F}(t)\delta\boldsymbol{x} + \boldsymbol{D}(t)\boldsymbol{w} \tag{3.41}$$

The a priori error-state covariance is obtained as in the standard KF, reiterated in equation 3.42. Where the matrix $\boldsymbol{A}$ and $\boldsymbol{Q}$ are the discretized system matrix and process noise covariance matrix respectively. As mentioned earlier, discretized system matrix is also known as the state transistion matrix. It is obtained through a first order taylor approximation of the state transistion matrix, $e^{\boldsymbol{F}T_s}$. Where T_s is the period between two the IMU measurements.

$$\boldsymbol{P}^-[k+1] = \boldsymbol{A}[k]\boldsymbol{P}^+[k]\boldsymbol{A}[k]^T + \boldsymbol{Q}[k] \tag{3.42}$$

The process of integrating the strapdown navigation equations and predicting the process covariance noise is repeated for each IMU measurement until an aiding measurement is available. This means that in the timesteps with no aiding measurement the a posteriori covariance is the same as the a priori , $\boldsymbol{P}^+[k] = \boldsymbol{P}^-[k]$. In this thesis the aiding measurement is a 3-dimentional position provided by PARS. The PARS measurement is rotated from the {r}-frame to the {e}-frame before it is used in the MEKF. This yields the measurement matrix $\boldsymbol{C} = \begin{bmatrix} \boldsymbol{I}_3 & \boldsymbol{0}_{3x12} \end{bmatrix}$, while the predicted measurement is equal to the nominal state as in equation 3.43. The measurement noise covariance $\boldsymbol{R}$ is the same as $\boldsymbol{R}_{PARS}$ which was presented in chapter 3.1.

$$\hat{\boldsymbol{y}}[k] = \boldsymbol{x}^e_{eb,nom}[k] \tag{3.43}$$

The error state, $\delta\boldsymbol{x}$ has not yet been estimated and remains zero until this point. Once the aiding measurement arrives, the Kalman gain, $\boldsymbol{K}$, is calculated as in equation 3.44, where $\boldsymbol{R}$ is the measurement covariance matrix. The Kalman gain is used to estimate error state, $\delta\hat{\boldsymbol{x}}$, and its corresponding posterior covariance matrix, $\boldsymbol{P}^+$, with equation 3.45 and 3.46 respectively. Equation 3.46 uses the Joseph form for better numerical stability.[34, p.63]

$$\boldsymbol{K}[k] = \boldsymbol{P}^-[k]\boldsymbol{C}[k]^T(\boldsymbol{C}[k]\boldsymbol{P}^-[k]\boldsymbol{C}[k]^T + \boldsymbol{R}[k])^{-1} \tag{3.44}$$

$$\delta\hat{\boldsymbol{x}}[k] = \boldsymbol{K}[k](\boldsymbol{y}[k] - \hat{\boldsymbol{y}}[k]) \tag{3.45}$$

$$\boldsymbol{P}^+[k] = (\boldsymbol{I}_{15} - \boldsymbol{K}[k]\boldsymbol{C}[k])\boldsymbol{P}^-[k](\boldsymbol{I}_{15} - \boldsymbol{K}[k]\boldsymbol{C}[k])^T + \boldsymbol{K}[k]\boldsymbol{R}[k]\boldsymbol{K}[k]^T \tag{3.46}$$

Equation 3.44-3.46 is often called the update step. After this step, the error state estimate $\delta\boldsymbol{x}$ is injected into the nominal state $\boldsymbol{x}^e_{eb,nom}$ as in equation 3.47-3.51. For the attitude injection term,

equation 3.40 is used to convert the 4 times MRP of the attitude error into the error quaternion $\delta \boldsymbol{q}$.

$$\boldsymbol{p}^{e}_{eb,nom}[k] = \boldsymbol{p}^{e}_{eb,nom}[k] + \delta\hat{\boldsymbol{p}}[k] \tag{3.47}$$

$$\boldsymbol{v}^{e}_{eb,nom}[k] = \boldsymbol{v}^{e}_{eb,nom}[k] + \delta\hat{\boldsymbol{v}}[k] \tag{3.48}$$

$$\boldsymbol{q}^{e}_{eb,nom}[k] = \boldsymbol{q}^{e}_{eb,nom}[k] \otimes \delta\boldsymbol{q}(\delta\boldsymbol{a}[k]) \tag{3.49}$$

$$\boldsymbol{b}^{b}_{acc,nom}[k] = \boldsymbol{b}^{b}_{acc,nom}[k] + \delta\hat{\boldsymbol{p}}_{ars}[m] \tag{3.50}$$

$$\boldsymbol{b}^{b}_{ars,nom}[k] = \boldsymbol{b}^{b}_{ars,nom}[k] + \delta\hat{\boldsymbol{b}}_{ars}[k] \tag{3.51}$$

After the injection of $\delta\boldsymbol{x}$ into $\boldsymbol{x}^{e}_{eb,nom}$, the error state reset to zero as in equation 3.53. Sola [34, p.65] shows that for obtain precise result, the error-state covariance must be updated as shown in equation 3.54. Where $\boldsymbol{G}$ is defined in equation 3.52.

$$\boldsymbol{G} = \begin{bmatrix} \boldsymbol{I}_6 & \boldsymbol{0}_{6x3} & \boldsymbol{0}_{6x6} \\ \boldsymbol{0}_{3x6} & \delta q_w \boldsymbol{I}_3 - \boldsymbol{S}(\delta\boldsymbol{q}_v) & \boldsymbol{0}_{3x6} \\ \boldsymbol{0}_{6x6} & \boldsymbol{0}_{6x3} & \boldsymbol{I}_6 \end{bmatrix} \tag{3.52}$$

This is done because the nominal attitude state $\delta\boldsymbol{q}$ was changed in the injection step. Hence the error-state covariance for $\delta\boldsymbol{a}$ must also be updated.

$$\delta\hat{\boldsymbol{x}} = \boldsymbol{0}_{15x1} \tag{3.53}$$

$$\boldsymbol{P}^{+}[k] = \boldsymbol{G}\boldsymbol{P}^{+}[k]\boldsymbol{G} \tag{3.54}$$

3.5 Single target tracking

The problem of tracking one or several targets such as planes or ships basically means to estimate the state of each object respectively using measurements from some remote sensing device.[35] The states may include information about the position and velocity of the objects. Tracking is used in several applications within both civilian and military fields. For example in surveillance of airspace in air traffic control or border patrol. An example of this is the ASDE-X radar system[36] which has been used on several airports around the world for tracking airplanes.[35, p.97] The sensors used in tracking system vary, but a common tracking scenario is one where a radar is used for remote sensing of some object[21, Ch.7.1]. A radar system works by transmitting a pulse of a RF signal from an antenna array which hits the target, bounces off it and returns to the receiver antenna. From the received signal the 3D spherical position of the target can be obtained in a signal processor. Keep in mind that this is a simplification of how a radar works in practice.[37, Ch.1] Other sensors such as cameras can also be used for vision based object tracking.[38]

Ideally the radar would only detected the targets of interest, but in practice the sensor might deliver several noisy measurements that doesn't originate from the target. These detections are called clutter measurements, or false alarms. The reason for why clutter measurements are detected is often that the received signal has a low SNR. This causes the need for a lowered detection threshold. Thereby allowing reflections off surrounding targets or infrastructure to be interpreted as other measurements.[35] Clutter measurements can therefore be defined as unwanted measurements.

In the case were only one measurement is obtained from the sensor and it in fact is a measurement of the target position, then a regular estimation algorithm such as the KF could be utilized with this measurement to estimate the position of the target. However, with clutter measurements, the problem becomes more difficult. As using the wrong measurement may lead to divergence of the target state. Tracking can therefore be seen as a special case of standard filtering, where the uncertainty of which measurement originates from what target must be considered at each time step.[35] In this thesis however, it is known that there only exists one target, hence the algorithms that is to be discussed are single target tracking algorithms.

In this thesis, the aiding measurements is obtained from a PARS system. The receiving ground antenna uses a combination of DoA- and RTT estimation to obtain a spherical 3D position mea-

surement of the UAV in the {r}-frame. The DoA algorithm delivers an estimated pseudospectrum with several peaks. Each peak describes the azimuth- and elevation angles of arrived signals. One of these peaks originate from the true target, while others is a result of multipath propagation.

3.5.1 Validation of measurements

The first step of many single target tracking algorithms such as the Nearest Neighbour(NN)- and Probabilistic Data Association (PDA) filter[35], is to pass the available measurements through a validation gate. Whether or not a measurement falls inside the validation gate at a given time step k, is decided by equation 3.55. The difference between the predicted measurement and the received measurement, $\boldsymbol{y}[k] - \hat{\boldsymbol{y}}[k]$, is known as the innovation. Where $\mathbb{S}[k] = \boldsymbol{C}[k]\boldsymbol{P}^{-}[k]\boldsymbol{C}[k]^T + \boldsymbol{R}[k]$ is the covariance of the innovation. Both are used in the KF algorithm, but the innovation covariance has so far in chapter 3 been represented with the equation rather than $\mathbb{S}$. γ is the gate threshold. The equation defines what is called the normalized innovation squared(NIS). The average NIS over several time steps will be distributed according a χ^2 distribution.[21, Ch.4.6.1] It is therefore possible to specify a gate threshold $\gamma = \chi^2_{p,n_y}$ which corresponds to a confidence interval of $1-p$ of the measurement being an inlier.

$$(\boldsymbol{y}[k] - \hat{\boldsymbol{y}}[k])^T \mathbb{S}[k]^{-1} (\boldsymbol{y}[k] - \hat{\boldsymbol{y}}[k]) \leq \gamma \tag{3.55}$$

The choice of the gate threshold also decides the probability of the measurement of the target being gated, $P_G = 1-p$. n_y is the dimension of the measurement, which is 3 in the case of a PARS measurement.[39, Ch.7.6.1] If the measurements exists within this region, it is deemed likely to have originated from the target and added to the set of gated measurements $\mathscr{Y}$. Measurements that does not pass through the validation gate are removed from the set of measurements and classified as clutter measurements. By utilizing the validation gate, unlikely measurements which are far away from the predicted measurement is removed and not considered further by the tracking algorithm. This essentially works the same way as an outlier rejection such as the one implemented in [24, p.148] by Gryte.
The volume of the 3 dimensional validation gate is described by equation 3.56.

$$V[k] = \frac{4\pi}{3} |\gamma \mathbb{S}|^{\frac{1}{2}} \tag{3.56}$$

Figure 3.11 displays a simple example of what a validation gate may look like for tracking algorithm that validates 2 dimensional position measurements.

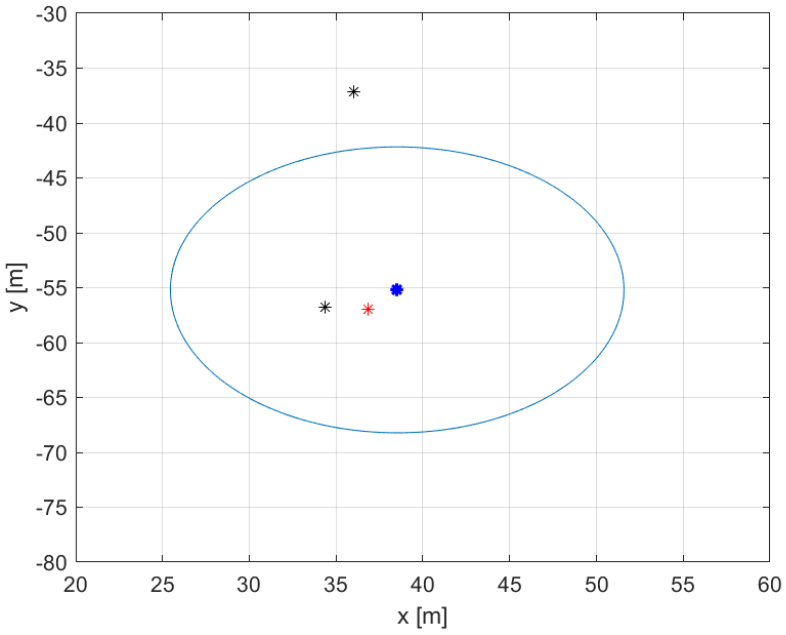

Figure 3.11: Example displaying a validation gate in 2 dimensions. The predicted measurement is the blue dot. While the red dot is the measurement that originates from the target. The black dots are clutter measurements.

3.5.2 Mathematical models in tracking

In a typical tracking scenario using a radar or camera, information about the targets control inputs and IMU measurements are usually unknown. However to yield predicted measurements for data association, tracking algorithms are in need of a motion model of the target. The most used target motion models in tracking literature are the constant velcity(CV), constant turn(CT) and constant acceleration(CA) models.[38] The names are self explanatory in that the models describe a target that is moving with constant velocity, a constant turn rate or constant acceleration respectively. These models are used in scenarios where the target to be tracked is expected to move with for instance constant velocity. This will result in somewhat accurate predictions of the target motion. If the target is a passenger airplane which is for instance is known to perform maneuvers which might be modeled by both the CV and CT model, the interacting multiple model algorithm is often used. It runs several estimation algorithms such as the KF in parallel and calculates which model is most correct and weights each model thereafter.[21, Ch.6] In this thesis however the INS provides a much more accurate motion model with the strapdown navigation equations in chapter 3.3.1. It is therefore not a typical tracking scenario, and the kinematic model provides a lot more information.

An important motivation for tracking algorithms is dealing with clutter measurements. A standard method for modeling the clutter measurements, especially in the case of multi-target tracking, is by the means of a Poisson distribution as in equation 3.57. The clutter model plays a key role when calculating the probability of each gated measurement originating from the target, known as association probabilities, $\boldsymbol{\beta}$. A Poisson distribution yields a feasible description of how many clutter measurements, z, that will appear inside the validation gate. With m gated measurement and one target, $z = m$, if the target is undetected and, $z = m - 1$, if the target is detected. In the equation z is the number of clutter measurements inside the volume of interest V, which is the validation region, with spatial density λ. The spatial density describes the number of clutter measurements per unit volume.[21, Ch.7.1]

$$p(z) = e^{-\lambda V} \frac{(\lambda V)^z}{z!} \tag{3.57}$$

A drawback of the Poisson model is the fact that it isn't trivial to find correct value of λ. Another clutter model known as the diffuse model is shown in equation 3.58, where δ is some arbitrary constant. It assumes that any number of clutter measurements is equally likely, meaning that it is uniform within the validation region. Note that with m validated measurements, there are only two possibilities for the number of clutter measurements. Either m, or $m-1$ if one of the measurements originates from the target.[35] The uniform is distribution is normalized so that it sums up to one.[40, Ch.3.4.3]

$$p(m) = p(m-1) = \delta \tag{3.58}$$

3.5.3 Nearest Neighbor Filter

The nearest neighbor(NN) filter is a widely used tracking filter due to its computational simplicity. It uses the measurement which is closest to the predicted measurement as if it was the target measurement. The distance measure used is the normalized innovation squared(NIS).[41] The NIS has been defined in equation 3.55.

The NN filter is essentially a KF which deals with clutter measurements by choosing the measurement that yields the smallest NIS in the KF update step. At each time step it chooses $\boldsymbol{y}^*[k]$ that is closest to the predicted measurement $\hat{\boldsymbol{y}}[k]$, and assumes it to be the target measurement. All other measurements are discarded.[41] The drawback of this approach is the fact that the NN measurement does not necessarily originate from the target at every time step. It might be a clutter measurement. The filter then uses the wrong measurement in the KF update, which may lead to divergence of the target state estimate. It is in a sense over confident when choosing only one measurement.[40, Ch.3] By choosing the wrong measurement, the innovation covariance $\mathbb{S}$ will be smaller than it should be due to measurement origin uncertainty, in the next time step.[35, p.94]

There also exists other versions of the NN filter. For instance the strongest neighbor filter which chooses the gated measurement with the largest signal strength as the target measurement. This is more often used in sonar tracking applications, while the NN filter that uses the NIS measure is more utilized in radar tracking.[40, Ch.3] The PARS system of concern in this thesis essentially uses the strongest NN algorithm when providing a single measurement. As it chooses the largest peak in the DoA pseudospectrum, corresponding to the direction of the strongest received signal.

Another version of the NN filter that includes the probability of the nearest gated measurement being clutter is called the probabilistic nearest neighbor filter. Instead of blindly choosing the nearest measurement to update the target state estimate, it approximates the posterior mean, $\hat{\boldsymbol{x}}$ and covariance $\boldsymbol{P}$ as a weighted sum of three different scenarios. These are that the nearest measurement originates from the target, that it is clutter, and that no measurement is gated.[42]

3.5.4 The Probabilistic Data Association Filter

The Probabilistic Data Association(PDA) filter is a Bayesian single target tracking algorithm that updates the state of the target with a weighted sum of the gated measurements at each time step. The weights are known as association probabilities, $\boldsymbol{\beta}$, which describe how probable it is that each measurement originates from the target. The underlying algorithm in the PDA filter is the standard KF or the EKF depending on whether the target dynamics and measurement model is linear or nonlinear respectively. The computational burden of the PDA filter is however approximately 50% higher because of the data association scheme.[35, p.89] After having calculated the probabilities of each gated measurement originating from the target, a KF update is performed with each of these respectively. The calculated updates are then weighted according to their association probability and used to obtain an a posteriori state estimate of the target.[35, p.87-91]. PDA filter can also be expanded to tracking multiple targets with the extension called the Joint Probabilistic Data Association Filter. This is beyond the scope of this thesis as it only considers one target. The reader is referred to [35, p.91-93] for a brief overview.

The PDA filter is based on several assumptions. First of all it assumes that only one target exists. The assumptions made about the target motion is similar to that of the standard KF or EKF. These are mentioned in chapter 3.4. The probability of the target being detected by the sensor used to perform the measurement, P_D, is usually in the range between $0.5-0.95$ depending on the application. 0.95 is typical for radar.[21, Ch.7.2] P_D will always be less than 1, even with a very high SNR, although it can be very close.[37, Ch.3.3.4] Of the $m[k]$ validated measurement, the discrete number of clutter measurements is distributed according to either a Possion- or diffuse distribution.[35]

As discussed in the introduction to chapter 3.5, tracking in general focuses on estimating the motion of vehicles by only using remote sensing devices such as radar in above water applications or sonar in underwater applications. The PDA filter is designed for this purpose and is therefore built upon the standard KF which estimates the targets state directly. This thesis focuses on handling measurement uncertainty in an INS with an MEKF that provides correction to the nominal state. Since the MEKF estimates $\delta\boldsymbol{x}$, the PDA filter algorithm is formulated with the MEKF as the underlying algorithm. This is different to how the PDA filter is usually presented in tracking literature such as [35] or [21, Ch.7].

The INS provides an estimate of the nominal state $\boldsymbol{x}^e_{eb,nom}[k]$. It takes the place of the predicted

measurement $\hat{\boldsymbol{y}}[k]$. When a spherical PARS position measurement arrives it is first mapped over to Cartesian coordinates in the {e}-frame. Then it is run through the validation gate displayed in equation 3.55. Due to the mapping of $\boldsymbol{R}$ in equation 3.7, the innovation covariance matrix $\boldsymbol{S}[k]$ will be different for each measurement. This also results in the Kalman gain being different for each gated measurements.

Depending on which clutter model is used for the number of clutter measurements, two slightly different versions of the calculating the association probabilities, $\boldsymbol{\beta}$, is obtained. Each association probability correspond to specific gated measurement in the set $\mathscr{Y}[k] = \{\boldsymbol{y}_1[k], ..., \boldsymbol{y}_m[k]\}$. If the Poisson version is used then the association probabilities will be calculated according to equation 3.59. If the diffuse version is used then equation 3.60 is utilized.[21, Ch.7.3] The index $i = 0$ is the probability that none of the gated measurement originate from the target. $\mathcal{N}(\boldsymbol{y}_i[k]; \hat{\boldsymbol{y}}[k], \mathbb{S}[k])$ is the distribution of the predicted measurement evaluated at $\boldsymbol{y}_i$. It returns the likelihood ratio of the measurement originating from that target rather than clutter. The likelihood ratio yields a measure of how well the gated measurements fit to the expected distribution of the measurements.[35] In both equations it should be noted that the proportional to sign, $\propto$, is used instead of the "equal to" sign. This is because the values for β are first obtained through either equation 3.59 or 3.60, before they are normalized so that sum of the association probabilities are equal to one, $\sum_{i=0}^{m[k]} \beta_i = 1$. The most widely used model in is the Poisson clutter model as it is used in a large number of research papers concerning multi-target tracking.[21, Ch.7.3.5] The diffuse model offers the advantage of not having to choose a value for the clutter intensity λ.

$$\beta_i[k] \propto \begin{cases} \lambda(1 - P_D P_G), & \text{if} i = 0 \\ P_D \mathcal{N}(\boldsymbol{y}_i; \hat{\boldsymbol{y}}[k], \mathbb{S}[k]), & \text{if} i > 0 \end{cases} \tag{3.59}$$

$$\beta_i[k] \propto \begin{cases} \frac{m[k](1-P_D P_G)}{V[k]}, & \text{if } i = 0 \\ P_D \mathcal{N}(\boldsymbol{y}_i[k]; \hat{\boldsymbol{y}}[k], \mathbb{S}[k]), & \text{if } i > 0 \end{cases} \tag{3.60}$$

As in the MEKF algorithm, equation 3.44-3.46 is then used to estimate the a posteriori error-state, $\delta\hat{\boldsymbol{x}}_i[k]$, and covariance, $\boldsymbol{P}_i^+[k]$, given each gated measurement in the set $\mathscr{Y}[k]$. These estimates are then merged together into a single Gaussian mixture. The mean of the Gaussian mixture[21, Ch.6.3] is calculated using equation 3.61. It should be noted that $i = 0$ is left out of this equation. If the underlying algorithm was a standard KF, β_0 would describes how much the prediction from the motion model should be weighted compared to the measurement updates.

As it is the probability that none of the gated measurements originate from the target. Since the MEKF estimates the error state, β_0 describes the probability of $\delta\boldsymbol{x} = 0$.

$$\delta\hat{\boldsymbol{x}}_{PDA}[k] = \sum_{i=1}^{m[k]} \beta_i \delta\hat{\boldsymbol{x}}_i \tag{3.61}$$

The covariance of the Gaussian mixture is obtained through equation 3.62. Where $\tilde{\boldsymbol{P}}$ is called the spread of the mean. It provides a measure of how much each individual mean differs from the Gaussian mixtures mean. It is given in equation 3.63.

$$\boldsymbol{P}_{PDA}[k] = \beta_0 \boldsymbol{P}^{-}[k] + \sum_{i=1}^{m[k]} \beta_i \boldsymbol{P}_i^{+}[k] + \tilde{\boldsymbol{P}}[k] \tag{3.62}$$

$$\tilde{\boldsymbol{P}}[k] = \sum_{i=0}^{m[k]} \beta_i \delta\hat{\boldsymbol{x}}_i \delta\hat{\boldsymbol{x}}_i^T - \delta\hat{\boldsymbol{x}}_{PDA}\delta\hat{\boldsymbol{x}}_{PDA}^T \tag{3.63}$$

$\tilde{\boldsymbol{P}}$ increases the covariance the state estimate since it is uncertain which of the gated measurements that actually originates from the target. This uncertainty should be reflected in the covariance of the estimate.[35] This concludes the introduction to the PDA filter. The next step in the navigation system would be the injection- and reset steps.

3.5.5 Multiple hypothesis tracking

Multiple hypothesis tracking algorithms(MHT) consider measurements from several time steps, which makes the current state estimate depend on the history of previous measurements. It considers tracks instead of measurements, where a track is defined as a sequence of measurements. This is different to the NN- and PDA filter which only uses the measurements in the current time step.

There exists different MHT algorithms. Mainly the track-oriented and hypothesis-oriented versions.[35, p.87] MHT algorithms quickly become very complex to implement, especially for the multi target case. However there exists single target versions of MHT.[21, Ch.9] Without going into the mathematics of the MHT, a basic overview for the single target case is briefly provided below.

A single target version of the track oriented-MHT algorithm is better known as the track split filter. Assuming that the target state is initialized, it constructs a track tree. A root node at time step 1 is built upon by $m[k]+1$ children nodes, for the consecutive time step. m is the number of gated measurements. Figure 3.12 displays an example of this where one measurement is

received at time $k = 1$. While time $k = 2$ yields 2 measurements. At time $k = 3$ only one measurement is gated. The crosses accounts for the target not being detected. With this logic a tree of several possible tracks are built.[21, Ch.9.2.1]

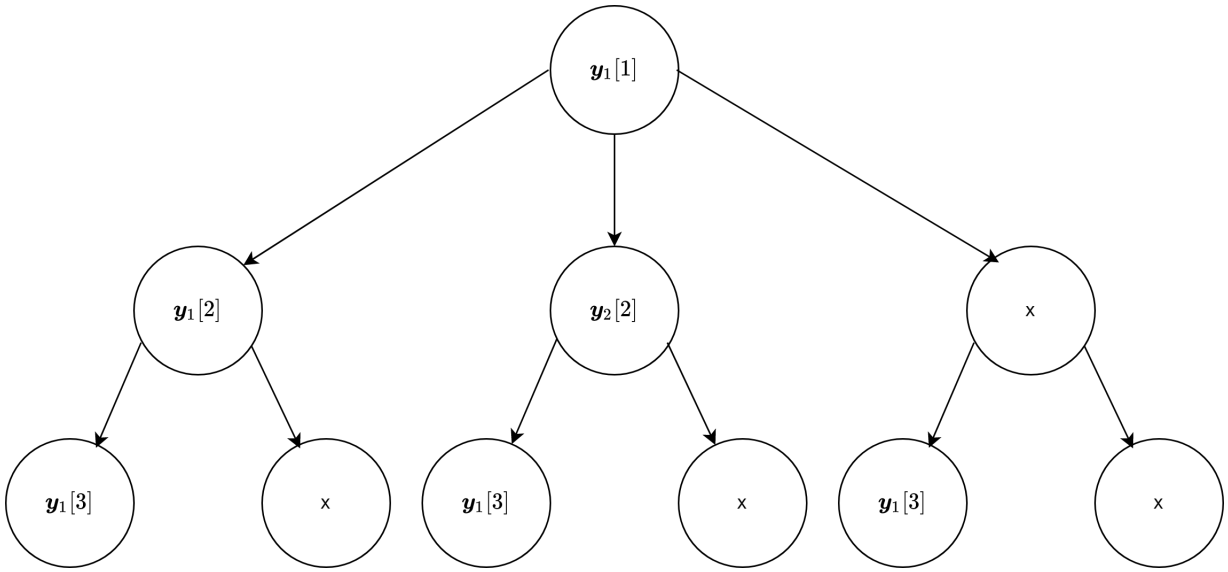

Figure 3.12: Example of a simple track tree. Based on figure in [21, Ch.9.1.1] by Brekke.

For each possible decent through the track tree, a weight is calculated based on how probable it is to be the correct track. A KF update is performed for each new measurement respectively, conditional on it's measurement history. The weighted sum of these estimates creates the estimated state of the target at time step k.[40, Ch.3.5.5] It is obvious that both the memory and computational requirements will increase as the track tree expands.[40, Ch.3.5.4] A common method for dealing with this is called N-scan pruning. It calculates a track score for each track which is based on the probabilities used in the weighted sum. It removes all tracks from the track tree except for the one with the highest track score, at N steps behind the current time step.[21, Ch.9.2.1]

Chapter 4

Implementation and dataset examination

This chapter explains the modifications that was implemented in the the navigation toolbox. The navigation toolbox is a generic MATLAB toolbox, developed at NTNU for easy protoyping, tuning and testing of navigation systems on prerecorded recorded datasets. Thereby allowing for offline testing of a proposed navigation systems before implementing and testing them in real time while performing flight experiments. It has a variety of state estimators such as the nonlinear observers presented in [11] and the MEKF presented in [12]. The Toolbox also has an implemented plotter class which makes it simple to convert the test results into intuitive plots which can be used in papers and reports.

In this thesis the the files related to the MEKF in the {e}-frame was modified to include the NN and PDA algorithm for spherical PARS measurements. Testing these algorithms should yield a good idea of how tracking effects the overall performance of the navigation system in a multi-path scenario. A description of the implementation and datasets are given in the below sub-chapters.

The recorded data was obtained by Okuhara et.al. in [18] with a fixed-wing UAV, Skywalker X8. The UAV uses a Pixhawk autopilot which runs Arduplane flight control software. The Pixhawk setup comes with a GNSS receiver, an IMU, a 3-axis digital compass and a barometer. An additional tactical grade IMU and GNSS receiver was also added to the sensor setup to provide a ground truth to compare with the estimated states. More information of the sensor- and system setup can be found in [18].

4.1 Implementation in Matlab Toolbox

The MEKF based PDA- and NN algorithm are implemented in the toolbox. A flowchart describing how the flow of the toolbox works is shown in figure 4.1. From one time step to the next, the INS is propagated by integrating the strapdown navigation equations accompanied by the covariance matrix. Depending on whether the UAV has started flying or is sitting still in the launch ramp, different choices are made. The toolbox has a pre-launch calibration step in which the knowledge of the UAVs linear and angular velocity being zero is used in the MEKF. A deeper explanations on the calibration is provided in [24, Ch.14.3.2.3]. The pre-launch calibration is used to make the accelerometer- and gyroscope biases converge quicker.

When a PARS position measurements arrives, the measurements runs thorough either NN- or PDA algorithms with MEKF as the underlying filter. Which algorithm that is used is chosen by the user. The MEKF, NN and PDA has been explained thoroughly in chapter 3.4.2, 3.5.3 and 3.5.4 respectively.

The MEKF in the MATLAB toolbox was already tuned for the purpose of PARS aided navigation. The tuning was similar to that of [24, p.172] by Gryte. With the tuning of the initial values and covariance matrices given in appendix B. The threshold for the validation gate γ is set to $\chi^2_{p=0.01,n_y=3} = 11.35$. This corresponds to 99% confidence interval of the measurement being an inlier, which results in $P_G = 0.99$. Note that a validation gate is also active in the standard MEKF. This means that when the measurement produced by the largest peak in the pseudospectrum is an outlier, the standard MEKF rejects it and doesn't use it to update the state estimate.

Information on how to get access to the implemented code and navigation toolbox is given in appendix A.

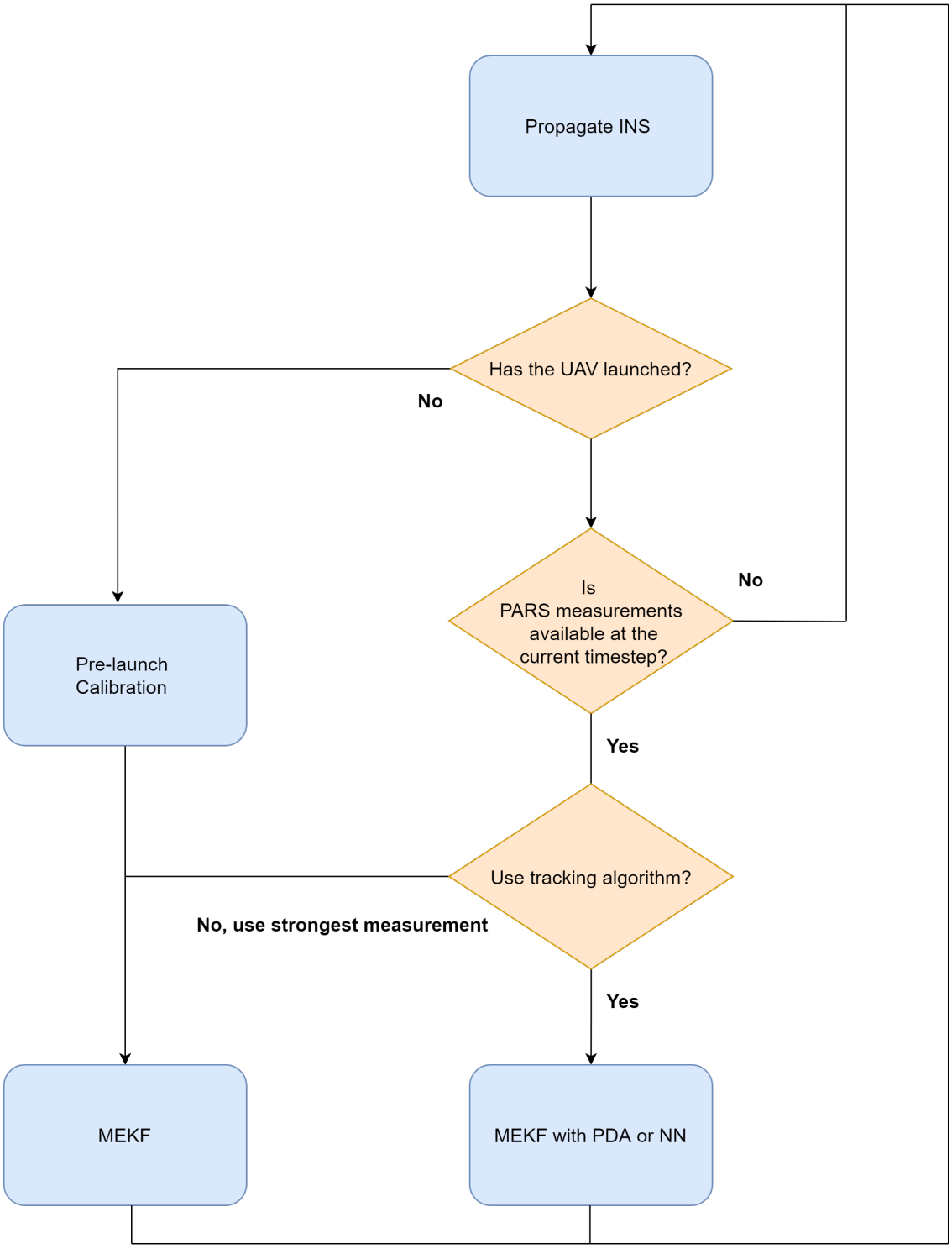

Figure 4.1: Float diagram describing the MATLAB toolbox.

4.2 The Agdenes dataset

The data used in this thesis was recorded at Agdenes, Norway by Okuhara et.al. in [18]. The raw data from the 4 largest peaks in the DoA pseudospectrum obtained from the PARS, with their respective azimuth and elevation angle, is displayed in figure 4.2 and 4.3. The range measurement is displayed in figure 4.4 Because the UAV sometimes flies outside the viewing frustum of PARS ground antenna, it saturates. This is especially visible in the interval between 400s and 500s in azimuth measurements in figure 4.2. This is when the UAV has just launched and is outside the viewing frustum often. When utilizing the data in the MATLAB toolbox, RTK-GNSS calculated elevation angles were used when UAV was outside the viewing frustum of the PARS ground antenna. This was done to avoid large intervals of dead reckoning.

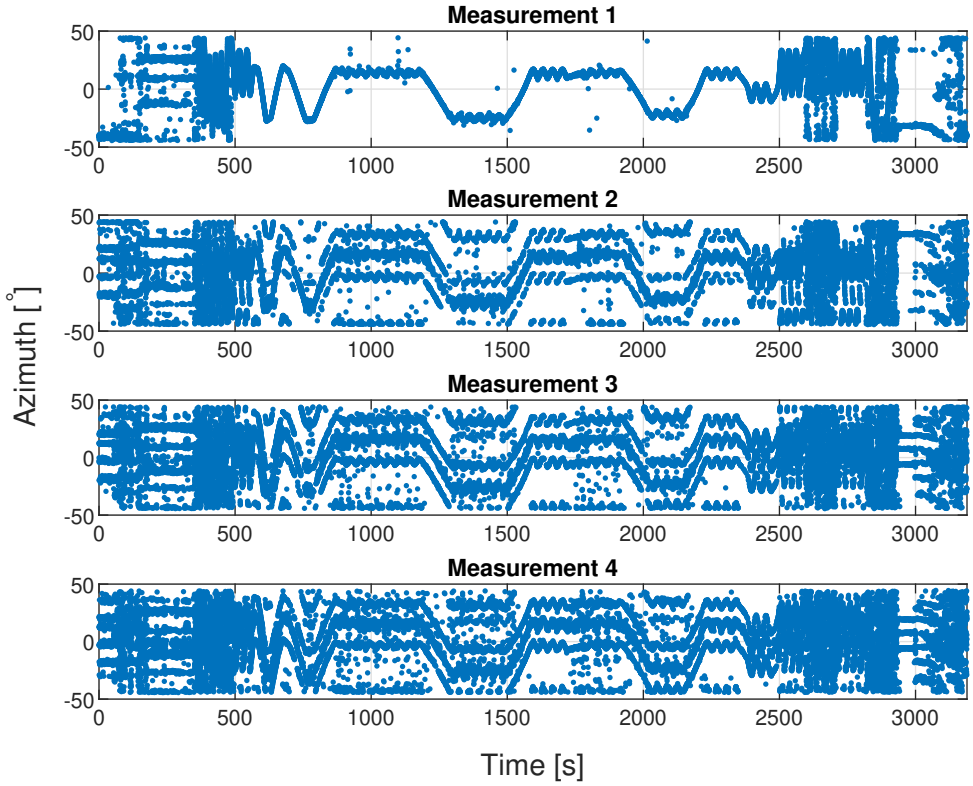

Figure 4.2: The azimuth angles of the 4 largest peaks in the DoA pseudospectrum. Measurement 1 corresponds to azimuth angle of the largest peak. Measurement 4 to the azimuth angle of the 4th largest.

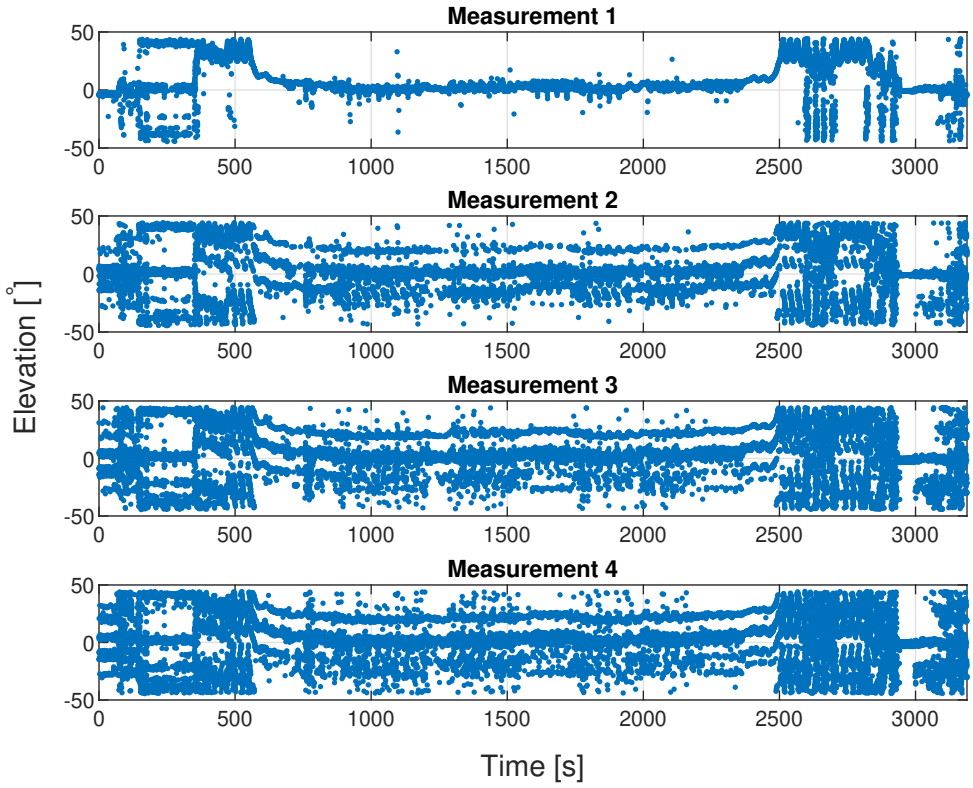

Figure 4.3: The elevation angles of the 4 largest peaks in the DoA pseudospectrum. Measurement 1 corresponds to elevation angle of the largest peak. Measurement 4 to the elevation angle of 4th largest.

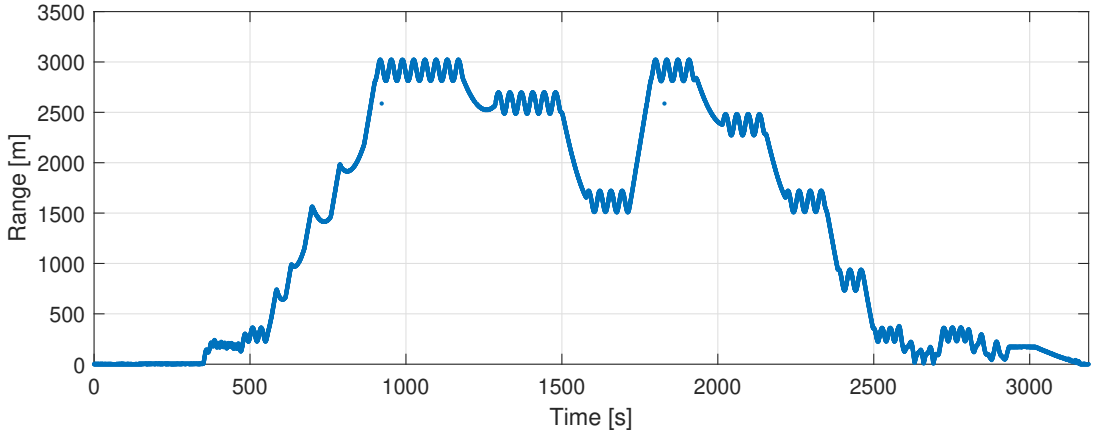

Figure 4.4: Range measurement in the Agdenes dataset.

Measurement 2-4 all displayed frequent jumps between different azimuth and elevation angles. It seems like the jumps happen as often as from timestep to timestep. Measurement 2-4 are also visually very similar, although it is hard to make a distinctions when the measurements are noisy. The middle line visible in measurement 2-4 is also very similar to the azimuth and elevation angle of measurement 1. This might be because the largest peak in the pseudospectrum has several smaller peaks which are close to each other.

All 4 measurements are used in the implemented single target tracking algorithms in the MATLAB toolbox.

4.3 Synthetic dataset

During the work with this thesis it became apparent that multipath interference was affecting the direct signal between the UAV and the PARS ground antenna more than initially expected. Oscillations in the elevation angle measurement were observed, which degraded the accuracy of the measurement more the further away from the ground station the UAV was. This exact problem was observed in chapter 3.2. The Agdenes dataset[18] did not display consistant intervals of PARS choosing the wrong azimuth and elevation angle. This means that a multipath signal most likely did not yield the largest peak in the DoA pseudospectrum in this dataset. This was however observed in online flight experiments performed in for example [13].

A dataset recorded by Gryte et.al [13] in 2019 at Raudstein, Norway, did display cases of the PARS choosing the reflected signal from the ocean surface rather than the direct signal from the UAV. However, this dataset has only been used in closed-loop flight, and the accompanying IMU data was not available to be used in offline testing. This motivated the creation of synthetic dataset that could mimic the effects observed in the Raudstein dataset.

Based on the pseudospectrum provided by the PARS at each received DoA measurement, the azimuth and elevation angles corresponding to the 4 largest peaks were extracted. The extraction was performed using the MATLAB function ***findpeaks***[43] along each of the rows and columns in the pseudospectrum. The 1D peaks were than matched to find their 2D positions. The pseudospectrum had a resolution of $50x50$. This results in a resolution of 1.83^o for each pixel. Figure 4.6 and 4.5 displays a $1200s$ interval of the raw azimuth- and elevation measurements respectively. The figures display that especially for the 3rd and 4th largest DoA measurement, the po-

sition changes a lot which makes it very noisy compared to the largest and second largest peak.

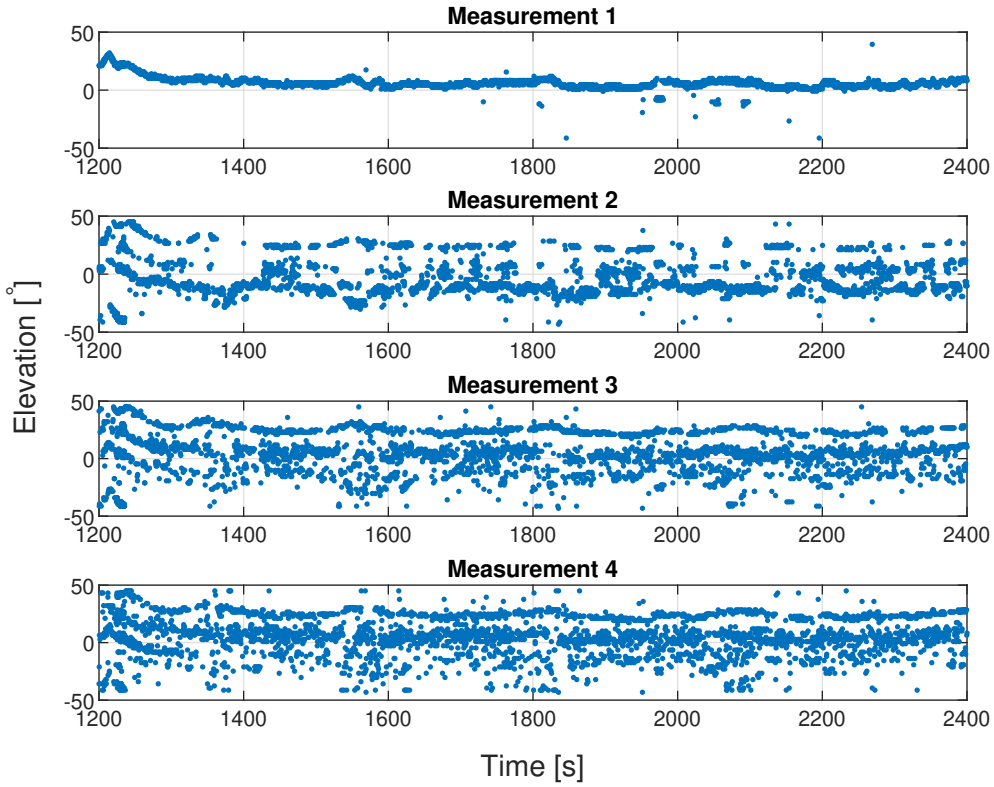

Figure 4.5: The elevation angles corresponding to 4 largest peaks in the pseudospectrum produced by the PARS. Measurement 1 corresponds to the elevation angle of the largest peak, and measurement 4 to the elevation angle of the 4th largest peak.

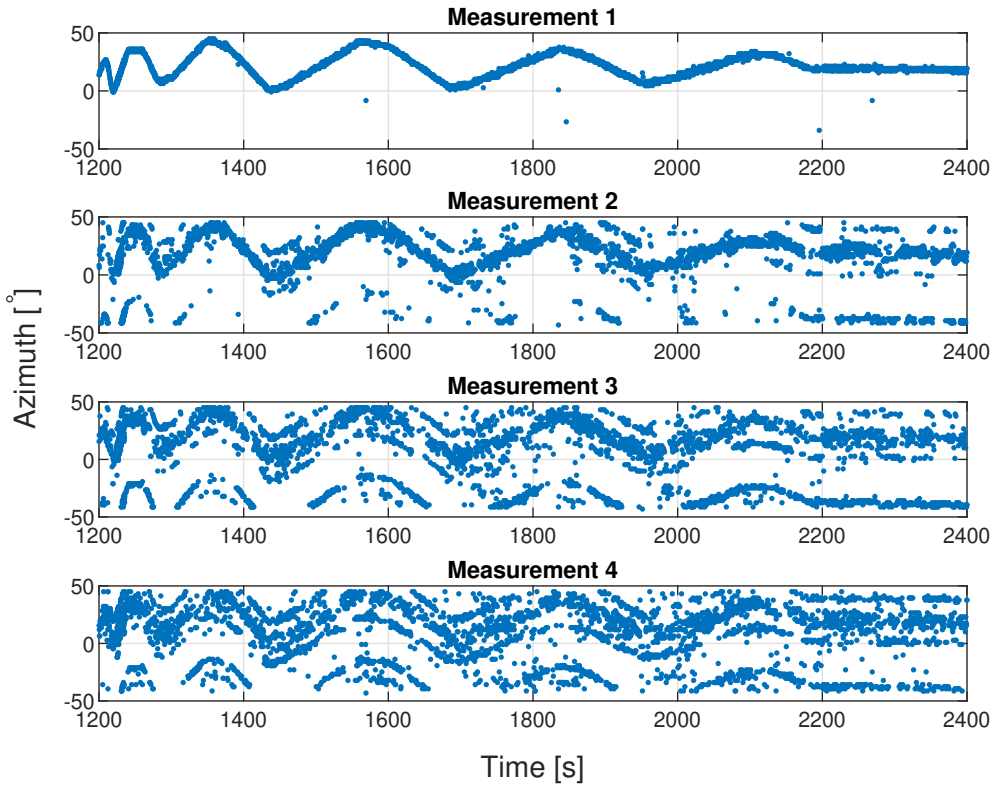

Figure 4.6: The azimuth angles corresponding to 4 largest peaks in the pseudospectrum produced by the PARS. Measurement 1 corresponds to the azimuth angle of the largest peak and measurement 4 to the azimuth angle 4th largest peak.

From figure 4.6 it becomes clear that the azimuth angle of the first and second measurement are very similar, with the exception of some outliers in the second measurement. This is due to other peaks that correspond to different DoA angles in the pseudospectrum becomes bigger in some time steps. Zooming into a closer look in the interval from $1950s - 2050s$ in the raw measurements, and plotting the measurements as curves rather than individual points reveals a $10s$ interval of the largest peak in the pseudospectrum corresponding to the wrong elevation angle. This is shown in figure 4.7 in the time interval from $1970s - 1980s$, where the elevation angle of measurement 1 jumps from about 8^o to -8^o. This is an example of the PARS choosing a reflected signal rather than the direct signal from the UAV. It also displays that the azimuth angle for the two measurements are similar in the same time interval.

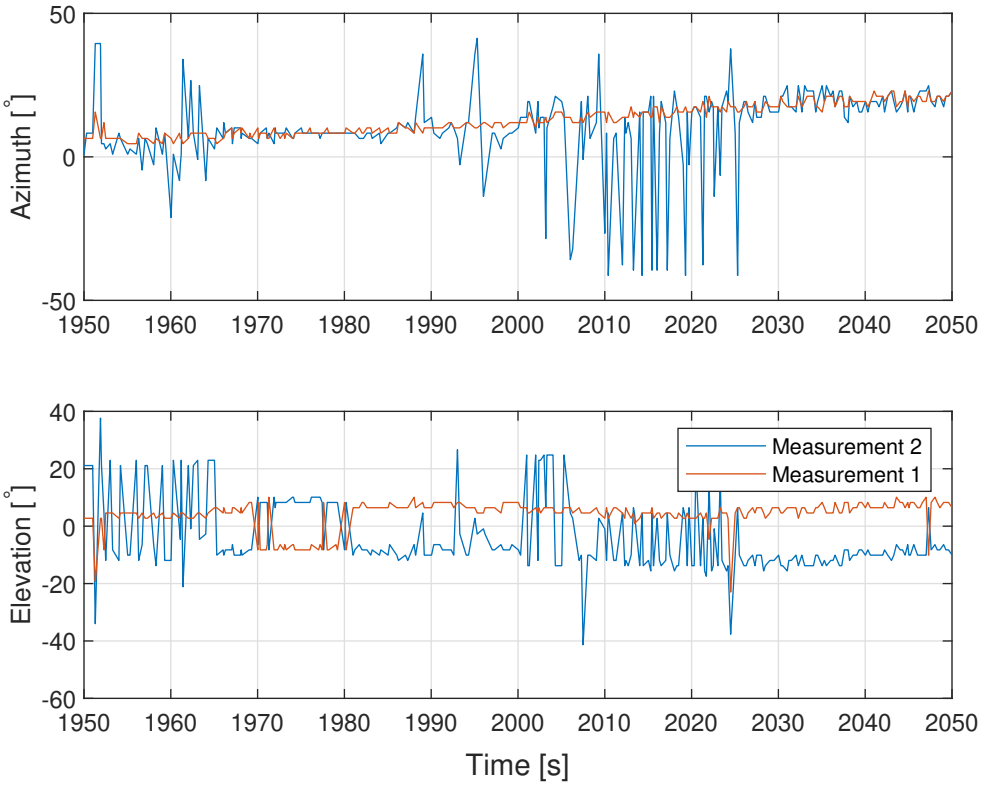

Figure 4.7: Interval in the Raudstein dataset where the elevation angle corresponding to the largest peak in the DoA pseudospectrum jumps for a time intervall of $10s$.

Looking at the pseudospectrum in the same time interval it becomes clear that the reflected signal, which has a negative elevation angle, has become stronger than the direct signal, which is the reason for why the PARS chooses this measurement. The pseudospectrum is shown in figure 4.8.

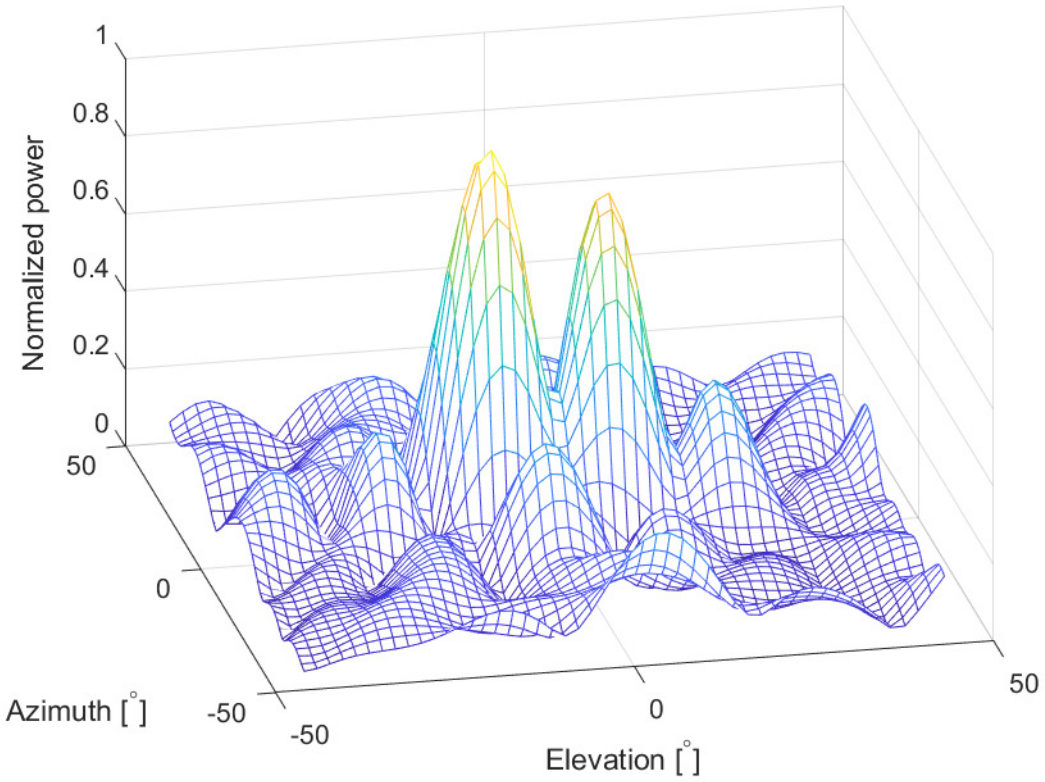

Figure 4.8: Pseudospectrum produced by the PARS ground antenna when the reflected signal becomes stronger than the direct signal.

The synthetic dataset was chosen to include 3 measurement of virtual peaks. All with the same azimuth angle, which is the same as the azimuth angle corresponding to measurement 1 in the Agdenes dataset. Due to the similarity in the 2 largest peaks in measurement 1 and 2 in the Raudstein dataset, it was considered reasonable that all the measurements in the synthetic dataset would have the same azimuth angle. The range measurement was also provided by the Agdenes dataset. As for the elevation angles, measurement 1 containted the correct RTK-GNSS calculated elevation angle, while measurement 2 and 3 contained the same elevation angle with an offset of $-5°$ and $-15°$ respectively. The Raudstein dataset displayed jumps in the magnitude of up to $16°$, which makes the choice for measurement 3 reasonable. The offset of measurement 2 was chosen to see how the tracking algorithms would handle smaller jumps. Thereafter white Gaussian noise with variance $\sigma^2 \approx 0.27°$ was then added to each of the 3 synthetic elevation measurements. The variance of the measurement noise affecting the elevation angle was obtained from calculating the variance of the first 340 elevation angle measurements in the Agdenes dataset, when the UAV was known to be at rest. Three arbitrary intervals were chosen where the correct elevation angle jumped between the 3 measurements. The resulting 3 eleva-

tion angles are shown in figure 4.9.

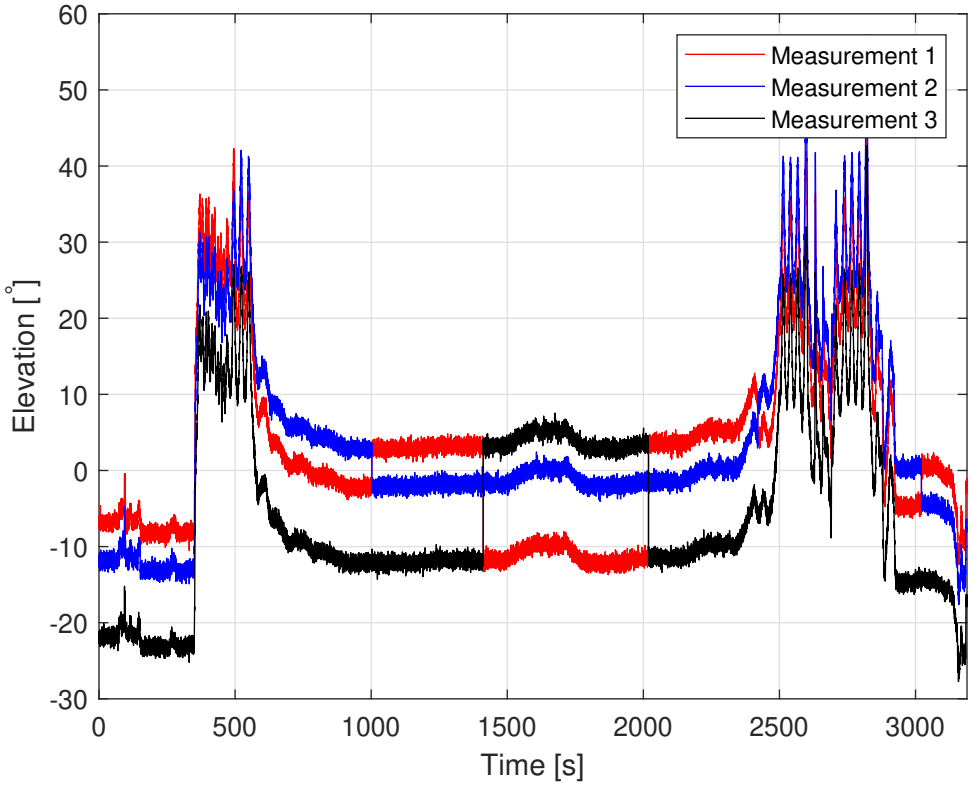

Figure 4.9: The 3 synthetic elevation angles used in the synthetic dataset.

Based on the knowledge of how the lasting intervals of jumps in the elevation angle obtained from the Raudstein dataset, the synthetic dataset is deemed sufficient to display the single target tracking algorithms ability to mitigate the effects of such behavior.

4.4 Ground truth measurements for comparison

To determine the accuracy of the navigation systems state estimates, a ground truth measurement i needed. The Pixhawk IMU and compass together provides an attitude and heading reference system(AHRS), which is used as ground truth for the estimated attitude of the UAV. The position measurement ground truth is provided by RTK-GNSS position measurements. Explained in simple terms, a base station GNSS receiver with predetermined position is set up. By calculating the position of the base station receiver using the GNSS signal carrier-phase, corrections can be calculated. The corrections are broadcast to the UAV GNSS receiver which uses them to account for errors such as atmospheric delays. RTK-GNSS can obtain cm level accuracy for distances up

to 20km away from the base station.[23, p.285] As opposed to regular GNSS postioning which is accurate to a few meters.[23, p.171]

Chapter 5

Results

The navigation system implemented provides the full state vector $\boldsymbol{x}^e_{eb} = [\boldsymbol{p}^e_{eb}, \boldsymbol{v}^e_{eb}, \boldsymbol{q}^e_b, \boldsymbol{b}^b_{acc}, \boldsymbol{b}^b_{ars}]^T$. In which $\boldsymbol{x} \in \mathbb{R}^{16}$. In this thesis however it is of most interest to examine the position estimates, and see if these improve by using single target tracking algorithms. Therefore, in this chapter only the position estimates will be presented and compared to the ground truth measurements from RTK-GNSS. Statistics and plots of the estimates of the velocity, attitude and IMU biases can be found in appendix C and D respectively. They are presented in a similar structure as this chapter. The velocity error displayed similar performance as the offline results presented in [24, Ch.14.5.1] by Gryte. The attitude error was in general up to 3° greater in this thesis compared to [24, p.162], with the largest error being the yaw angle. The velocity and attitude estimates of the different algorithms yielded similar results with both datasets.

5.1 The Agdenes dataset

The first analysis were performed on the dataset recorded by Okuhara et.al. in [18]. The tuneable parameters in the MEKF is the matrices $\boldsymbol{Q}$ and $\boldsymbol{R}$ which describe the process- and measurement noise respectively. As mentioned previously it is crucial to give the MEKF good initial state estimates for the filter to converge. The tuning of the MEKF is given in appendix B.

5.1.1 One measurement using the largest peak

As explained in chapter 4.2, the 4 largest peaks in the pseudospectrum generated from the PARS system was extracted to be used in the tracking algorithm. Each peak represents a received signal from a specific direction. In the original system only the largest peak, equating to the

received signal which yielded the best communication channel, was used in the MEKF. To compare the performance of the tracking algorithms it is important to understand how well the existing system would perform on the given data. Therefore the analysis was first performed using the DoA measurement corresponding to only the strongest peak in the pseudospectrum without any tracking algorithms. This yielded the position error-statistics given in table 5.1. Note that the error in the down direction is very large compared to the north- and east direction. Comparing these results to the one obtained by Gryte [24, p.166] in a previous flight experiment with the same UAV above the ocean shows that the RMSE in the north position is 1.42° smaller than that obtained in with the Agdenes dataset.

Table 5.1: Positions estimate error using only the strongest peak in the DoA pseudospectrum, compared to the RTK-GNSS calculated position.

	North [m]	**East** [m]	**Down** [m]	**Norm** [m]
ME:	7.12	2.21	-35.80	36.57
MAE:	8.54	3.53	39.42	40.49
STD:	7.13	3.95	48.08	48.76
RMSE:	10.08	4.52	59.94	60.95

Figure 5.1 and 5.2 displays the difference between the ground truth RTK-GNSS position compared to the estimated position, in 2D and 3D respectively. It is clear that the vertical position is most affected by the multipath propagation.

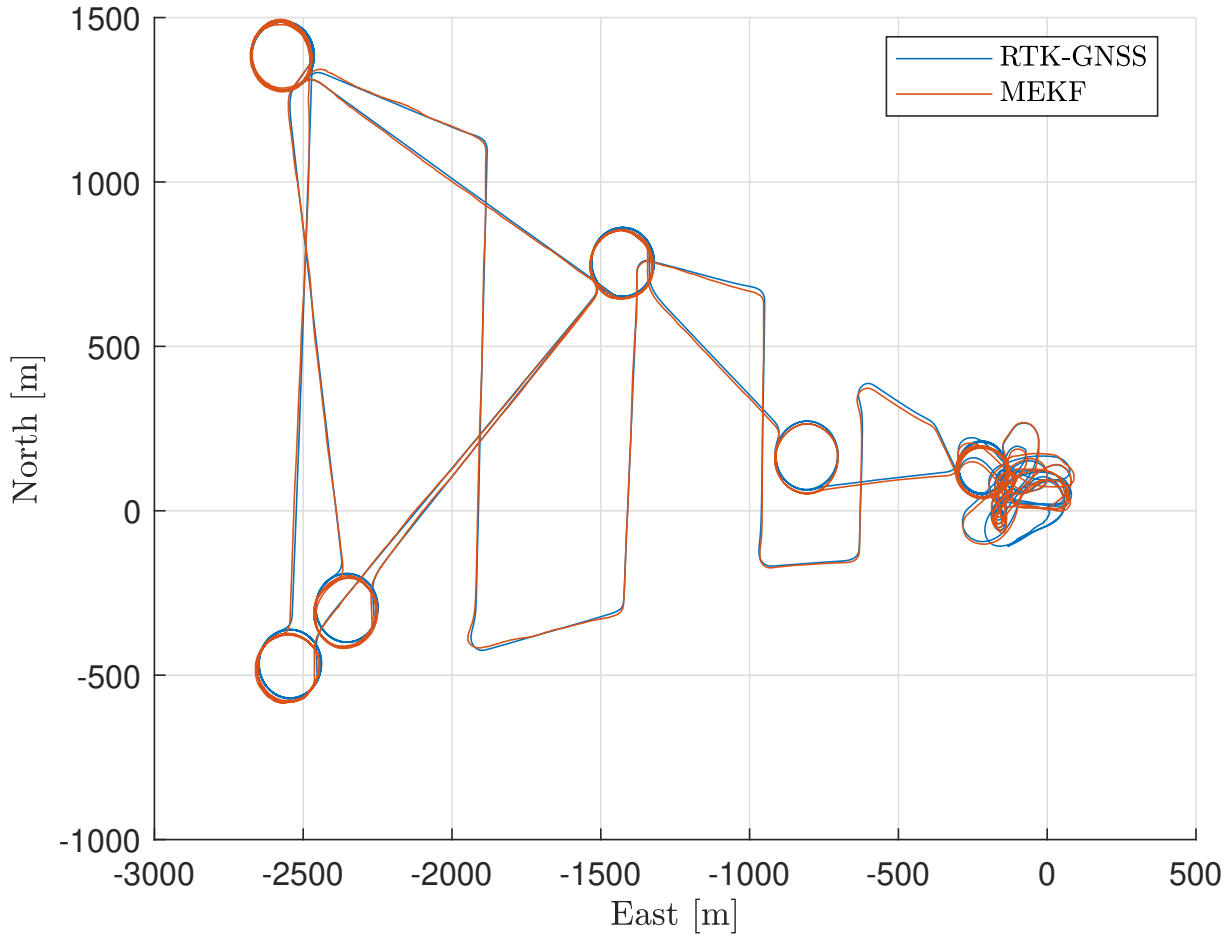

Figure 5.1: 2D position(North-East) estimate of the UAV relative to the position measurement provided by RTK-GNSS measurements.

Further figure 5.3 gives a different a perspective of the position estimate in each direction. While figure 5.4 displays the error in the position estimate compared to RTK-GNSS.

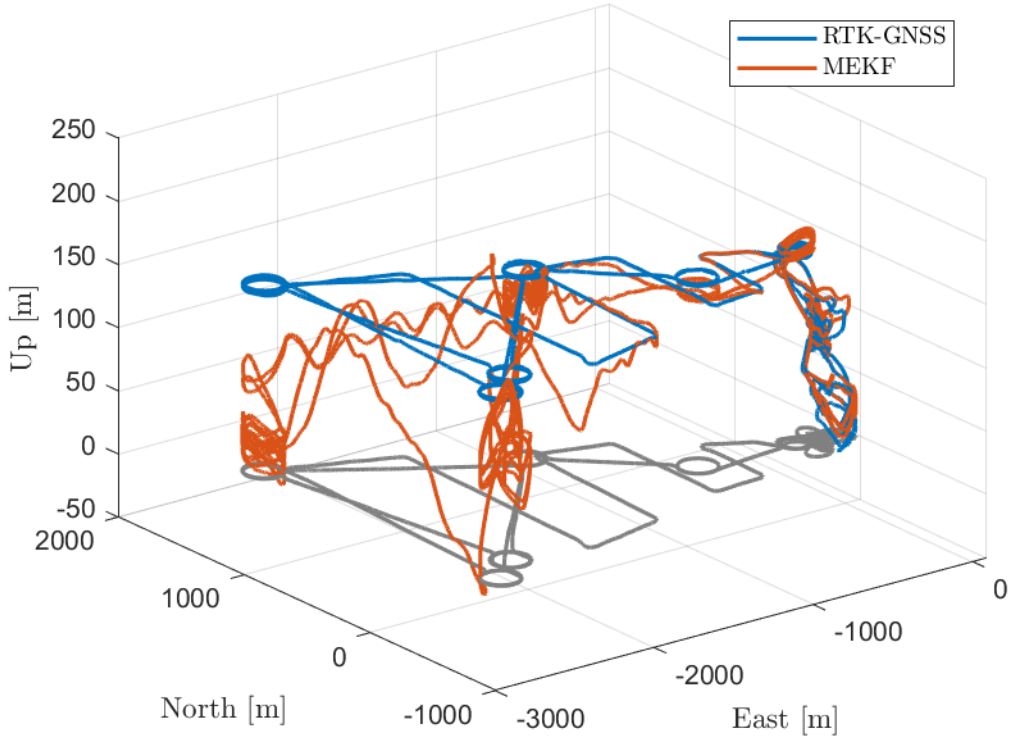

Figure 5.2: Local 3D position estimate of the UAV relative to the position measurement provided by RTK-GNSS measurements.

In figure 5.4 it can be observed that the position error in the north and east direction is outside 3 standard deviations of the MEKF covariance in the beginning and end of the flight. It also observed in the subsequent position error plots in the result chapter. It happens in the region where the UAV switches between being outside and inside the PARS ground antennas viewing frustum. This points to there maybe being in error in how the RTK-GNSS measurements is inserted into the PARS measurements. Another reason could be that a slight offset between the PARS- and RTK-GNSS measurements has been observed. The error is calculated by comparing the RTK-GNSS position with the estimated position. The intervals where RTK-GNSS measurements are used result in the sudden jumps to inside the 3σ region. This observation gives a possible explanation to why the error in the north position is higher in this result when compared to that obtained by Gryte[24, p.166] in a similar flight experiment above the ocean.

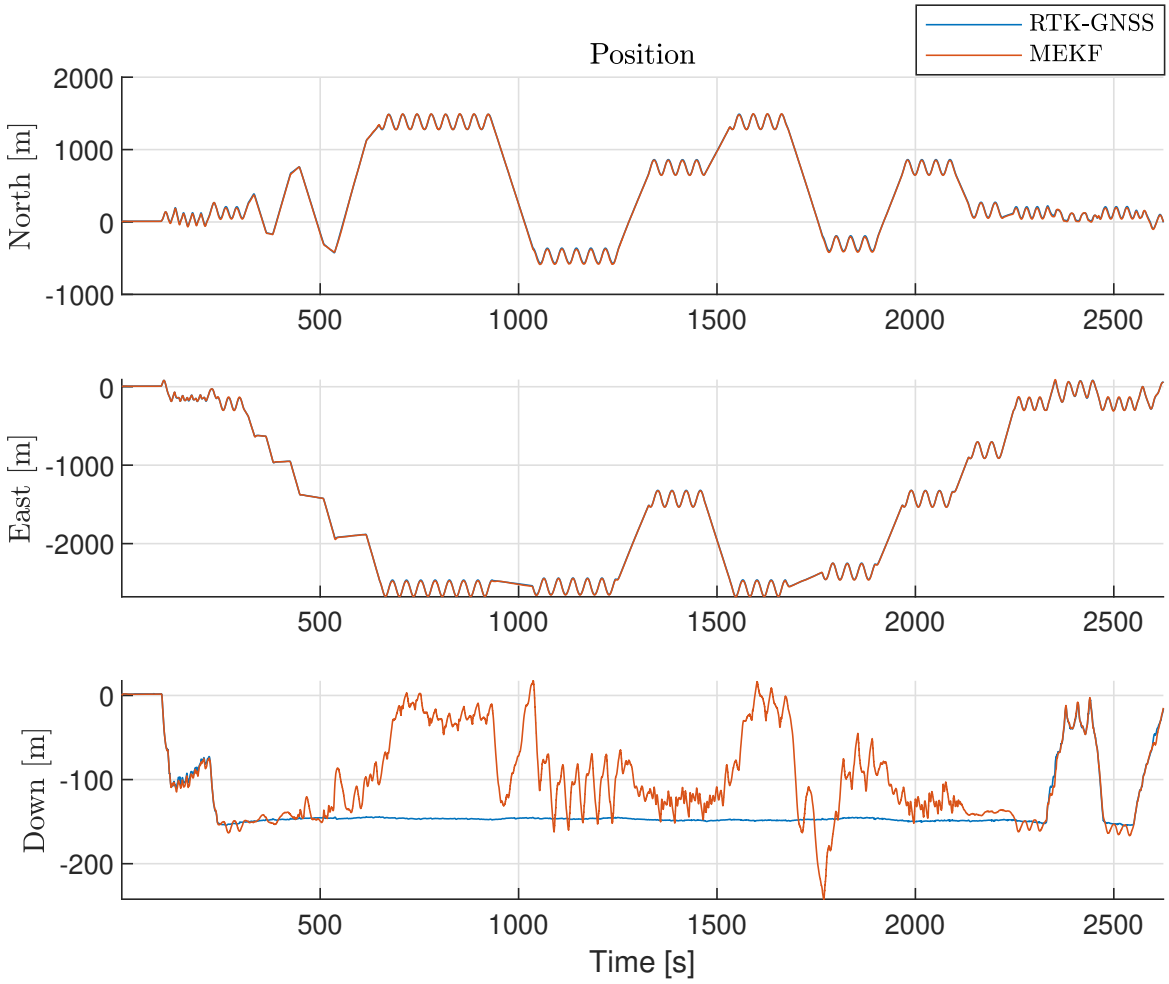

Figure 5.3: Estimated position in the North-, east-, and down direction respectively, relative to the position provided by RTK-GNSS measurements.

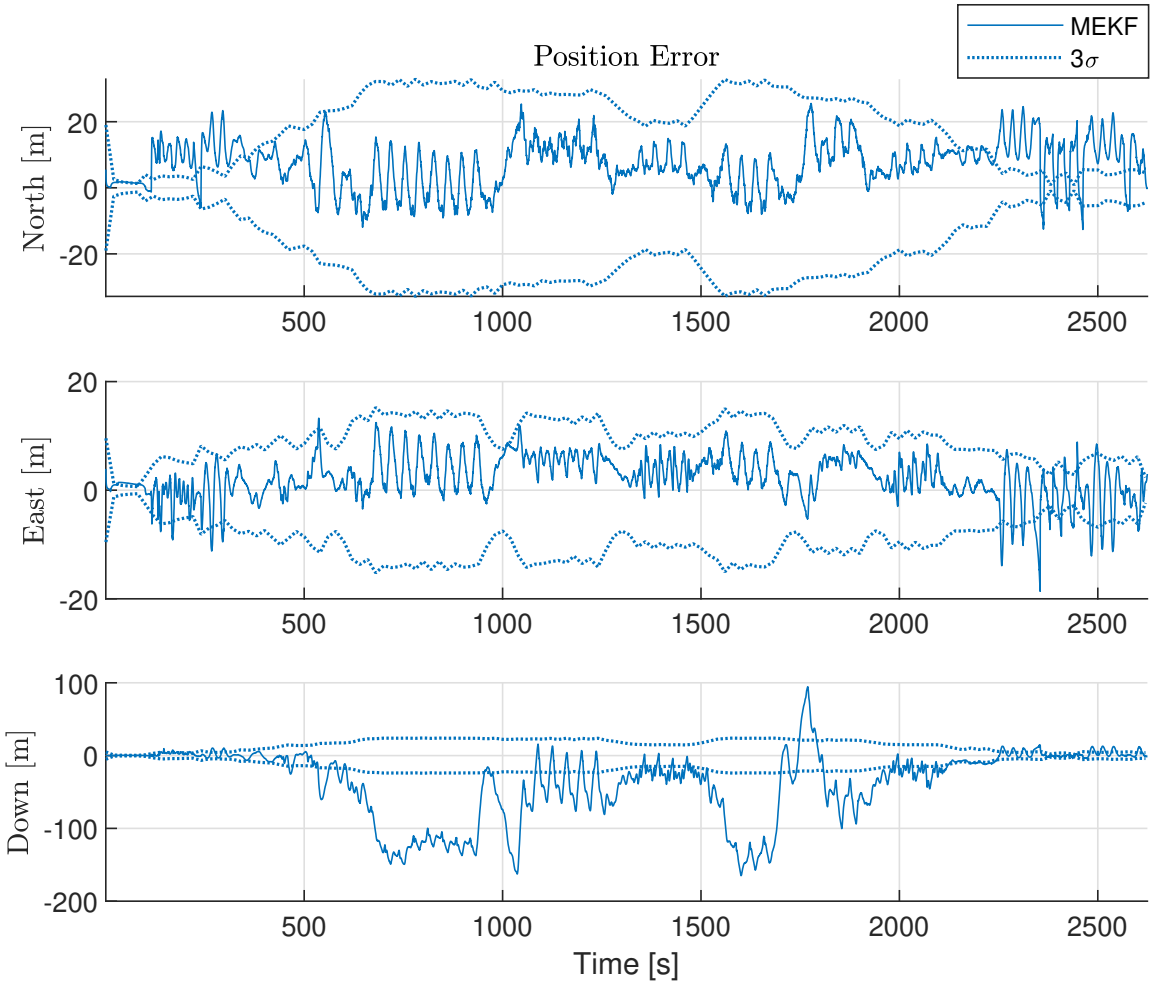

Figure 5.4: Estimated position error relative to the RTK-GNSS position. The dotted lines displays 3 times the standard deviation of the MEKF covariance.

5.1.2 Nearest Neighbor Filter

With 4 extracted peaks corresponding to 4 different azimuth- and elevation measurements, the NN filter was applied. The resulting error statistics are shown in table 5.2.

Table 5.2: Estimate positions error using the 4 largest peaks in the DoA pseudospectrum when applying the NN filter. Relative to the RTK-GNSS calculated position.

	North [m]	**East** [m]	**Down** [m]	**Norm** [m]
ME:	7.14	2.22	-35.59	36.36
MAE:	8.54	3.54	39.23	40.30
STD:	7.10	3.95	47.85	48.54
RMSE:	10.06	4.53	59.63	60.65

Comparing the results in table 5.2 with the ones obtained when only utilizing the strongest peak shows that the differences in estimation accuracy are insignificant. This can also be seen in figure 5.5 which shows the estimated position error in each direction compared to RTK-GNSS. This looks very similar to figure 5.4.

Figure 5.6 may be the explanation of this. It shows that it is mostly the first measurement, which corresponds to the strongest peak in the DoA pseudospectrum, that is gated and used in the NN filter. Since the first measurement is the only measurement that is gated through the majority of the flight the results will be similar. The small differences can be attributed to the few instances where several measurements are gated. For the very first part of the flight all 4 measurements are gated. The same holds for some intervals in the last part of the flight. This is due to the RTK-GNSS measurements that has been added to dataset when the UAV is outside the viewing frustum of the PARS ground station. Either way it seems like the other measurements in the dataset is mostly clutter.

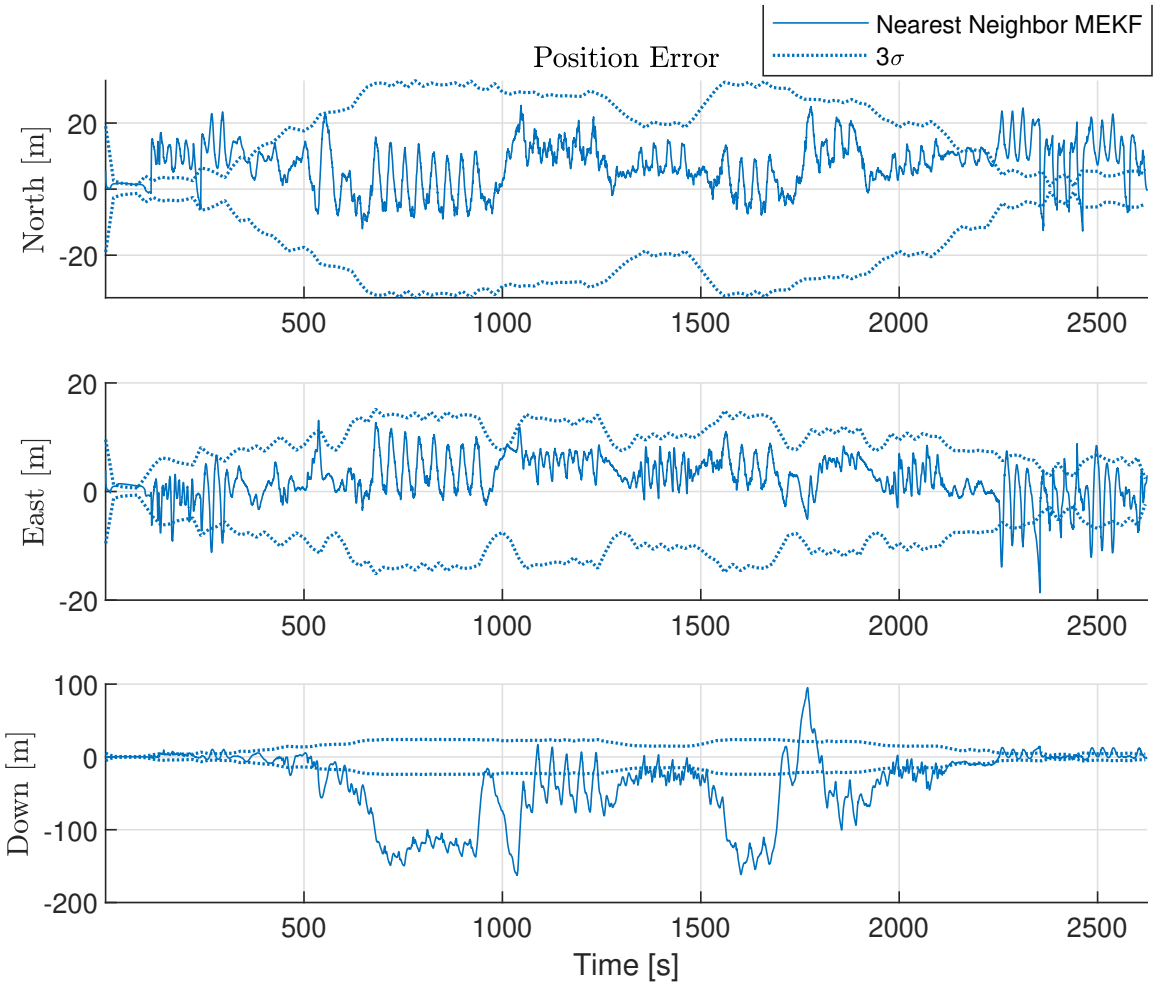

Figure 5.5: Position error in the North-, east-, and down direction respectively using the NN filter, relative to the position provided by RTK-GNSS measurements. The dotted lines represent 3 times the standard deviation of the MEKF covariance.

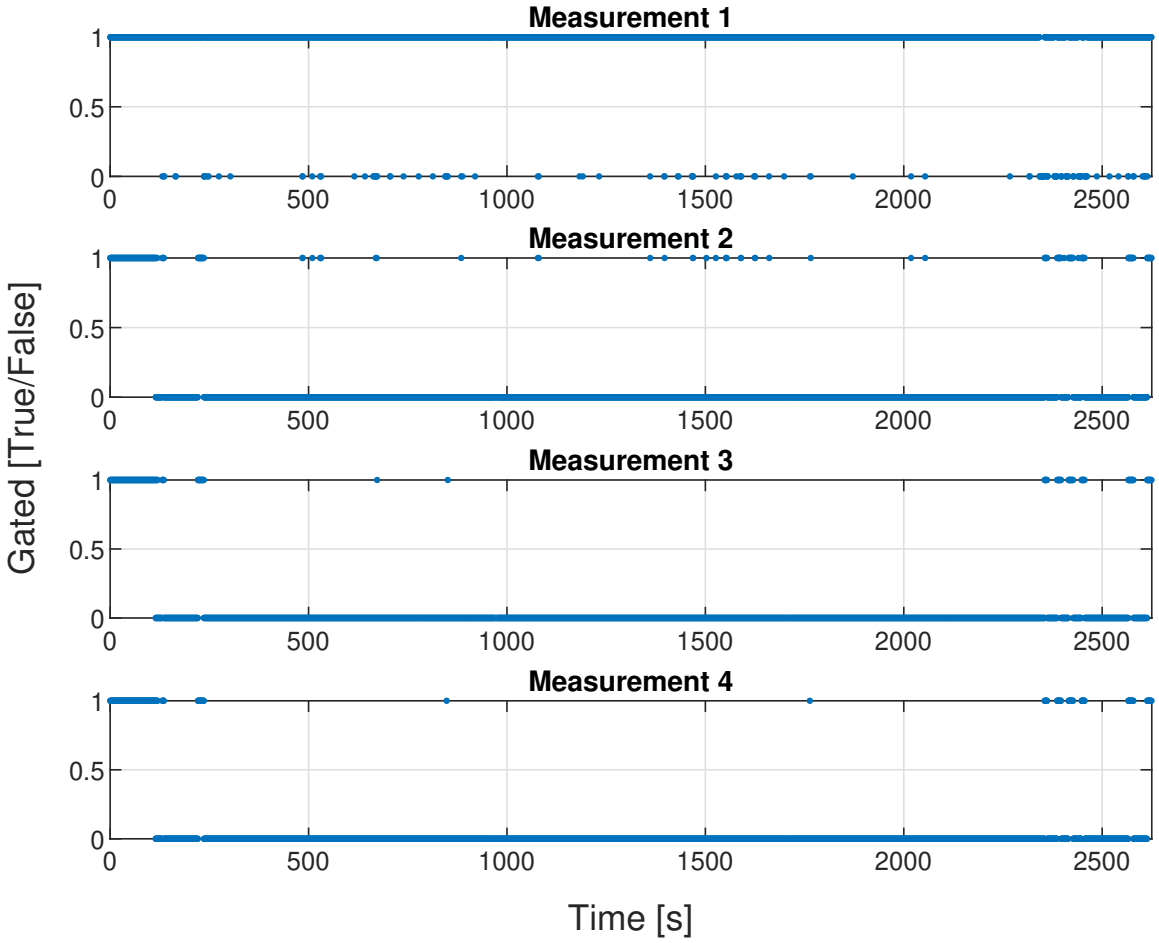

Figure 5.6: Displays whether a measurement passed through the validation gate or not. 1 means that the measurement is gated, while 0 means that it is not.

5.1.3 Probabilistic Data Association Filter

Even though the Agdenes dataset seems to mainly be affected by oscillations in the elevation angle due to multipath interference, it is still of interest to see the results obtained by applying the PDA filter.

The tuneable parameters in PDA filter are the clutter density λ, the probability of detection P_D. Typical values for P_D in radar tracking applications is around $P_D = 0.95$. It is a reasonable assumptions that the PARS will have higher probability of detection as the UAV is continuously transmitting a signal to the PARS ground station. Especially since both the direct signal and the multipath signals are monitored. It is therefore set to $P_D = 0.99$, as $P_D = 1$ would be unrealistic since the PARS ground antenna will experience some time steps where target is undetected. The PDA can either utilize the Poisson clutter model, or the diffuse clutter model. Both were implemented and tested on the dataset.

Different values for the clutter density, λ, were tested on the dataset. The resulting estimation error statistics for some different clutter density values are shown in table 5.3. The table shows that while the differences are small, $\lambda = 10^{-6}m^{-3}$ yielded the best estimation accuracy in terms of MAE and RMSE. Using the diffuse clutter model yielded similar performance to that of $\lambda = 10^{-4}$ and $\lambda = 10^{-6}$ as the estimated value for the clutter density was within this interval, depending on the number of gated measurements. As the clutter density, λ, was set to even smaller values, the algorithm weighted the measurements more, and put less emphasis on the a priori nominal state $\boldsymbol{x}^e_{eb,nom}$, with β_0.

Table 5.3: Norm of estimated position error using PDA for with different values for the clutter density. Using the RTK-GNSS position as reference.

Clutter density $[m^{-3}]$	**ME** $[m]$	**MAE** $[m]$	**STD** $[m]$	**RMSE** $[m]$
$\lambda = 10^{-4}$:	34.88	41.12	53.17	63.59
$\lambda = 10^{-6}$:	35.91	39.85	48.45	60.31
$\lambda = 10^{-9}$:	35.59	40.31	48.53	60.65
$\lambda = 10^{-12}$:	36.37	40.31	38.53	60.65

Figure 5.7 shows the association probabilities throughout the flight for the PDA filter with $\lambda = 10^{-6}m^{-3}$. Note that the time steps where no blue dot are visible means that the respective measurement was not gated, and therefore given an association probability of 0. With the exception of some time steps, the first measurement is the only gated measurement, and it's respective

association probability β_1 is close to 1 for the majority of the flight. There are some instances where the PDA filter seem to trust measurement 1 less, which is reflected in it's lower weighting and increasing the belief in the prediction with β_0. In the same manner as in the results with the NN filter, the parts where all measurements are weighted equally is the time steps where the RTK-GNSS position is used due to PARS measurement saturating when the UAV is outside the viewing frustum. Since all measurements are the same in these instances, they are weighted equally with $\beta_i \approx 0.25$.

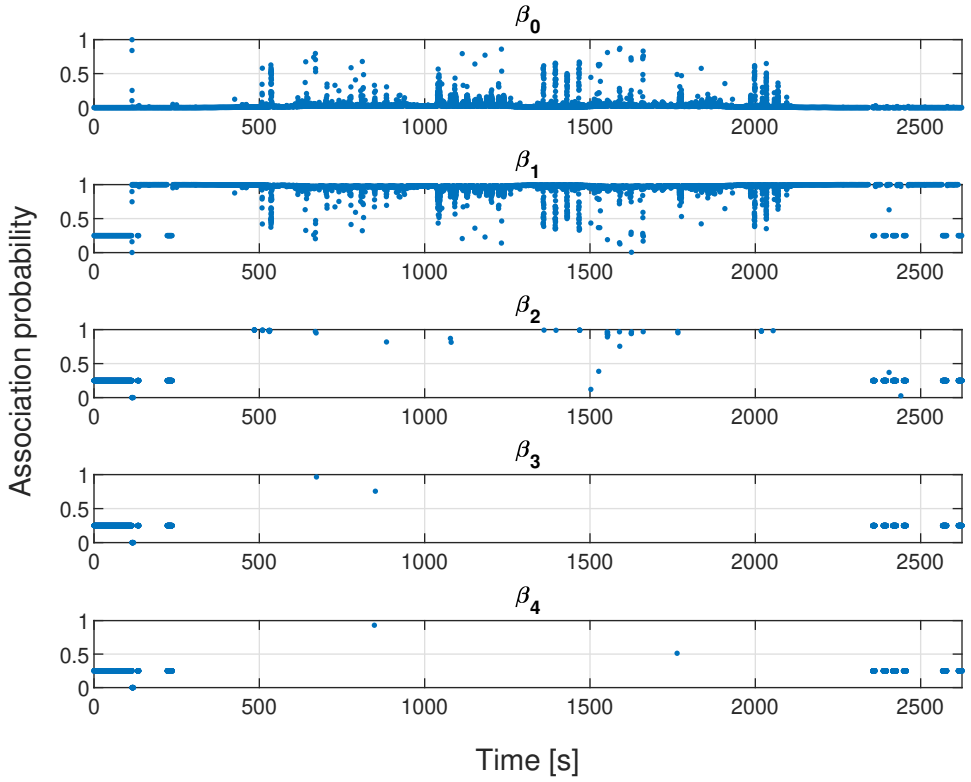

Figure 5.7: Association probabilities for PDA with $P_D = 0.99$ and $\lambda = 10^{-6}m^{-3}$. If no probability is plotted it means that the corresponding measurement was not gated.

Figure 5.8 displays the estimated position error of the PDA filter with = $10^{-6}m^{-3}$ relative to the RTK-GNSS position. It is almost identical to that of the standard MEKF and the NN filter, in figure 5.4 and 5.5 respectively.

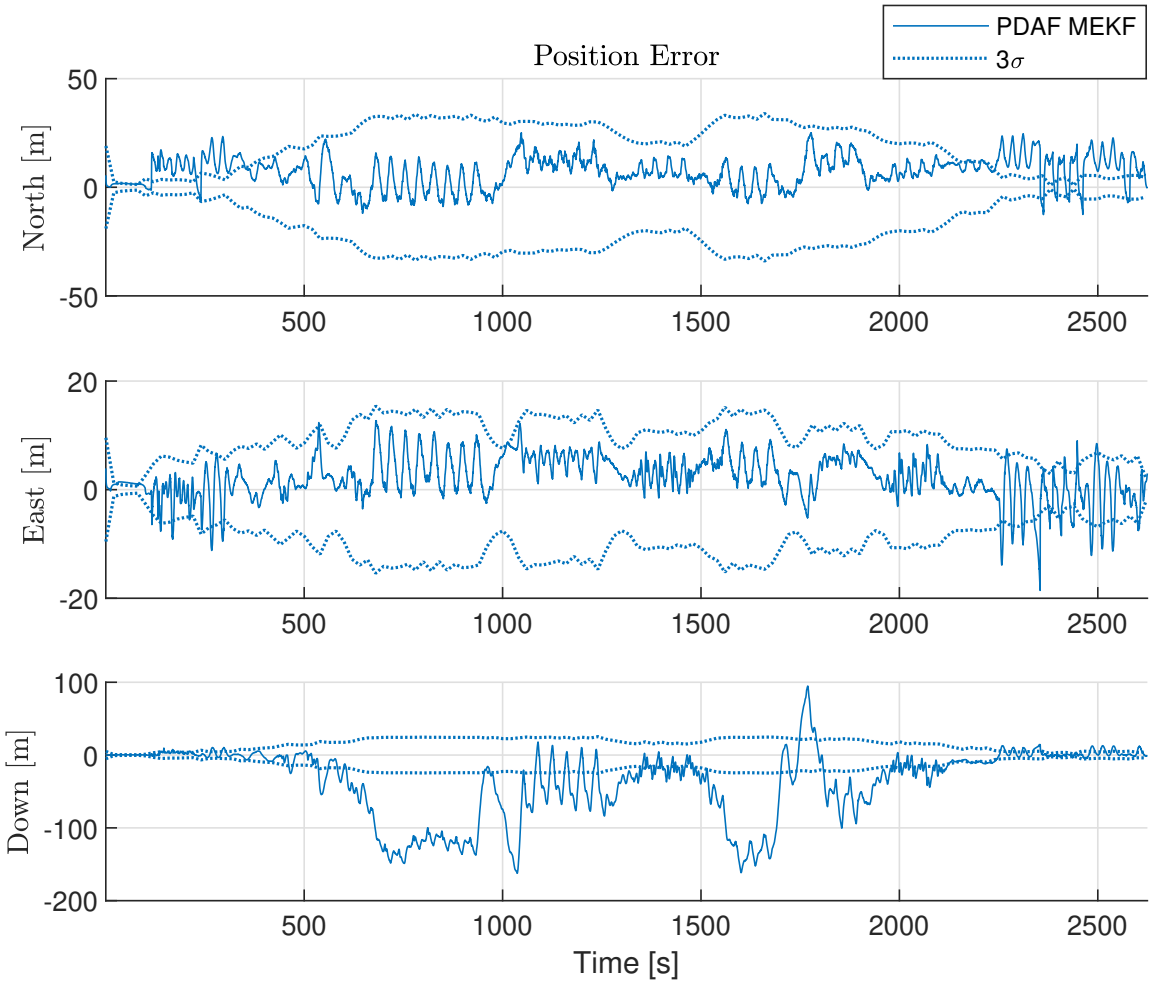

Figure 5.8: Estimated position error in the North-, east-, and down direction respectively using the PDA filter with $P_D = 0.99$ and $= 10^{-6}m^{-3}$, relative to the position measurement provided by RTK-GNSS measurements. The dotted lines represent 3 times the standard devation of the MEKF covariance.

Detailed error statistics with the PDA filter using $\lambda = 10^{-6}m^{-3}$ is given in 5.4 Comparing the error statistics tables for each method displays that the RMSE improvement between using the largest peak in the DoA spectrum in the standard MEKF is only improved by $0.65m$ to the norm when using the PDA filter. Applying the NN- and PDA filter does not result in big improvements for the navigation system on the Agdenes dataset.

Table 5.4: Position error in the North-, east-, and down direction respectively using the PDA filter with $P_D = 0.99$ and $\lambda = 10^{-6}m^{-3}$. Relative to the position provided by RTK-GNSS measurements.

	North [m]	**East** [m]	**Down** [m]	**Norm** [m]
ME:	7.13	2.16	-35.13	35.91
MAE:	8.50	3.49	38.78	39.85
STD:	7.05	3.93	47.77	48.45
RMSE:	10.03	4.49	59.30	60.31

5.1.4 Observations

Through the work on this thesis the group working on the PARS aided navigation project discovered that the problem of multipath propagation was effecting the system in two different ways rather than one. Initially it was observed that the PARS sometimes would interpret the signal reflection from the ocean surface as the true direct signal. This is most likely due to PARS being designed for communication and that the reflected signal yielded a better communication line. This effect has been shown to be the case in some recorded datasets where periodical jumps in the elevation angle measurement appears mid-flight. The other problem that multipath propagation introduces is interference. When the signal bounces of the ocean surface and surrounding infrastructure it interferes with the direct signal from the UAV. This is is visible as oscillations in the DoA estimates of the signal. It is especially visible in the elevation angle, and results in a poorer estimate of the vertical position of the UAV. The results from the Agdenes dataset seem to indicate that it mainly is multipath interference that affects the PARS during the flight experiment. Since measurement 1 seems to be the direct signal, but with an unreliable elevation measurement, the difference between the standard MEKF and tracking algorithms performance is insignificant.

5.2 Synthetic dataset

The results from testing the NN- and PDA filter on the synthetic dataset is presented in the following sub-chapters. To have a basis result to compare the NN- and PDA filter performance to, the correct RTK-GNSS calculated elevation angle with added Gaussian white noise is used to find a benchmark result. This will represent the best possible result given that the tracking algorithm always chooses the correct measurement. The position error is shown in table 5.5.

Table 5.5: Positions estimate error using the RTK-GNSS calculated elevtion angle with added Gaussian white noise in the standard MEKF. Compared to the RTK-GNSS calculated position without added noise.

	North $[m]$	**East** $[m]$	**Down** $[m]$	**Norm** $[m]$
ME:	7.47	0.73	0.12	7.51
MAE:	8.23	1.88	1.65	8.60
STD:	5.89	2.32	2.11	6.68
RMSE:	9.52	2.44	2.11	10.05

5.2.1 Nearest Neighbor

The error statistics when using the NN filter on the 3 synthetic position measurements are shown in table 5.6. The results indicate that the NN filter is able to choose the correct measurement consistently, as the results is almost exactly similar to those obtained in the benchmark results. The MAE and RMSE in the down direction is slightly larger, by $0.12m$, than in the benchmark results.

Table 5.6: Positions estimate error using NN filter with the 3 synthetic measurements. Compared to the RTK-GNSS calculated position without added noise.

	North $[m]$	**East** $[m]$	**Down** $[m]$	**Norm** $[m]$
ME:	7.46	0.73	0.04	7.49
MAE:	8.22	1.89	1.77	8.62
STD:	5.90	2.33	2.23	6.72
RMSE:	9.51	2.44	2.23	10.07

Figure 5.9 displays the fact that there are always two measurements gated throughout the entirety of the flight. These are the direct signal and the same signal with a -5° offset in the elevation angle. The NN filter chooses the direct signal, as this is closer to the predicted measurement, which is why it's performance is similar to the benchmark results.

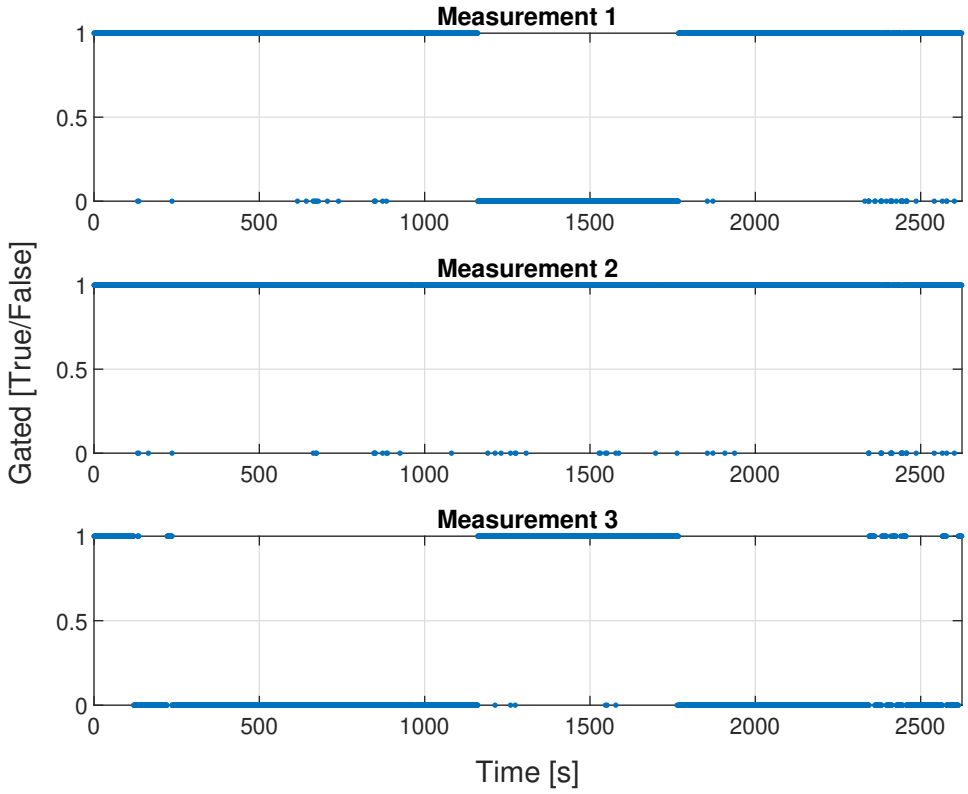

Figure 5.9: Which measurements are passed true the validation gate throughout the flight. 1 means that the measurement is gated, while 0 means that it is not.

5.2.2 Probabilistic Data Association Filter

With $P_D = 0.99$ and different clutter density values, the PDA filter was tested on the synthetic dataset. The results are shown in table 5.7. The same effect when reducing the clutter density was observed for the synthetic dataset. As λ was chosen smaller, the PDA algorithm weighted the measurements more. $\lambda \geq 10^{-3}$ resulted in a diverging nominal state.

Table 5.7: Norm of position error with RTK-GNSS as reference. Using the PDA filter with different clutter intensities, λ, on the synthetic dataset.

Clutter density $[m^{-3}]$	**ME** $[m]$	**MAE** $[m]$	**STD** $[m]$	**RMSE** $[m]$
$\lambda = 10^{-4}$:	12.66	13.25	9.81	16.01
$\lambda = 10^{-6}$:	12.15	12.80	8.89	15.05
$\lambda = 10^{-9}$:	12.12	12.80	8.90	15.03
$\lambda = 10^{-12}$:	12.12	12.80	8.90	15.03

Although the differences are small, $\lambda = 10^{-9}m^{-3}$ and $\lambda = 10^{-12}m^{-3}$ provided the most accurate estimates. A more detailed overview on the error in each direction in the {n}-frame for the PDA filter with $\lambda = 10^{-9}m^{-3}$ is provided in table 5.8.

Table 5.8: Positions estimate error for the North-, East and Down direction using the PDA filter with $P_D = 0.99$ and clutter intensity $\lambda = 10^{-9}m^{-3}$ on the synthetic dataset. Compared to the RTK-GNSS calculated position.

	North $[m]$	**East** $[m]$	**Down** $[m]$	**Norm** $[m]$
ME:	7.22	1.68	-9.59	12.12
MAE:	8.10	2.33	9.64	12.80
STD:	5.98	2.47	6.10	8.90
RMSE:	9.37	2.99	11.37	15.03

Comparing the performance of the NN filter to the PDA filter reveals a noticeable difference. That is the fact that the MAE in the down direction is $9.64m$ with a standard deviation of $6.10m$ for the PDA filter. The RMSE in the down direction is 11.37 for the PDA filter. The NN filter has a down direction MAE and RMSE equal to $1.77m$ and $2.23m$ respectively. With a standard deviation of $2.23m$. The errors in the North- and East direction is more similar for the two algorithms.

When looking at the way the PDA filter weights each measurement, the reason for the big difference in down direction error becomes clear. Figure 5.10 displays that at least two measurements are gated through the entire flight, similar to the NN filter. The measurement containing the

$-15°$ offset is not passed true the validation gate. It should be noted that GNSS position data is used in approximately the first $100s$ of the flight as the UAV is outside the PARS viewing frustum of the PARS ground antenna. The measurement with the correct elevation angle is weighted with the highest association probability which is varies within $0.8-1$ through the flight. The correct elevation angle is first visible in measurement 1, before it appears in measurement 2 after approximately $250s$. At approximately $750s$ it appears in measurement number 1 once again, and in measurement 3 after around $1200s$ and so on. With the same logic it can easily be seen how the different elevation angles jump between measurements. For more information on the synthetic dataset, see chapter 4.3. Since the wrong measurement also is gated, it has an affect on the estimated error state mixture, which results in a poorer position estimate. The association probability of the measurement containing the elevation angle with a $-5°$ offset varies within approximately $0-0.2$ through the flight.

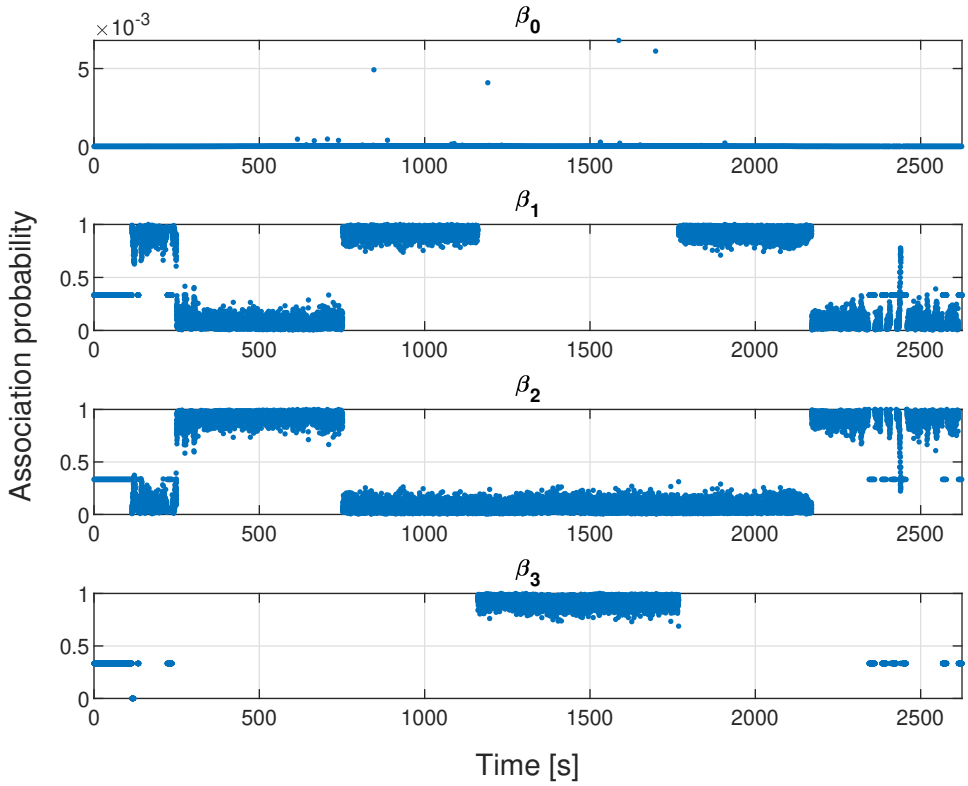

Figure 5.10: Association probabilities, β, for the PDA filter with $P_D = 0.99$ and $\lambda = 10^{-9}$ applied on the synthetic dataset. If no probability is plotted it means that the corresponding measurement was not gated.

Since the association probability of the false gated measurement was in the range of approximately $0-0.2$, it was of interest to tune the PDA filter such that more emphasis was put on the

true measurement. The association probabilities for the gated measurements are obtained by calculating the likelihood ratios of each respectively. The likelihood ratio is obtained from evaluating the predicted measurement distribution at each gated measurement, $\mathcal{N}(\boldsymbol{y}_i; \hat{\boldsymbol{y}}[k], \mathbb{S}[k])$. Making the innovation covariance $\mathbb{S}[k]$ smaller, which in turn makes the predicted measurement distribution more narrow, should result in a smaller likelihood ratio for measurements that are further away from the predicted measurement. To test this the standard deviation of the elevation angle σ_α was lowered from 2° to 1.5° in the noise covariance matrix $\boldsymbol{R}$. This resulted in the PDA calculated association probabilities showed in figure 5.11.

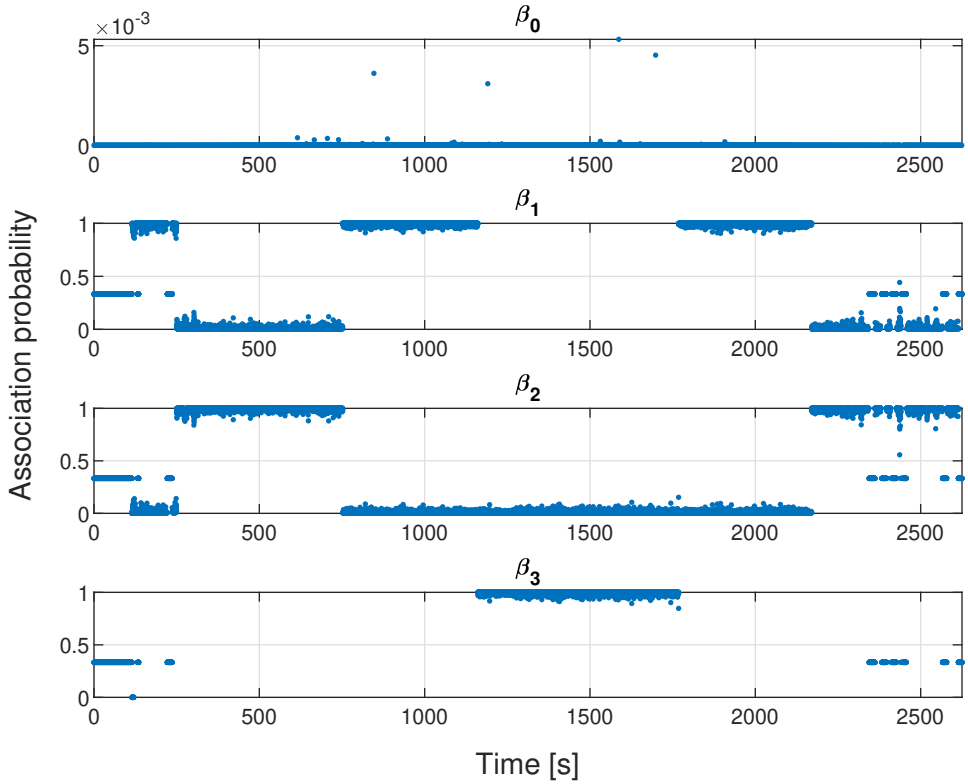

Figure 5.11: Association probabilities, β for PDA with $P_D = 0.99$, $\lambda = 10^{-9}m^{-3}$ and $\sigma_\alpha = 1.5°$. If no probability is plotted it means that the corresponding measurement was not gated.

The corresponding error statistics for the stricter tuning of the PDA filter with $\lambda = 10^{-9}$ is given in table 5.9. It shows that the results become similar to that of the NN filter when the innovation covariance is smaller.

A comparison of the estimated position of the PDA filter with $= 10^{-9}m^{-3}$ and $P_D = 0.99$, with $\sigma_\alpha = 2°$ and $\sigma_\alpha = 1.5°$ is shown in figure 5.12. It displays how making the predicted measurement distribution more sharp, by lowering σ_α, yields a more accurate down position.

Table 5.9: Position estimate error using the PDA filter with $P_D = 0.99$, $\lambda = 10^{-9} m^{-3}$ and $\sigma_\alpha = 1.5$. Synthetic dataset. Compared to RTK-GNSS measurements.

	North $[m]$	**East** $[m]$	**Down** $[m]$	**Norm** $[m]$
ME:	7.56	0.40	-0.90	7.63
MAE:	8.27	1.80	1.66	8.62
STD:	5.82	2.29	2.03	6.58
RMSE:	9.54	2.33	2.22	10.07

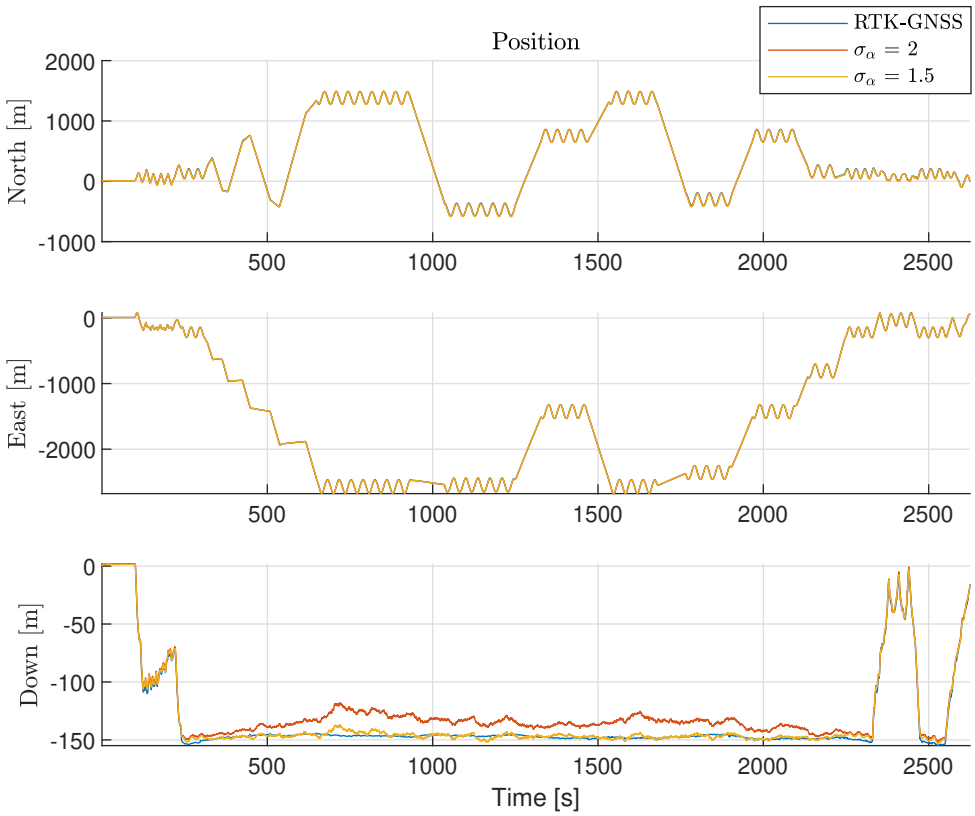

Figure 5.12: Comparison between the estimated position of the PDA filter with = $10^{-9} m^{-3}$ and $P_D = 0.99$, and $\sigma_\alpha = 2°$ and $\sigma_\alpha = 1.5°$. Compared to the RTK-GNSS measurement.

A different perspective is provided in figure 5.13, which shows the position of the UAV in the {n}-frame. It displays that a wider predicted measurement distribution results in a larger weighting of the wrong measurement. Therefore a larger error in the vertical direction.

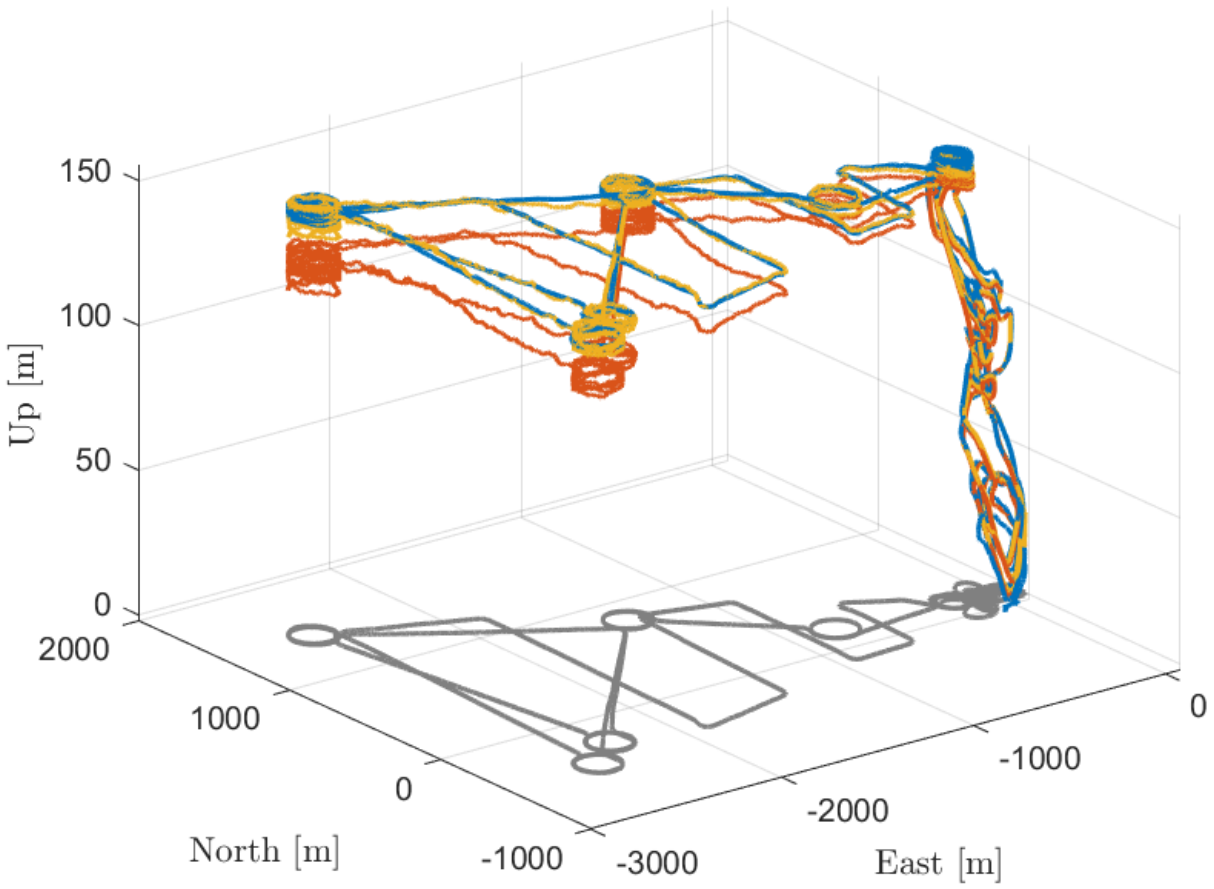

Figure 5.13: Comparison between the estimated position of the PDA filter with = $10^{-9}m^{-3}$ and $P_D = 0.99$. The red line uses $\sigma_\alpha = 2°$ and the orange line uses $\sigma_\alpha = 1.5°$. Compared to the RTK-GNSS measurement.

Chapter 6

Discussion

The results presented in the previous chapter displayed how well the NN- and PDA filter mitigate different multipath effects. This chapter discusses the main findings in the analysis.

6.1 The dataset and measurement extraction

There could be several reasons for why the Agdenes dataset did not display longer intervals of the PARS system choosing the wrong DoA measurement. This may originate from how the different DoA measurements are extracted from the pseudospectrum. Finding the largest peak in the pseudospectrum is easy, but to keep track of several smaller peaks is a harder task. As observed in chapter 4 it was mainly one large peak, and several smaller peaks that appeared in the pseudospectrum of the Agdenes dataset. This can be understood from how the 4 extracted azimuth- and elevation angle measurements behaved. Measurement 1 was consistent, albeit noisy with oscillatory behaviour in the elevation angle mid-flight. This points to the strongest peak actually being the direct signal from the UAV through the entirety of the flight. The size of the smaller peaks varies a lot through time, which resulted in the 2nd-4th largest peak jumping back and forth between different DoA measurements rather than consequently keeping track of the same peak. This hypothesis seem to fit with how the extracted DoA measurements appear in the Agdenes dataset.

The same effect was also observed when extracting the largest peaks in the Raudstein dataset. The largest and second largest peak seemed to have a somewhat constant relation to each other, while the smaller peaks however jumped back and forth between different azimuth and elevation angles, resulting in noisy and unreliable measurements. The reason for this may be that the

smaller peaks are weak and highly effected by noise. With a small threshold between which of the smaller peaks is the largest at each time step, the rapid jumps between them are to be expected. This also points to it not being necessary to monitor more than two DoA measurements at once. As the probability of the smaller peaks being gated and used for aiding the INS is very low. Another reason for the highly dynamic behavior of the smaller peaks could be the chosen method on how to extract the DoA angles from the pseudospectrum. Another approach that might have yielded more reliable results would be to utilize an optimization algorithm to search for local maxima.

6.2 Performance of the single target tracking algorithms

The analysis using the Agdenes data showed that it was mainly measurement 1, corresponding to the largest peak in the DoA pseudospectrum that was passed through the validation gate. In previous work as the one performed by Gryte [24, Ch.14.5.1.2] a barometer was implemented due to an unreliable elevation angle measurement. The results while using measurement 1 in the standard MEKF, and 4 measurements in the NN- and PDA filter was almost identical on the Agdenes dataset. The estimated position in the down direction was especially inaccurate. This points towards it being necessary with a barometer to obtain a reliable position estimate. Dealing with the oscillations in the elevation angle is however a problem the single target tracking algorithms was not able to solve.

It was initially expected that extracting more DoA measurements from the PARS pseudospectrum, and applying a single target tracking algorithm on these, would mitigate most of the multipath effects. However, what was not expected was the amount of noisey oscillations that affected elevation angle measurement of the direct signal. The oscillations on the elevation angle is likely caused by constructive and destructive interference between the direct signal and reflected signals from the ocean surface. As measurement 2-4 mainly provided clutter measurements that were considered as outliers by the validation gate, the performance of the single target tracking algorithms cannot be expected to be better than the standard MEKF with an outlier rejection algorithm.

The test on the synthetic dataset was supposed to show how the tracking algorithms would deal with a scenario of the reflected signal becoming stronger than the direct signal, but the

direct signal also being among the set of extracted measurements. The results indicated that the NN filter actually performed better than the PDA filter on the synthetic dataset. The measurement with the -5° offset in the elevation angle was passed through the validation gate together with the direct signal. The PDA filter calculates the association probabilities by evaluating each gated measurement on a predicted measurement distribution. The measurements that are further away from the predicted measurement are less weighted. Gated clutter measurements will therefore degrade the accuracy of the PDA filters estimate of the error state. The PDA filter had to be retuned to make the predicted measurement distribution narrower, and obtain similar results to the NN filter. However what this essentially does in this scenario, is to make the PDA filter tend towards a NN filter. This is because the PDA filter will weight the nearest measurement with an association probability close to 1.

The results are contrary to what is known in tracking literature, as NN is a very simple algorithm compared to the PDA. The reason for the better performance of the NN is likely the lack of clutter measurements in the PARS system compared to a typical scenario such as radar tracking. As a radar receives the reflected signal from the target of interest, it often yields several measurements that appear close to each other in a cluster. If this is the case, it makes sense to evaluate several measurements in the cluster with the PDA filter. As merely choosing the nearest neighbor could lead to worse performance and potentially loss of the track if the wrong measurement is used in the KF update step.

The PDA filter would likely have outperformed the NN filter if more clutter measurements appeared close to the predicted measurement. The synthetic dataset could have included more clutter measurements, but then it would not be an accurate description of the extracted peaks from the Raudstein dataset. The pseudospectrum mainly included one large peak which mostly corresponded to the direct signal from the UAV, and some smaller peaks that were spread out. Creating a scenario with closely spaced measurements around the largest peak in the pseudospectrum would not be a realistic description of the observed data.

In chapter 4 it was shown that a jump of about -16° in the elevation angle was observed between two of the extracted elevation angle measurement in the Raudstein dataset. The measurement corresponded to the two largest peaks in the pseudospectrum. This jump occured because the reflected signal became stronger than the direct signal. The results with the synthetic dataset showed that a jump of this magnitude would be rejected by the validation gate and not consid-

ered by the single target tracking algorithms. This means that the validation gate in it self would be enough to deal with such effects, if both measurements were monitored. Once the reflected signal became stronger than the direct signal, the distance between the predicted measurement and the strongest measurement would yield a too large NIS. This in turn would result in the reflected signal being considered an outlier, while the direct signal would pass through the validation gate and be used in the MEKF update. If the threshold for the validation gate was set to higher value, the reflected measurement would have been considered in the PDA- or NN filter. However in the case of the PDA filter the measurement would likely get a very small association probability with little to no effect on the position estimate. The NN filter chooses the closest measurement, and would choose the direct signal measurement as this is closer to the predicted measurement.

The results seem to indicate that the NN filter would be the suitable single target tracking algorithm for this application. This is because the pseudospectrum provided from the PARS includes peaks with sufficient space between them. A greater perfomance by the PDA filter would likely be observed in a heavily cluttered pseudospectrum with several closely spaced peaks around the largest peak. The similar performance of the PDA- and NN filter, in combination with the discovery of how much multipath interference affected the elevation angle of the direct signal, points towards the need of a new approach. The need for a more complex single target tracking algorithm such as the track-split filter would however be considered unnecessary for this application. It would increase the computational complexity of the navigation system, without necessarily increasing the accuracy of the estimates. This is because single target tracking does not seem to mitigate the interference induced oscillations in the elevation angle.

6.3 A realistic analysis scenario

The analysis in this thesis was performed with the assumption that the navigation system always monitored several peaks in the DoA pseudospectrum. In practice however, this would not be beneficial. First of all the runtime of the system would increase as extracting four or more local maxima for each PARS measurement is more expensive than extracting one. The recorded dataset from Raudstein displayed the reflected signal becoming stronger than the direct signal in small intervals. However, the direct signal corresponded to the largest peak in the pseudospectrum for most of the time throughout the flight experiment. Extracting several measurements from the pseudospectrum would therefore be useless, as measurement 2-4 most

likely would be rejected by the validation gate most of the time.

A more realistic scenario if this were to be implemented in the real navigation system pipeline would be to only monitor the measurement that corresponds to the largest peak in the pseudospectrum. If the measurement is rejected by the validation gate N times, then the two largest peaks in the pseudospectrum should be considered in the next time step. If the system once again detects that one of the two monitored measurements are rejected for several timesteps again, it should go back to only monitoring the largest peak.

From the obtained results in this thesis, the most suitable tracking algorithm for a PARS based navigation system would be the NN filter. By implementing the tracking algorithm as described it should be able to handle cases where the true signal peak becomes smaller than the reflected signal peak in the pseudospectrum. Thereby making it more robust against this kind of multipath effect.

6.4 Dependent multipath measurements

A problem that has not been investigate to a great extent in this thesis is the fact that the PARS spherical position measurements all depend on the same range. Due to the way the range measurement is obtained, only one range measurement is available. All the extracted DoA measurements use the same range when calculating a Cartesian position. The actual range of the reflected multipath signals would however be longer as the multipath signal uses longer time to reach the PARS ground antenna. This means that the calculated positions for the reflected signals are essentially wrong.

Another problem that may arise from this is the fact that we feed the MEKF with more information than we actually have when using several measurement in the PDA filter. The range for the reflected signal is unknown. It may be tempting to compensate for this by scaling the measurement noise variance of the range in the covariance matrix $\boldsymbol{R}$, by the number of monitored measurements. This would likely compensate for the reduced covariance of the state estimate as more information is injected in the MEKF than is actually known. However since the PDA filter performs a normalization procedure on the association probabilities as a part of Gaussian mixture algorithm, it is assumed that the problem can be neglected.

6.5 Further work

The perspective on the task to be solved changed during the work on this thesis as it became apparent that multipath induced oscillations in the direct signals elevation angle measurement is the biggest hurdle to overcome before the full spherical PARS measurement can be used in flights above the sea. Potentially making it possible to remove the need for an additional barometer to measure the vertical position. Hence, single target tracking algorithms alone are not able to solve the problem. However it is a step in the right direction. The use of a simple target tracking algorithm such as the NN filter will make the system more robust in the case where the the reflected signal creates a larger peak in the pseudospectrum than the direct signal. A description of how a practical implementation could look has already been discussed in 6.3.

Further work on the problem in this thesis should involve considering other techniques for extracting the peaks of the pseudsospectrum. As of now a very simple technique is used, and it could be that some of the noise in the extracted DoA measurement stems from this. Investigating the use of optimization based techniques for peak extraction is therefore suggested as further work. The extracted measurements should then be tested on the same algorithms to see whether the robustness of the navigation system has improved.

Chapter 7

Conclusion

Although it initially was expected that single target tracking algorithms would be able to mitigate most of the effect of multipath propagation in a phased array radio system(PARS) aided navigation system, the contrary was displayed in this thesis. Observations of a dataset from a flight experiment at Agdenes, Norway showed that interference between the reflected signals and direct signal from the UAV yielded poor elevation angle measurements. The Nearest Neighbor(NN)- and Probabilsitic Data Association(PDA) filter was implemented and tested on the recorded flight data, but both yielded poor position estimates when using the elevation angle measurements.

A synthetic dataset, based on a recorded dataset from previous flight experiments at Raudstein, Norway, was also created and used to test the algorithms. The synthetic dataset was created to show how the single target tracking algorithms would handle measurement uncertainty with a more reliable elevation angle measurement. It was shown that by monitoring more than one measurement, both the NN- and the PDA filter would make the navigation system more robust against cases where a reflected signal becomes stronger than the direct signal from the UAV. Analysis on both datasets points in the direction of the NN-filter being more suitible algorithm for a PARS aided navigation system, as the appearance of clutter is less dense in PARS compared typical tracking scenarios involving radar measurements.

Other techniques should be looked into for mitigating the multipath induced oscillations in the elevation angle measurement. As of now an additional sensors such as a barometer to measure height is needed to make the PARS aided navigation system have merit as an alternative to global navigation satellite system aided navigation.

Bibliography

[1] Eulalia Balestrieri, Pasquale Daponte, Luca De Vito, and Francesco Lamonaca. Sensors and measurements for unmanned systems: An overview. *Sensors*, 21(4):1518, 2021.

[2] Jules G McNeff. The global positioning system. *IEEE Transactions on Microwave theory and techniques*, 50(3):645–652, 2002.

[3] Hazim Shakhatreh, Ahmad H Sawalmeh, Ala Al-Fuqaha, Zuochao Dou, Eyad Almaita, Issa Khalil, Noor Shamsiah Othman, Abdallah Khreishah, and Mohsen Guizani. Unmanned aerial vehicles (UAVs): A survey on civil applications and key research challenges. *Ieee Access*, 7:48572–48634, 2019.

[4] Prime Air. https://www.amazon.com/Amazon-Prime-Air/b?ie=UTF8&node=8037720011. Accessed: 12.05.2022.

[5] Jasmine Zidan, Elijah I Adegoke, Erik Kampert, Stewart A Birrell, Col R Ford, and Matthew D Higgins. GNSS vulnerabilities and existing solutions: A review of the literature. *IEEE Access*, 9:153960–153976, 2020.

[6] Grace Xingxin Gao, Matteo Sgammini, Mingquan Lu, and Nobuaki Kubo. Protecting GNSS receivers from jamming and interference. *Proceedings of the IEEE*, 104(6):1327–1338, 2016.

[7] Andrew J Kerns, Daniel P Shepard, Jahshan A Bhatti, and Todd E Humphreys. Unmanned aircraft capture and control via GPS spoofing. *Journal of Field Robotics*, 31(4):617–636, 2014.

[8] Mark L Psiaki and Todd E Humphreys. GNSS spoofing and detection. *Proceedings of the IEEE*, 104(6):1258–1270, 2016.

[9] Nasser Gyagenda, Jasper V Hatilima, Hubert Roth, and Vadim Zhmud. A review of GNSS-independent UAV navigation techniques. *Robotics and Autonomous Systems*, page 104069, 2022.

[10] Unmanned Aerial Vehicles Laboratory (UAV-Lab). https://www.itk.ntnu.no/english/lab/unmanned, 2021. Accessed: 14.05.2022.

[11] Sigurd M Albrektsen, Torleiv H Bryne, and Tor A Johansen. Phased array radio system aided inertial navigation for unmanned aerial vehicles. In *2018 IEEE Aerospace Conference*, pages 1–11. IEEE, 2018.

[12] Kristoffer Gryte, Torleiv H Bryne, Sigurd M Albrektsen, and Tor A Johansen. Field Test Results of GNSS-denied Inertial Navigation aided by Phased-array Radio Systems for UAVs. In *2019 International Conference on Unmanned Aircraft Systems (ICUAS)*, pages 1398–1406. IEEE, 2019.

[13] Kristoffer Gryte, Torleiv H Bryne, and Tor A Johansen. Unmanned aircraft flight control aided by phased-array radio navigation. *Journal of Field Robotics*, 38(4):532–551, 2021.

[14] CRE2-189. https://radionor.no/product/cre2-189-2/. Accessed: 29.04.2022.

[15] CRE2-144-LW. https://radionor.no/product/cre2-144-lw/. Accessed: 29.04.2022.

[16] Sigurd M Albrektsen, Atle Sægrov, and Tor A Johansen. Navigation of UAV using phased array radio. In *2017 Workshop on Research, Education and Development of Unmanned Aerial Systems (RED-UAS)*, pages 138–143. IEEE, 2017.

[17] Sigurd M Albrektsen, Torleiv H Bryne, and Tor A Johansen. Robust and secure UAV navigation using GNSS, phased-array radio system and inertial sensor fusion. In *2018 IEEE Conference on Control Technology and Applications (CCTA)*, pages 1338–1345. IEEE, 2018.

[18] Mika Okuhara, Torleiv Håland Bryne, Kristoffer Gryte, and Tor Arne Johansen. Phased Array Radio Navigation System on UAVs: GNSS-based Calibration in the Field. In *2021 International Conference on Unmanned Aircraft Systems (ICUAS)*, pages 210–218. IEEE, 2021.

[19] M Wooley. Bluetooth Direction Finding: A Technical Overview. *Bluetooth Resources*, 2019.

[20] Cort J Willmott and Kenji Matsuura. Advantages of the mean absolute error (MAE) over the root mean square error (RMSE) in assessing average model performance. *Climate research*, 30(1):79–82, 2005.

[21] Edmund Brekke. *Fundamentals of Sensor Fusion, Third edition.* 2020.

[22] T.I. Fossen. *Handbook of Marine Craft Hydrodynamics and Motion Control.* John Wiley & Sons, 2021.

[23] Paul D. Groves. *Principles of GNSS, Inertial, and Multisensor Integrated Navigation Systems*. Artech House, 2008.

[24] Kristoffer Gryte. Precision control of fixed-wing UAV and robust navigation in GNSSdenied environments. 2020.

[25] Takashi Maruyama, Kazunari Kihira, and Hiroaki Miyashita. Phased Arrays. In *Handbook of Antenna Technologies*, pages 1114–1153. Springer, Singapore, 2016.

[26] Zhizhang Chen, Gopal Gokeda, and Yiqiang Yu. *Introduction to Direction-of-arrival Estimation*. Artech House, 2010.

[27] Ralph Schmidt. Multiple emitter location and signal parameter estimation. *IEEE transactions on antennas and propagation*, 34(3):276–280, 1986.

[28] Mohammed AG Al-Sadoon, Nazar T Ali, Yousf Dama, Abdulkareim Zuid, Stephen MR Jones, Raed A Abd-Alhameed, and James M Noras. A new low complexity angle of arrival algorithm for 1D and 2D direction estimation in MIMO smart antenna systems. *Sensors*, 17(11):2631, 2017.

[29] Shahin Farahani. Chapter 5-RF propagation, antennas, and regulatory requirements. *ZigBee Wireless Networks and Transceivers*, pages 171–206, 2008.

[30] Scott R Bullock. *Transceiver and System Design for Digital Communications*. The Institution of Engineering and Technology, 2018.

[31] Rudolph Emil Kalman. A new approach to linear filtering and prediction problems. 1960.

[32] Maria Isabel Ribeiro. Kalman and extended kalman filters: Concept, derivation and properties. *Institute for Systems and Robotics*, 43:46, 2004.

[33] Greg Welch, Gary Bishop, et al. An introduction to the Kalman filter. 1995.

[34] Joan Sola. Quaternion kinematics for the error-state Kalman filter. *arXiv preprint arXiv:1711.02508*, 2017.

[35] Yaakov Bar-Shalom, Fred Daum, and Jim Huang. The probabilistic data association filter. *IEEE Control Systems Magazine*, 29(6):82–100, 2009.

[36] Paul Lanzkron and Eli Brookner. Solid state X-band airport surface surveillance radar. In *2007 IEEE Radar Conference*, pages 670–676. IEEE, 2007.

[37] Mark A Richards, Jim Scheer, William A Holm, and William L Melvin. Principles of modern radar. 2010.

[38] Manav Kumar and Sharifuddin Mondal. Recent developments on target tracking problems: A review. *Ocean Engineering*, 236:109558, 2021.

[39] Fredrik Gustafsson. *Statistical sensor fusion*. Studentlitteratur, 2010.

[40] Yaakov Bar-Shalom and Xiao-Rong Li. *Multitarget-multisensor tracking: principles and techniques*, volume 19. YBs Storrs, CT, 1995.

[41] X Rong Li and Yaakov Bar-Shalom. Tracking in clutter with nearest neighbor filters: analysis and performance. *IEEE transactions on aerospace and electronic systems*, 32(3):995–1010, 1996.

[42] X Rong Li. The pdf of nearest neighbor measurement and a probabilistic nearest neighbor filter for tracking in clutter. In *Proceedings of 32nd IEEE conference on decision and control*, pages 918–923. IEEE, 1993.

[43] findpeaks. Find local Maxima. https://se.mathworks.com/help/signal/ref/findpeaks.html. Accessed: 14.05.2022.

Appendix A

Matlab Toolbox

The code implemented in this thesis can be found in a git repository by following this link. To access the link you need to be connected to the NTNU VPN.

The modifications made to the toolbox can be found in the branch named ***eirik-branch***. The files of interest are all the files in the ***PDAF_tools*** folder and the files ***Observer/Observer_MEKF_4XMRP_ECEF_Tracking.m*** and ***main_runner_raudstein_cre_with_ECEF_Tracking.m***.

Access may be granted by contacting supervisor Kristoffer Gryte at *kristoffer.gryte@ntnu.no*. This is an internal framework for NTNU.

Appendix B

Tuning and equations

B.1 Linear error state kinematics

The error-state kinematics are described by the linear time-variant system:

$$\delta \hat{\boldsymbol{x}} = \boldsymbol{F}(t)\delta \boldsymbol{x} + \boldsymbol{D}(t)\boldsymbol{w}$$

Where the matrices $\boldsymbol{F}(t)$ and $\boldsymbol{D}(t)$ are given by:

$$\boldsymbol{F}(t) = \begin{bmatrix} \mathbf{0} & \boldsymbol{I}_3 & \mathbf{0} & \mathbf{0} & \mathbf{0} \\ \mathbf{0} & -2\boldsymbol{S}(\boldsymbol{\omega}_{\boldsymbol{ie}}^{\boldsymbol{e}}) & \boldsymbol{V}_a & \boldsymbol{V}_{acc} & \mathbf{0} \\ \mathbf{0} & \mathbf{0} & \boldsymbol{A}_a & \mathbf{0} & \boldsymbol{A}_{ars} \\ \mathbf{0} & \mathbf{0} & \mathbf{0} & -\boldsymbol{T}_{acc} & \mathbf{0} \\ \mathbf{0} & \mathbf{0} & \mathbf{0} & \mathbf{0} & -\boldsymbol{T}_{ars} \end{bmatrix}$$

and:

$$\boldsymbol{D}(t) = \begin{bmatrix} \mathbf{0} & \mathbf{0} & \mathbf{0} & \mathbf{0} \\ -\boldsymbol{R}_b^e(\boldsymbol{q}_b^e) & \mathbf{0} & \mathbf{0} & \mathbf{0} \\ \mathbf{0} & -\boldsymbol{I}_3 & \mathbf{0} & \mathbf{0} \\ \mathbf{0} & \mathbf{0} & \boldsymbol{I}_3 & \mathbf{0} \\ \mathbf{0} & \mathbf{0} & \mathbf{0} & \boldsymbol{I}_3 \end{bmatrix}$$

Where $\mathbf{0} = \mathbf{0}_{3x3} = \begin{bmatrix} 0 & 0 & 0 \\ 0 & 0 & 0 \\ 0 & 0 & 0 \end{bmatrix}$. And $\boldsymbol{V}_a = \boldsymbol{R}_b^e \boldsymbol{S}(\hat{\boldsymbol{f}}_{ib}^i)$, $\boldsymbol{V}_{acc} = -\boldsymbol{R}_b^e$, $\boldsymbol{A}_a = -\boldsymbol{S}(\hat{\boldsymbol{\omega}}_{\boldsymbol{ib}}^{\boldsymbol{b}})$ and $\boldsymbol{A}_{ars} = -\boldsymbol{I}_3$.

B.2 Tuning of INS and MEKF

The tunable parameters in the Inertial Navigation System(INS) and the Multiplicative Extended Kalman Filter(MEKF) are shown in the below table. The values are similar to the tuning in [24, p.172].

Table B.1: Tuneable parameters in the INS using MEKF for corrections.

Parameters	Value	Unit of measurement
Initial covariance values:		
$\boldsymbol{P}_{pos}[0]$:	$10^2\boldsymbol{I}_3$	$[m^2]$
$\boldsymbol{P}_{vel}[0]$:	$2^2\boldsymbol{I}_3$	$[\frac{m^2}{s^2}]$
$\boldsymbol{P}_{b_{acc}}[0]$:	$4.72689\cdot10^{-3}\boldsymbol{I}_3$	$[\frac{m^2}{s^4}]$
$\boldsymbol{P}_{b_{ars}}[0]$:	$3.04617\cdot10^{-6}\boldsymbol{I}_3$	$[\frac{rad^2}{s^2}]$
$\boldsymbol{P}_a[0]$:	$diag(\begin{bmatrix}0.03955 & 0.09236 & 0.76797\end{bmatrix})$	$[rad^2]$
Measurement noise covariance:		
σ^2_ρ:	15^2	$[m^2]$
σ^2_ξ	2^2	$[^\circ]$
σ^2_α	2^2	$[^\circ]$
Process noise covariance:		
$\boldsymbol{Q}_{acc}$	$6.5877610^{-4}\boldsymbol{I_3}$	$[\frac{m^2}{s^3}]$
$\boldsymbol{Q}_{ars}$	$9.2146710^{-7}\boldsymbol{I_3}$	$[\frac{rad^2}{s^3}]$
$\boldsymbol{Q}_{b_{acc}}$	$5.3726810^{-8}\boldsymbol{I_3}$	$[\frac{m^2}{s^5}]$
$\boldsymbol{Q}_{b_{ars}}$	$3.2645010^{-15}\boldsymbol{I_3}$	$[\frac{m^2}{s}]$
Bias models:		
$\boldsymbol{T}_{acc}$	3600	$[s]$
$\boldsymbol{T}_{ars}$	3600	$[s]$

The tuning values above form the initial covariance estimate:

$$\boldsymbol{P}[0] = \begin{bmatrix} \boldsymbol{P}_{pos}[0] & \boldsymbol{0}_{3x3} & \boldsymbol{0}_{3x3} & \boldsymbol{0}_{3x3} & \boldsymbol{0}_{3x3} \\ \boldsymbol{0}_{3x3} & \boldsymbol{P}_{vel}[0] & \boldsymbol{0}_{3x3} & \boldsymbol{0}_{3x3} & \boldsymbol{0}_{3x3} \\ \boldsymbol{0}_{3x3} & \boldsymbol{0}_{3x3} & \boldsymbol{P}_a[0] & \boldsymbol{0}_{3x3} & \boldsymbol{0}_{3x3} \\ \boldsymbol{0}_{3x3} & \boldsymbol{0}_{3x3} & \boldsymbol{0}_{3x3} & \boldsymbol{P}_{b_{acc}}[0] & \boldsymbol{0}_{3x3} \\ \boldsymbol{0}_{3x3} & \boldsymbol{0}_{3x3} & \boldsymbol{0}_{3x3} & \boldsymbol{0}_{3x3} & \boldsymbol{P}_{b_{ars}}[0] \end{bmatrix}$$

The process noise covariance matrix:

$$\boldsymbol{Q} = \begin{bmatrix} \boldsymbol{Q}_{acc} & \boldsymbol{0}_{3x3} & \boldsymbol{0}_{3x3} & \boldsymbol{0}_{3x3} \\ \boldsymbol{0}_{3x3} & \boldsymbol{Q}_{ars} & \boldsymbol{0}_{3x3} & \boldsymbol{0}_{3x3} \\ \boldsymbol{0}_{3x3} & \boldsymbol{0}_{3x3} & \boldsymbol{Q}_{b_{acc}} & \boldsymbol{0}_{3x3} \\ \boldsymbol{0}_{3x3} & \boldsymbol{0}_{3x3} & \boldsymbol{0}_{3x3} & \boldsymbol{Q}_{b_{ars}} \end{bmatrix}$$

And the measurement noise covariance matrix:

$$\boldsymbol{R} = \begin{bmatrix} \sigma_{\rho}^2 & 0 & 0 \\ 0 & \sigma_{\xi}^2 & 0 \\ 0 & 0 & \sigma_{\alpha}^2 \end{bmatrix}$$

Appendix C

Results - Statistics

This appendix includes statistics of the velocity and attitude estimates that were not included in the result chapter of the thesis.

C.1 The Agdenes dataset - One measurement using the larges peak

Velocity

Table C.1: Estimated velocity error relative to the Pixhawk GNSS calculated velocity.

	North [$\frac{m}{s}$]	**East** [$\frac{m}{s}$]	**Down** [$\frac{m}{s}$]	**Norm** [$\frac{m}{s}$]
ME:	-0.07	-0.02	0.03	0.08
MAE:	0.48	0.35	0.49	0.77
STD:	0.71	0.52	0.71	1.13
RMSE:	0.71	0.52	0.72	1.13

Attitude

Table C.2: Estimated attitude error relative to the Pixhawk AHRS provided attitude.

	Roll [°]	**Pitch** [°]	**Yaw** [°]	**Norm** [°]
ME:	-0.89	-1.59	-0.39	1.86
MAE:	1.90	2.25	12.82	13.16
STD:	2.38	2.25	16.69	17.01
RMSE:	2.54	2.75	16.70	17.11

C.2 The Agdenes dataset - Nearest Neighbor filter

Velocity

Table C.3: Estimated velocity error relative to the Pixhawk GNSS calculated velocity.

	North [$\frac{m}{s}$]	**East** [$\frac{m}{s}$]	**Down** [$\frac{m}{s}$]	**Norm** [$\frac{m}{s}$]
ME:	-0.06	-0.02	0.03	0.08
MAE:	0.48	0.34	0.49	0.76
STD:	0.71	0.52	0.71	1.13
RMSE:	0.71	0.52	0.71	1.13

Attitude

Table C.4: Estimated attitude error relative to the Pixhawk AHRS provided attitude.

	Roll [°]	**Pitch** [°]	**Yaw** [°]	**Norm** [°]
ME:	-0.89	-1.59	-0.39	1.86
MAE:	1.90	2.25	12.82	13.16
STD:	2.38	2.25	16.69	17.01
RMSE:	2.54	2.75	16.70	17.11

C.3 The Agdenes dataset - Probabilistic Data Association filter

Velocity

Table C.5: Norm of velocity error for different clutter densities, relative to the Pixhawk GNSS calculated velocity.

Clutter density $[m^{-3}]$	**ME** $[\frac{m}{s}]$	**MAE** $[\frac{m}{s}]$	**STD** $[\frac{m}{s}]$	**RMSE** $[\frac{m}{s}]$
$\lambda = 10^{-4}$:	0.09	0.73	1.08	1.09
$\lambda = 10^{-6}$:	0.08	0.76	1.12	1.13
$\lambda = 10^{-9}$:	0.08	0.76	1.13	1.13
$\lambda = 10^{-12}$:	0.08	0.76	1.13	1.13

Table C.6: Estimated velocity error using $P_D = 0.99$ and $\lambda = 10^{-6}m^{-3}$ relative to the Pixhawk GNSS calculated velocity.

	North $[\frac{m}{s}]$	**East** $[\frac{m}{s}]$	**Down** $[\frac{m}{s}]$	**Norm** $[\frac{m}{s}]$
ME:	-0.06	-0.02	0.03	0.08
MAE:	0.48	0.35	0.49	0.76
STD:	0.71	0.52	0.71	1.13
RMSE:	0.71	0.52	0.71	1.13

Attitude

Table C.7: Norm of the attitude error with different clutter densities, relative to the AHRS provided attitude.

Clutter density [m^{-3}]	**ME** [°]	**MAE** [°]	**STD** [°]	**RMSE** [°]
$\lambda = 10^{-4}$:	1.88	13.24	17.10	17.20
$\lambda = 10^{-6}$:	1.86	13.17	17.02	17.12
$\lambda = 10^{-9}$:	1.86	13.16	17.01	17.11
$\lambda = 10^{-12}$:	1.86	13.16	17.01	17.11

Table C.8: Estimated attitude error using $P_D = 0.99$ and $\lambda = 10^{-6}m^{-3}$ relative to the Pixhawk AHRS provided attitude.

	Roll [°]	**Pitch** [°]	**Yaw** [°]	**Norm** [°]
ME:	-0.89	-1.59	-0.38	1.86
MAE:	1.90	2.25	12.82	13.16
STD:	2.38	2.25	16.69	17.01
RMSE:	2.54	2.75	16.70	17.11

C.4 Synthetic dataset - Nearest Neighbor filter

Velocity

Table C.9: Velocity estimate error using the NN filter with the 3 synthetic measurements. Compared to the Pixhawk GNSS calculated velocity.

	North [$\frac{m}{s}$]	**East** [$\frac{m}{s}$]	**Down** [$\frac{m}{s}$]	**Norm** [$\frac{m}{s}$]
ME:	-0.03	-0.06	0.06	0.09
MAE:	0.40	0.29	0.13	0.51
STD:	0.58	0.43	0.20	0.75
RMSE:	0.58	0.43	0.21	0.75

Attitude

Table C.10: Attitude estimate error using NN filter with the 3 synthetic measurements. Compared to the attitude measurement provided by AHRS.

	Roll [°]	**Pitch** [°]	**Yaw** [°]	**Norm** [°]
ME:	-0.89	-1.60	0.20	1.84
MAE:	1.90	2.25	12.96	13.29
STD:	2.38	2.24	16.82	17.13
RMSE:	2.54	2.75	16.82	17.23

C.5 Synthetic dataset - Probabilistic Data Association Filter

Velocity

Table C.11: Estimated velocity error using $P_D = 0.99$, $\lambda = 10^{-9}m^{-3}$ and $\sigma_\alpha = 2°$, relative to the Pixhawk GNSS calculated velocity. Performed on the synthetic dataset.

	North $[\frac{m}{s}]$	**East** $[\frac{m}{s}]$	**Down** $[\frac{m}{s}]$	**Norm** $[\frac{m}{s}]$
ME:	-0.01	-0.05	0.06	0.08
MAE:	0.36	0.26	0.14	0.46
STD:	0.54	0.39	0.20	0.69
RMSE:	0.54	0.40	0.20	0.70

Attitude

Table C.12: Attitude estimate error using PDA filter with the 3 synthetic measurements. Using $P_D = 0.99$ and $\lambda = 10^{-9}m^{-3}$ and $\sigma_\alpha = 2°$. Compared to the attitude measurement provided by AHRS.

	Roll [°]	**Pitch** [°]	**Yaw** [°]	**Norm** [°]
ME:	-0.88	-1.59	0.08	1.82
MAE:	1.89	2.24	12.91	13.24
STD:	2.38	2.25	16.80	17.12
RMSE:	2.54	2.75	16.80	17.21

Synthetic dataset - Retune the noise covariance matrix

Velocity

Table C.13: Velocity estimate error using the PDA filter with the 3 synthetic measurements. Using $P_D = 0.99$, $\lambda = 10^{-9} m^{-3}$ and $\sigma_\alpha = 1.5°$. Compared to the Pixhawk GNSS calculated velocity.

	North $[\frac{m}{s}]$	**East** $[\frac{m}{s}]$	**Down** $[\frac{m}{s}]$	**Norm** $[\frac{m}{s}]$
ME:	-0.03	-0.06	0.06	0.09
MAE:	0.40	0.29	0.13	0.51
STD:	0.58	0.43	0.20	0.75
RMSE:	0.58	0.44	0.20	0.75

Attitude

Table C.14: Attitude estimate error using PDA filter with the 3 synthetic measurements. Using $P_D = 0.99$, $\lambda = 10^{-9} m^{-3}$ and $\sigma_\alpha = 1.5°$. Compared to the attitude measurement provided by AHRS.

	Roll [°]	**Pitch** [°]	**Yaw** [°]	**Norm** [°]
ME:	-0.89	-1.60	0.22	1.85
MAE:	1.90	2.25	12.96	13.29
STD:	2.38	2.24	16.82	17.14
RMSE:	2.54	2.75	16.82	17.24

Appendix D

Results - Figures

This appendix include figures displaying the estimated velocity, attitude and IMU biases that were not included in the result chapter of the thesis.

D.1 The Agdenes dataset - One measurement using the larges peak

Velocity

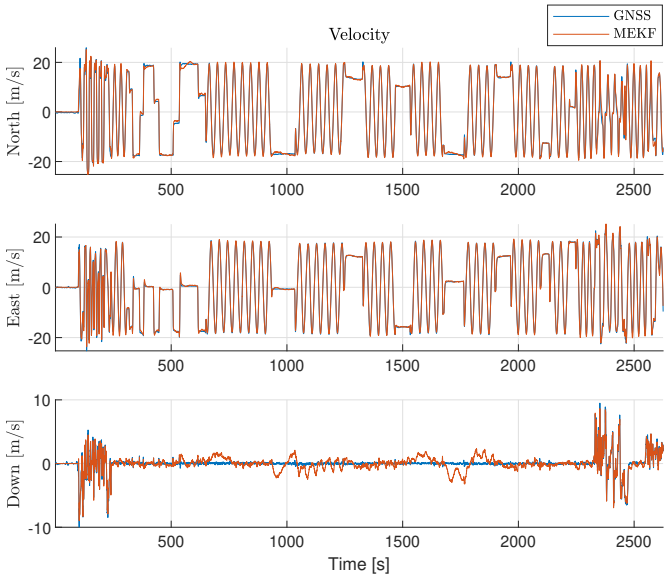

Figure D.1: Estimated velocity compared to the Pixhawk GNSS calculated velocity.

Attitude

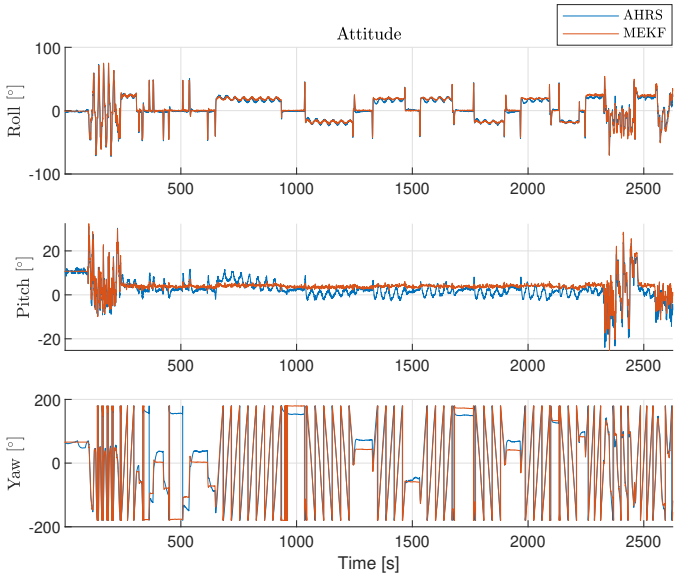

Figure D.2: Estimated attitude compared to the AHRS.

Bias

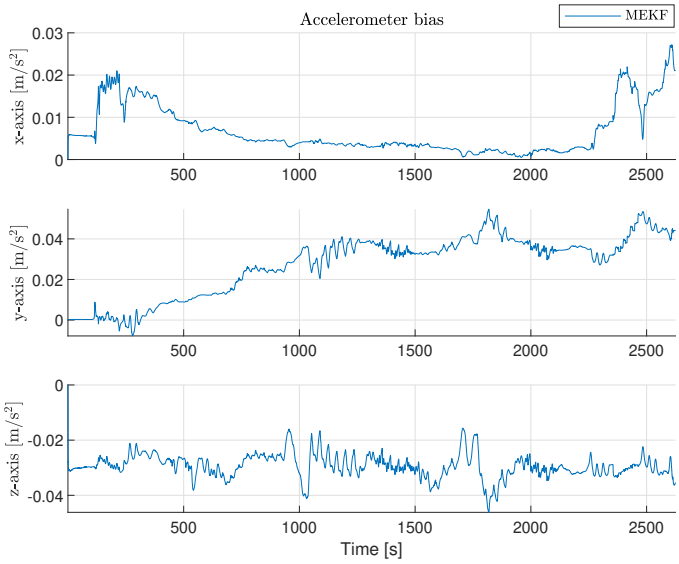

Figure D.3: Estimated accelerometer biases.

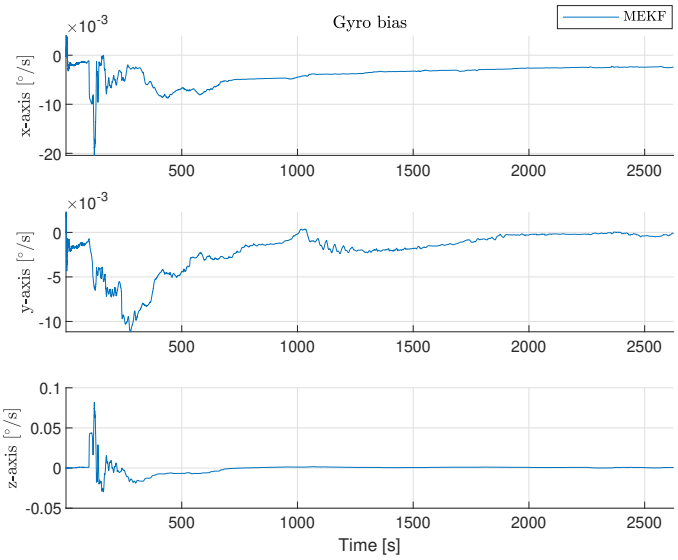

Figure D.4: Estimated gyroscope biases.

D.2 The Agdenes dataset - Nearest Neighbor filter

Velocity

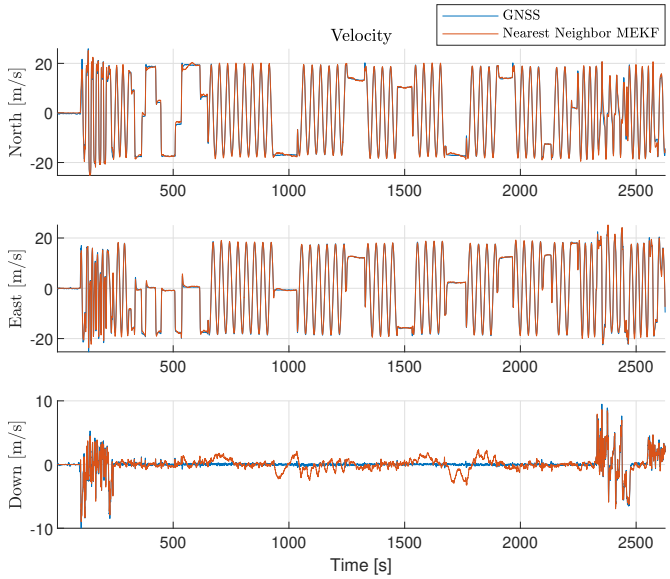

Figure D.5: Estimated velocity using the NN filter compared to the Pixhawk GNSS calculated velocity.

Attitude

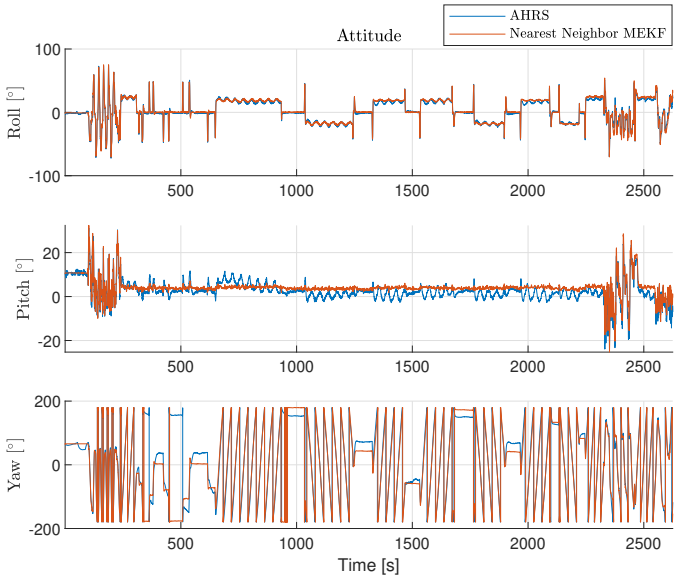

Figure D.6: Estimated attitude using the NN filter compared to the AHRS.

Bias

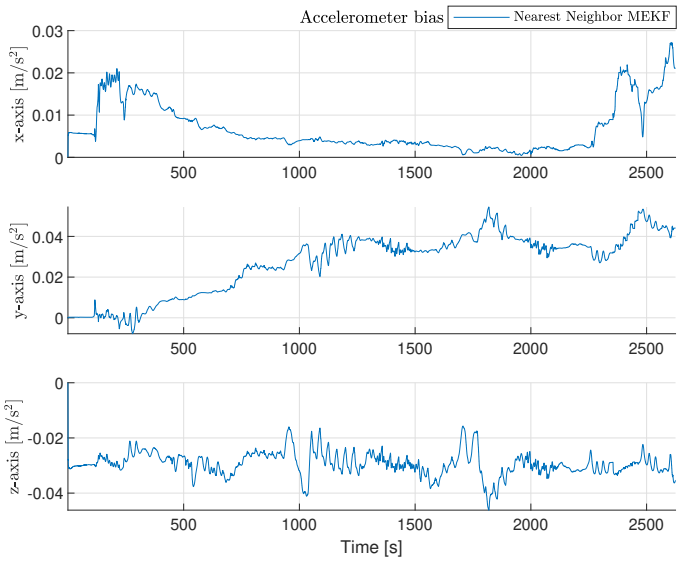

Figure D.7: Estimated accelerometer biases using the NN filter.

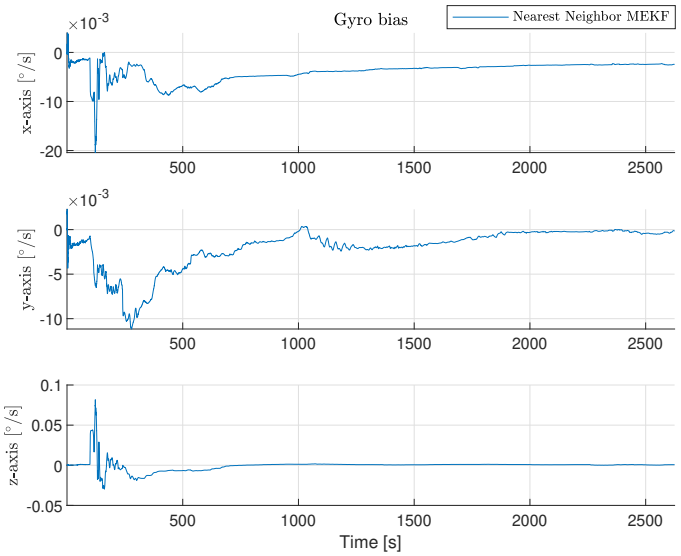

Figure D.8: Estimated gyroscope biases using the NN filter.

D.3 The Agdenes dataset - Probabilistic Data Association filter

Velocity

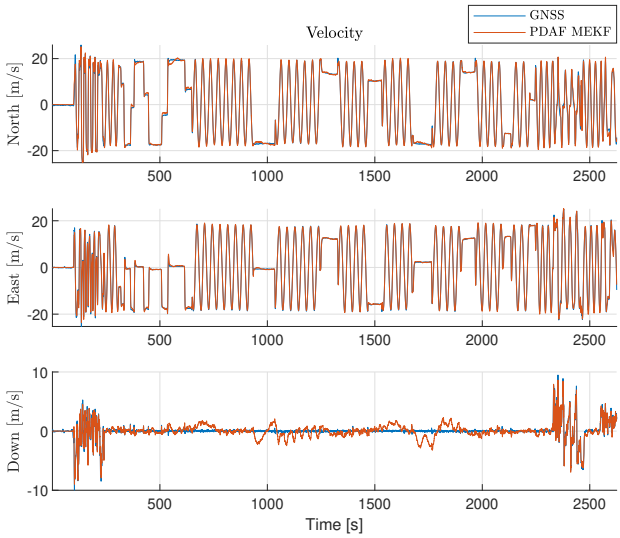

Figure D.9: Estimated velocity using the PDA filter with $P_D = 0.99$ and $\lambda = 10^{-6}m^{-3}$, compared to the Pixhawk GNSS calculated velocity.

Attitude

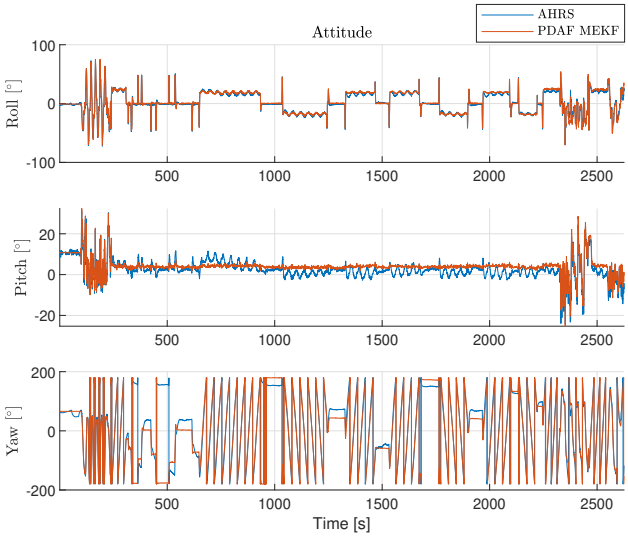

Figure D.10: Estimated attitude using the PDA filter with $P_D = 0.99$ and $\lambda = 10^{-6}m^{-3}$, compared to the AHRS.

Bias

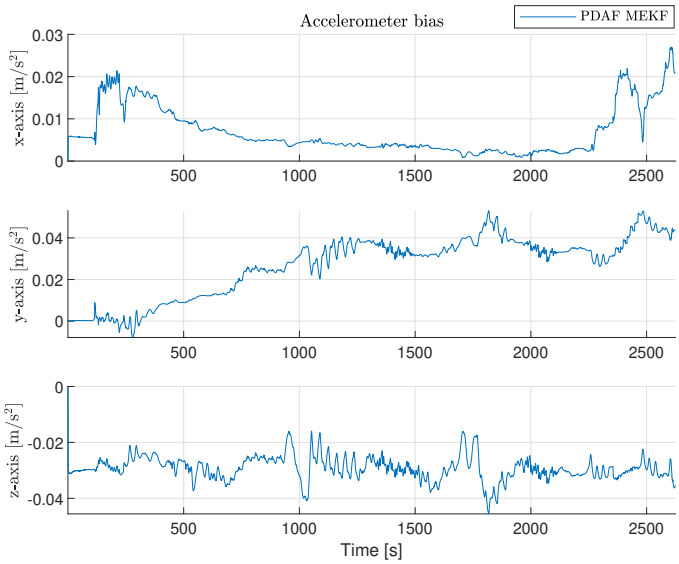

Figure D.11: Estimated accelerometer biases using the PDA filter with $P_D = 0.99$ and $\lambda = 10^{-6}m^{-3}$.

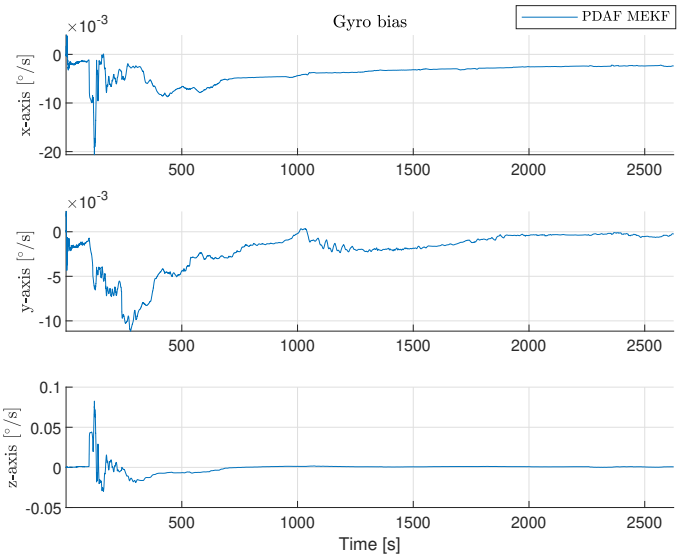

Figure D.12: Estimated gyroscope biases using the PDA filter with $P_D = 0.99$ and $\lambda = 10^{-6}m^{-3}$.

D.4 Synthetic dataset - Nearest Neighbor filter

Velocity

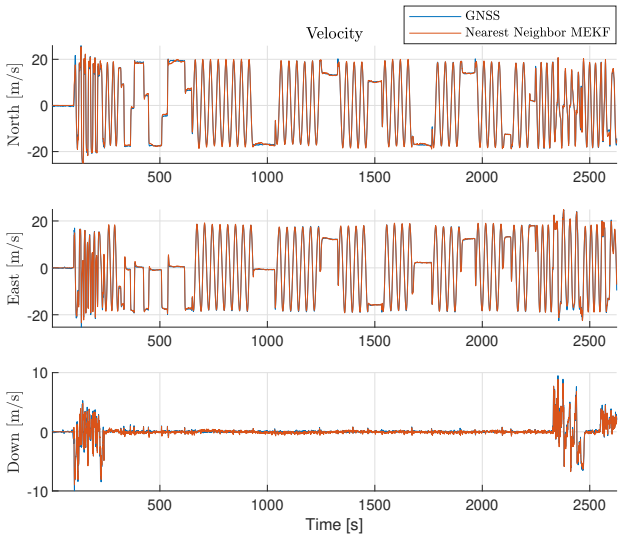

Figure D.13: Estimated velocity using the NN filter on the synthetic dataset, compared to the Pixhawk GNSS calculated velocity.

Attitude

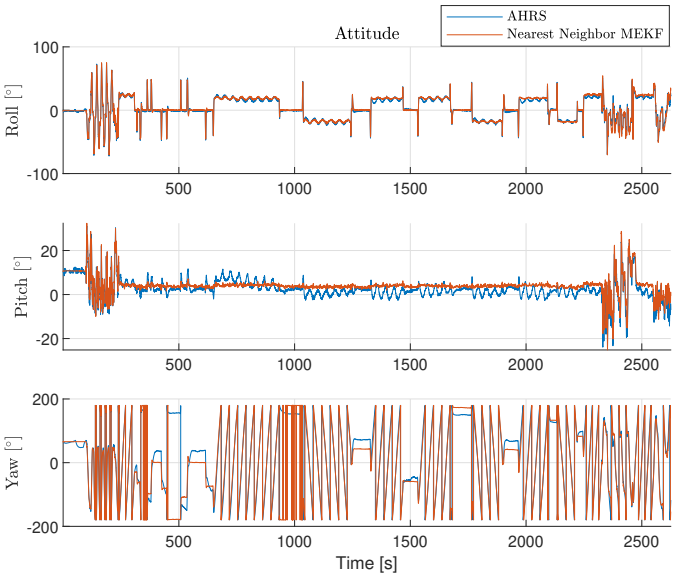

Figure D.14: Estimated attitude using the NN filter on the synthetic dataset, compared to the AHRS.

Bias

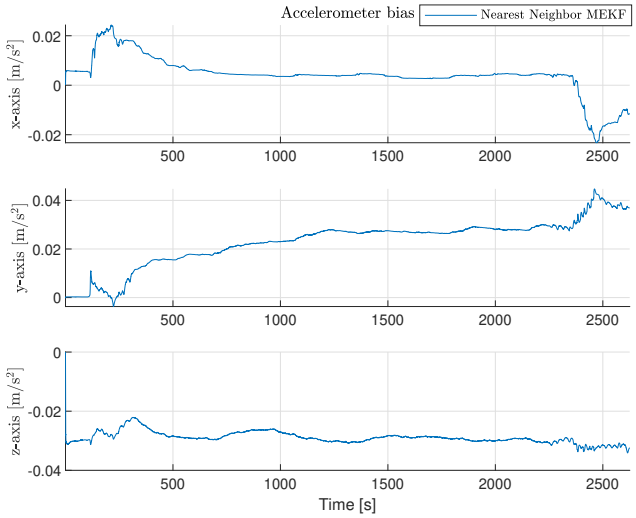

Figure D.15: Estimated accelerometer biases using the NN filter on the synthetic dataset.

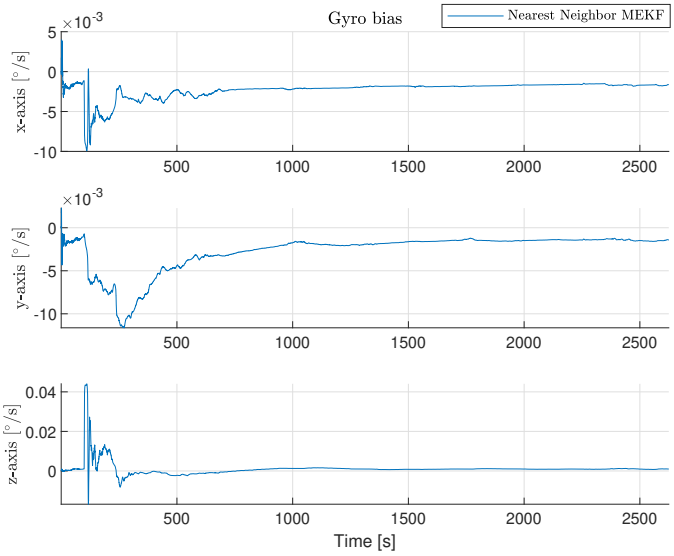

Figure D.16: Estimated gyroscope biases using the NN filter on the synthetic dataset.

D.5 Synthetic dataset - Probabilistic Data Association Filter

Velocity

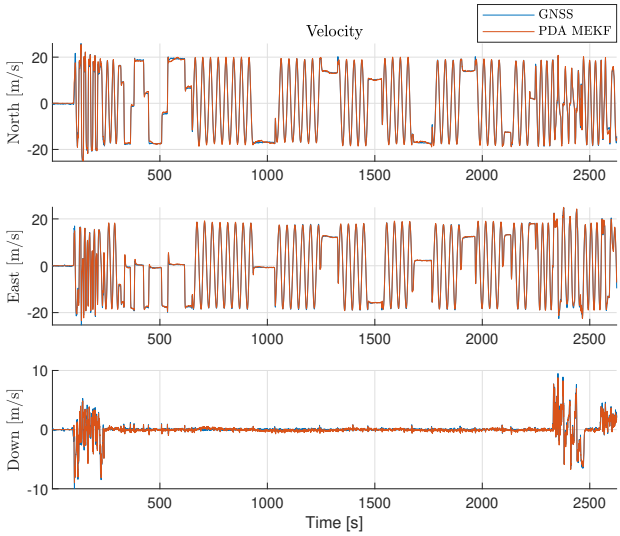

Figure D.17: Estimated velocity using the PDA filter with $P_D = 0.99$, $\lambda = 10^{-9} m^{-3}$ and $\sigma_\alpha = 2°$ on the synthetic dataset, compared to the Pixhawk GNSS calculated velocity.

Attitude

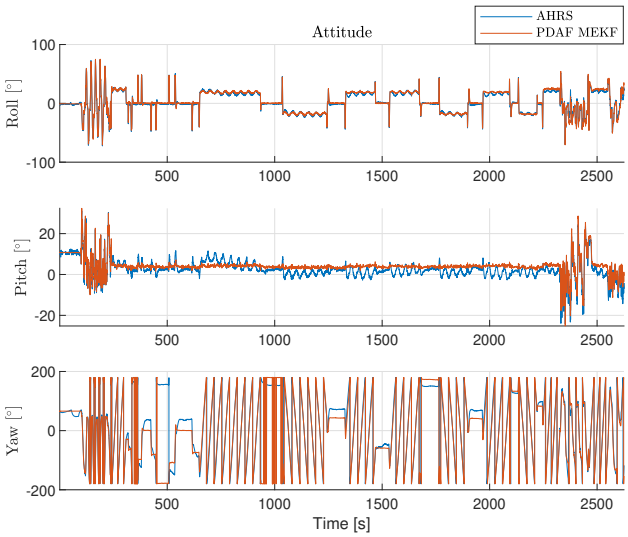

Figure D.18: Estimated attitude using the PDA filter with $P_D = 0.99$, $\lambda = 10^{-9} m^{-3}$ and $\sigma_\alpha = 2°$ on the synthetic dataset, compared to the AHRS.

Bias

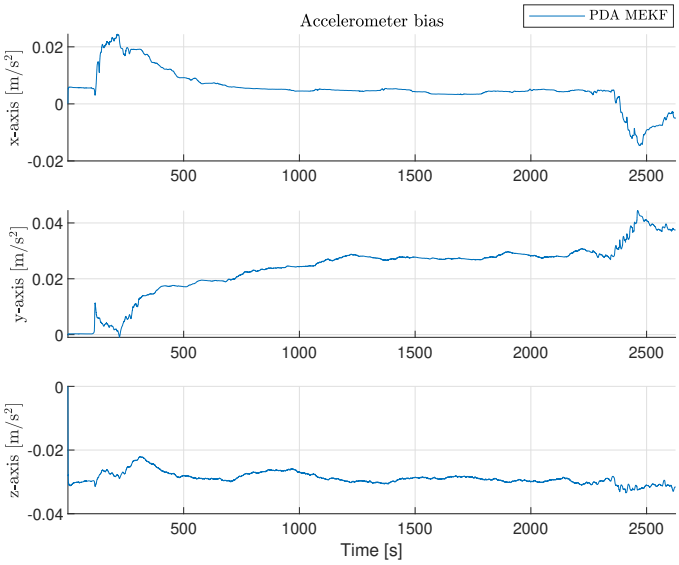

Figure D.19: Estimated accelerometer biases using the PDA filter with $P_D = 0.99$, $\lambda = 10^{-9} m^{-3}$ and $\sigma_\alpha = 2°$ on the synthetic dataset.

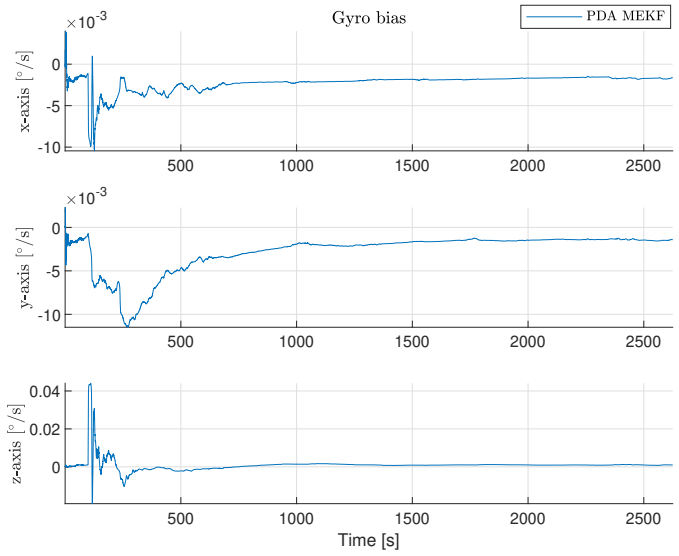

Figure D.20: Estimated gyroscope biases using the PDA filter with $P_D = 0.99$, $\lambda = 10^{-9} m^{-3}$ and $\sigma_\alpha = 2°$ on the synthetic dataset.

Synthetic dataset - Retuned noise covariance matrix

Velocity

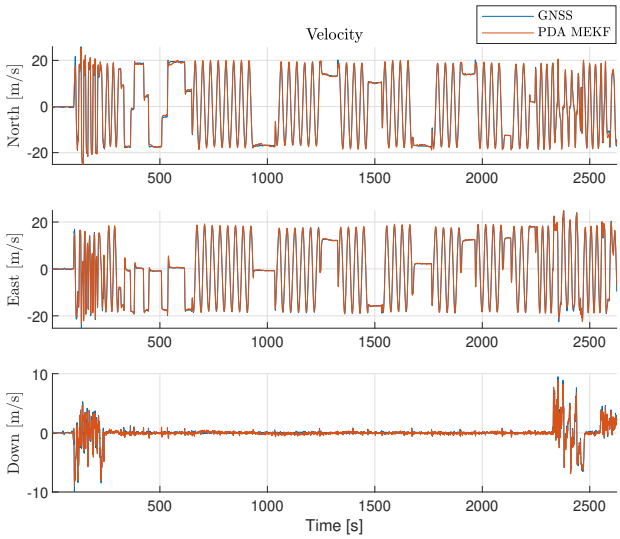

Figure D.21: Estimated velocity using the PDA filter with $P_D = 0.99$, $\lambda = 10^{-9} m^{-3}$ and $\sigma_\alpha = 1.5°$ on the synthetic dataset, compared to the Pixhawk GNSS calculated velocity.

Attitude

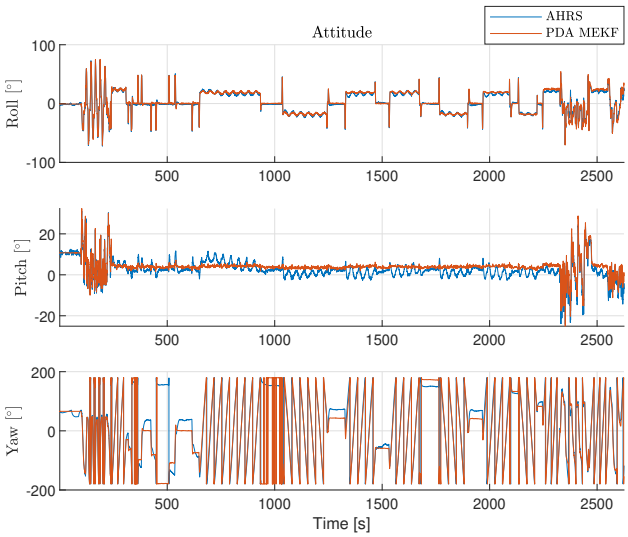

Figure D.22: Estimated attitude using the PDA filter with $P_D = 0.99$, $\lambda = 10^{-9} m^{-3}$ and $\sigma_\alpha = 1.5°$ on the synthetic dataset, compared to the AHRS.

Bias

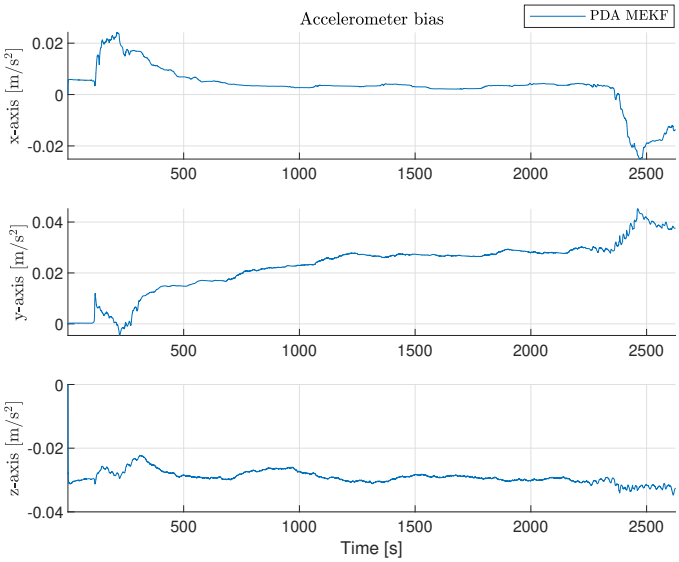

Figure D.23: Estimated accelerometer biases using the PDA filter with $P_D = 0.99$, $\lambda = 10^{-9}m^{-3}$ and $\sigma_\alpha = 1.5°$ on the synthetic dataset.

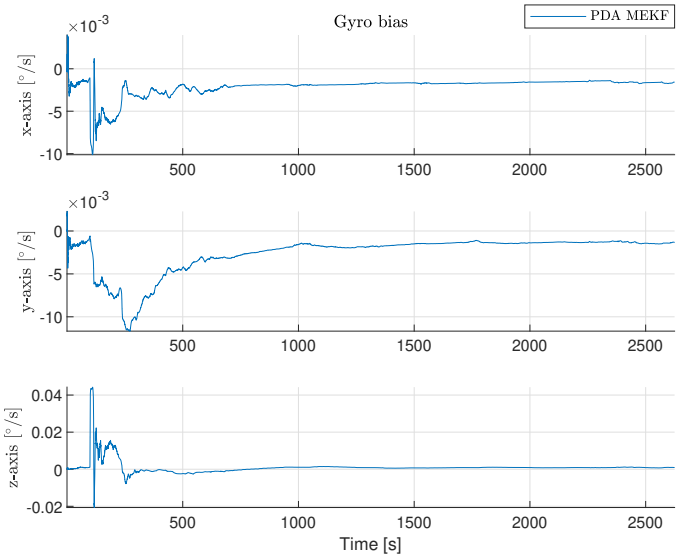

Figure D.24: Estimated gyroscope biases using the PDA filter with $P_D = 0.99$, $\lambda = 10^{-9}m^{-3}$ and $\sigma_\alpha = 1.5°$ on the synthetic dataset.

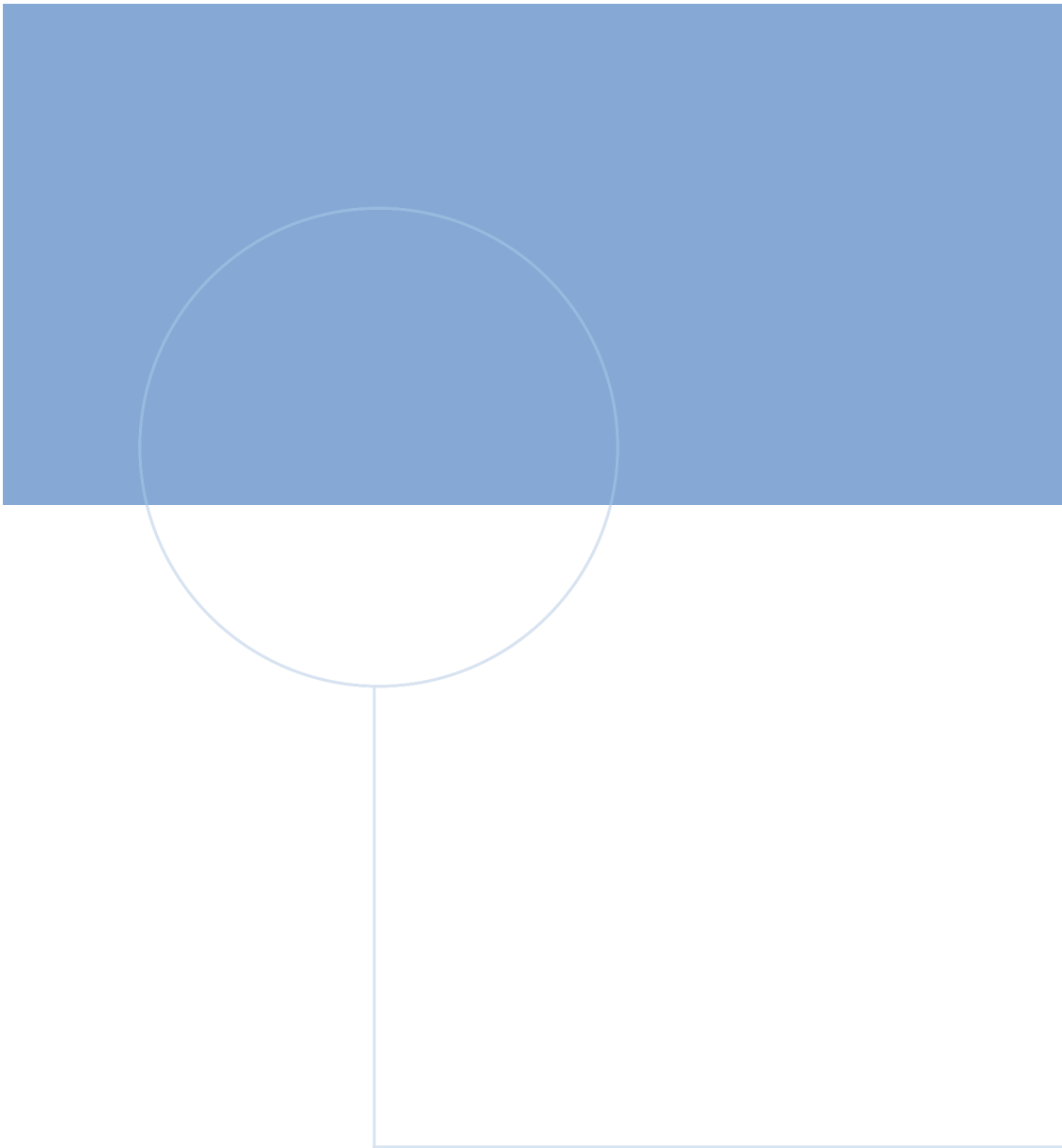

NTNU

Kunnskap for en bedre verden